# Superhydrophobicity of Surfaces Decorated by Electrospun Micro- and Nano-fibers

by

Yi Zhang

A thesis

presented to the University of Waterloo

in fulfillment of the

thesis requirement for the degree of

Doctor of Philosophy

in

Mechanical and Mechatronics Engineering

Waterloo, Ontario, Canada, 2023

# Examining Committee Membership

The following serves on the Examining Committee for this thesis. The decision of the Examining Committee is by majority vote.

| | |
|---|---|
| External Examiner: | Dr. Hongbo Zeng<br>Professor, University of Alberta |
| Supervisor: | Dr. Zhongchao Tan<br>Professor, University of Waterloo |
| Internal Member: | Dr. Kevin Musselman<br>Associate Professor, University of Waterloo |
| Internal Member: | Dr. Xiaoyu Wu<br>Assistant Professor, University of Waterloo |
| Internal-external Member: | Dr. Xianshe Feng<br>Professor, University of Waterloo |

# Author's Declaration

This thesis consists of materials all of which I authored or co-authored: see Statement of Contributions included in the thesis. This is a true copy of the thesis, including any required final revisions, as accepted by my examiners.

I understand that my thesis may be made electronically available to the public.

# Statement of Contributions

Yi Zhang is the sole author for Chapters 1, 2 and 7 which are written under the supervision of Prof. Z. Tan and are not written for publication. This thesis consists of three manuscripts written for publication. Exceptions to sole authorship of material are as follows:

**Research presented in Chapter 3:**

This research is conducted at the University of Waterloo by Yi Zhang under the supervision of Prof. Z. Tan. Yi Zhang designs the study and completes model development and analysis with consultations from Prof. Hesheng Yu, a visiting scholar at the University of Waterloo. Yunqiao Huang and Yifu Li contribute to model verification and draft revision. Yi Zhang drafts the manuscript and each author provides intellectual input on the manuscript.

Y. Zhang, Y. Huang, Y. Li, H. Yu, Z. Tan, Free energy barrier in wetting parallel-structured surfaces, *Colloids and Surfaces A: Physicochemical and Engineering Aspects*, 2022, 655: 130214.

**Research presented in Chapter 4:**

This research is conducted at the University of Waterloo by Yi Zhang under the supervision of Prof. Z. Tan. Yi Zhang designs the study and completes the data collections and analysis with consultations from Yifu Li. Yi Zhang drafts the manuscript and each author provides intellectual input on the manuscript.

Y. Zhang, Y. Li, Z. Tan, Development of Adjustable High- to Low-Adhesive Superhydrophobicity Using Aligned Electrospun Fibers, *Langmuir* (Under review)

**Research presented in Chapter 5 and Chapter 6:**

This research is conducted at the University of Waterloo by Yi Zhang under the supervision of Prof. Z. Tan. Yi Zhang designs the study and completes the data collections and analysis with consultations from Yifu Li, Prof. Hesheng Yu, and Yunqiao Huang. Yifu Li and Prof. Zhigang Zuo contribute to draft revision. Prof. Kevin Musselman assists characterization of sample. Xiaoming Duan and Prof. Zhenghe Xu provide resources for writing. Yi Zhang drafts the manuscript and each author provides intellectual input on the manuscript.

Y. Zhang, Y. Li, Y. Huang, Z. Zuo, K. Musselman, X. Duan, H. Yu, Z. Xu, Z. Tan, A Facile and Strategic Approach to Superhydrophobic Fibrous Structure with Biaxially Aligned Electrospun Porous Fibers, *Advanced Materials Interfaces*. doi.org/10.1002/admi.202300507

As the first author of these three publications, I am responsible for model development, experimental design, data collection and preliminary analysis, and drafting manuscript. My coauthors provide guidance during each step of the research and offer feedback on draft the manuscripts.

# Abstract

A superhydrophobic surface, characterized with a water contact angle more than 150˚, can show lotus or rose-petal effect depending on the adhesion strength to droplets. For the lotus effect, droplets can roll off the surface at a small tilting angle, usually less than 10˚. For the rose-petal effect, droplets can adhere to the surface even by turning the surface upside down. Both effects have gained much attention for their wide applications.

Electrospinning is proven to be an efficient and versatile technique for developing superhydrophobicity based on the surface roughness provided by the generated micro- and nanofibers. However, current electrospinning methods suffer from a lack of strategic approach to superhydrophobicity and complex fabrication. Based on the influence of fiber morphology parameters on surface wettability, this thesis research aims to develop rose-petal and lotus superhydrophobic surfaces using uniaxially aligned fibers and biaxially aligned porous fibers, respectively. Both fibers are fabricated by simple one-step electrospinning.

This thesis starts with building an integrated thermodynamic model for droplet wetting on various parallel-structured surfaces to understand the wetting behavior. The model relates free energy to the continuous movement of three-phase contact lines (TPCLs) in different wetting states, and the forming conditions of free energy barrier are derived from the model. Then the model and the forming conditions of energy barrier are validated using data in the literature and experimental data using aligned fibers. The model indicates that compared to structures with sharp edge, round structures can broaden the range of apparent contact angle (APCA) for energy barriers. Thus, surfaces patterned by round structures can achieve large APCAs with high contact angle hysteresis, which are needed for rose-petal effect.

Then this thesis specifies the wetting model for surfaces patterned by uniaxially aligned fibers based on the preceding integrated model. The model indicates that the energy barrier increases with fiber diameter and the basal width of droplet. Uniaxially aligned polystyrene fibers with average diameters of 0.9 and 1.8 μm and inter-fiber distance ($l$) from 70 to 1450

μm are fabricated to study the wetting behavior on surfaces dressed by aligned fibers. Based on the wetting behavior, petal-effect surfaces are fabricated using uniaxially aligned fibers with an average diameter of 1.8 μm and *l* between 70 and 130 μm. The APCAs of the petal-effect surfaces are in a range of 150˚-156˚, and droplets can adhere to the surfaces even by turning the surfaces upside down.

After that, this thesis studies the wetting behavior on surfaces dressed by aligned porous fibers. Uniaxially and biaxially aligned porous fibers are fabricated onto substrate surfaces through one-step electrospinning with controlled relative humidity. On the uniaxially aligned fibers, droplets are in the Cassie-Baxter (CB) state when *l* is less than 18.2 μm. For *l* greater than 18.2 μm, wetting transition to the Wenzel state occurs. On the biaxially aligned porous fibers, droplets stay in CB state even when *l* reaches 34 μm. More importantly, there is no change in the variation trend of hydrophobicity for *l* between 18.2 and 34 μm compared to that for *l* below 18.2 μm, indicating that the droplets stay on the upper-layer fibers without contacting the lower-layer fibers or substrate. Numerical simulation using Surface Evolver shows that a Cassie-Baxter-"restoring" (CaRe) wetting contributes to a more stable CB state in the biaxial structure. Lotus-effect surfaces are thus developed based on the CaRe wetting using the biaxial structure. As a result, the developed structure has contact angles between 159˚ and 162˚ and roll-off angles from 10˚ to 3˚ for water droplets from 3 to 10 μL in volume.

Finally, two potential applications of the developed biaxial structure are demonstrated. First, the biaxial structure is used to develop a waterproof, breathable, and superhydrophobic membrane by depositing fibers on a supporting commercial nylon mesh. The breathability of the membrane is quantified by water vapor transmission rate, which is $20.8 \pm 0.1\ kg \cdot m^{-2} \cdot d^{-1}$. The second application is a surface layer for wearable electronics. After being patched with the biaxial structure for 60 minutes, the human forearm skin shows unnoticeable change in temperature. In addition, the average transmittance in the visible region (380-760 nm) of the biaxial structure is 83.6 ± 3.1% using a UV-Vis spectrophotometer.

# Acknowledgements

For this PhD degree, I have traveled a long road. But when I graduate, everything along the way will become scenery.

First, I would like to express my deep gratitude to my supervisor, Prof. Zhongchao Tan, without whom I could not have undertaken this journey. His invaluable criticism, generous support, and endless patience steered me through this research. I am so fortunate to grow up as a researcher under his supervision.

I am also truly grateful to all my committee members, Prof. Hongbo Zeng, Prof. Xianshe Feng, Prof. Kevin Mussulman, Prof. Xiaoyu Wu for providing professional evaluations and constructive comments on this thesis.

I would like to extend my sincere thanks to the previous and current members of Green Energy & Pollution Control Research Lab. I want to thank Dr Yifu Li and Yunqiao Huang for their innumerable help in both research and life, and also all the wine we drunk for our friendships; Dr. Hesheng Yu for being always available when I need guidance and support in research; Lei Wang, Jiawen Zheng, Lizhen Hu, Erqian Gao, Scott Smith, Stephen Banjo, Dr Fangyan Sun for offering valuable assistance in the lab.

Special thanks also go to my girlfriend, Anna Zhang, for all her love and support. She has pulled me back from depression countless times with her innocence and loveliness.

Last, I would be remiss in not mentioning my parents, who have always stood by me and provided endless support to me in pursuing a PhD degree. I hope to have more time to spend with them in the future.

# Table of Contents

# List of Figures

# List of Tables

# List of Abbreviations

| Notation | Term |
|---|---|
| **Abbreviations** | |
| CNT | Carbon nanotube |
| DCM | Dichloromethane |
| DMAc | *N*, *N*-dimethylacetamide |
| DMF | N,N-dimethylformamide |
| DMDCS | Dichlorodimethyl silane |
| DTMS | *n*-dodecyltrimethoxysilane |
| FAS | Fluoroalkylsilane |
| FDTS | (heptadecafluoro-1, 1, 2, 2-tetrahydrodecyl)trichlorosilane |
| FPI | Fluorinated polyimide |
| FPU | Fluorinated polyurethane |
| Hap | Hydroxyapatite |
| HFIP | Hexafluoro isopropanol |
| NF | Nanoflake |
| NP | Nanoparticle |
| NFES | Near-field electrospinning |
| PA6 | Polyamide 6 |
| PAA | Poly(acrylic acid) |
| PAH | Poly(allylamine hydrochloride) |
| PAM | Poly(acryl amide) |
| PAN | Polyacrylonitrile |
| PANI | Polyaniline |
| PCC | n-octadecane phase change capsules |

| | |
|---|---|
| PCL | Poly(caprolactone) |
| PDMS | Poly(methylhydrosiloxane) |
| PEO | Poly(ethylene oxide) |
| PES | polyethersulfone |
| PET | Poly(ethylene terephthalate) |
| PFDT | 1H,1H,2H,2H-perfluorodecanethiol |
| PFDTES | Perfluorodecyltrietho-xysilane |
| PI | Polyimide |
| PLLA | Poly(L-lactic acid) |
| PMMA | Poly(methyl methacrylate) |
| PnPrOx | Poly(2-n-propyl-2-oxazoline) |
| PolyPhe | Poly(L-phenylalanine) |
| PPFEMA | Poly(perfluoroalkyl ethyl methacrylate) |
| PS | Polystyrene |
| PS-PDMS | Poly(styrene-*b*-dimethylsiloxane) |
| PTFE | Poly(tetrafluoroethylene) |
| PU | Polyurethane |
| PVA | Poly(vinyl alcohol) |
| PVB | polyvinyl butyral |
| PVC | Polyvinyl chloride |
| PVDF | Poly(vinylidene fluoride) |
| PVDF-HFP | Poly(vinylidene fluoride-co-hexafluoropropylene) |
| PVP | Poly(vinyl pyrrolidone) |
| SEBS | Poly(styrene-*b*-(ethylene-*co*-butylene)-*b*-styrene) |
| THF | Tetrahydrofuran |
| TM | Tourmaline |

| | |
|---|---|
| γ-PGA-Phe | γ-PGA modified with *L*-phenylalanine ethylester |

**Acronyms**

| | |
|---|---|
| ACA | Advancing contact angle |
| BN | Boron nitride |
| CA | Cellulose acetate |
| CAH | Contact angle hysteresis |
| CB | Cassie-Baxter |
| CVD | Chemical vapor deposition |
| ECA | Equilibrium contact angle |
| iCVD | Initiated chemical vapor deposition |
| ICA | Intrinsic contact angle |
| LBL | Layer-by-layer |
| LBM | Lattice Boltzmann Method |
| MCA | Metastable contact angle |
| RCA | Receding contact angle |
| RH | Relative humidity |
| SEM | Scanning electron microscope |
| WBS | Waterproof, breathable, superhydrophobic |
| WVTR | Water vapor transmission rate |

# List of Symbols

| Notation | Term | Unit |
|---|---|---|
| $A$ | Surface area | $m^2$ |
| $A_1$ | Surface area of the outer surface of droplet | $m^2$ |
| $A_2$ | Apparent contact area between droplet and solid surface | $m^2$ |
| $A_c$ | Cup opening area for water vapor transmission rate test | $m^2$ |
| $d$ | Fiber diameter | m |
| $d_c$ | Characteristic diameter of the produced porous fibers | m |
| $E$ | Free energy per unit depth | J/m |
| $f_1$ | Ratio of solid-liquid interface area to droplet basal area | |
| $f_2$ | Ratio of bottom liquid-vapor interface area to droplet basal area | |
| $f$ | Ratio of solid-liquid interface area to droplet basal area when $f_1 + f_2 = 1$ | |
| $f_p$ | Fraction of fiber surface occupied by pores | |
| $G$ | Free energy | J |
| $g$ | Gravity acceleration | $m/s^2$ |
| $h$ | Height of surface structure | m |
| $l$ | Inter-fiber distance | m |
| $l_1$ | Total width of one surface structure and groove | m |
| $l_2$ | Width of one surface structure | m |
| $l_w$ | Normalized wetting length | |
| $L$ | Length of interface | m |
| $L_t$ | Total width from the first to the $N^{th}$ measured fiber | m |

| | | |
|---|---|---|
| $m$ | Weight | kg |
| $N$ | Number of fibers across the measured area | |
| $n$ | Half number of covered structure unit | |
| $r$ | Radius of surface structure | m |
| $r_w$ | Ratio of actual and projected solid-liquid interface area | |
| $R_0$ | Radius of droplet before contact | m |
| $R_1$ | Radius of droplet after contact | m |
| $R_2$ | Half-length of contact interface | m |
| $s$ | Wetted length on horizontal surfaces by exterior TPCL in one structure unit | m |
| $s'$ | Wetted length on each horizontal surface by exterior TPCL | m |
| $S$ | Cross-section area of droplets | $m^2$ |
| $S_{structure}$ | Cross-section area of one surface structure | $m^2$ |
| $S_{groove}$ | Cross-section area of one groove | $m^2$ |
| $S_2$ | Cross-section area difference between the liquid below external TPCL and the structure above external TPCL | $m^2$ |
| $t$ | Time | s |
| $V$ | Droplet volume | $m^3$ |

**Greek letters**

| | | |
|---|---|---|
| $\alpha_r$ | Roll-off angle | |
| $\gamma$ | Surface tension | N/m |
| $\delta_i$ | Wetted length by interior TPCL | m |
| $\delta_e$ | Wetted length on each inclined surface by exterior TPCL | m |
| $\delta_o$ | Wetted length on inclined surfaces by exterior TPCL in one structure unit | m |

| | | |
|---|---|---|
| $\delta_o'$ | Wetted length on each inclined surface by exterior TPCL | m |
| $\theta_A$ | Apparent contact angle | |
| $\theta_Y$ | Intrinsic contact angle | |
| $\theta_{Y,F}$ | Intrinsic contact angle of fiber | |
| $\theta_{Y,S}$ | Intrinsic contact angle of substrate | |
| $\theta_i$ | Wetted angle by interior TPCL | |
| $\theta_o$ | Angular position of exterior TPCL | |
| $\theta_{s1}$ | Structure parameter as defined in Figure 3.5 | |
| $\theta_{s2}$ | $2\varphi - \theta_{s1}$ for $\theta_o < 180^\circ$; $-\theta_{s1}$ for $\theta_o > 180^\circ$ | |
| $\theta_{s3}$ | 0 for $\theta_o < 180^\circ$; $\varphi - \theta_{s1}$ for $\theta_o > 180^\circ$ | |
| $\rho$ | Droplet density | $kg/m^3$ |
| $\varphi$ | Internal angle of surface structure | |

**Subscripts**

| | |
|---|---|
| C1, C2 | Position of exterior TPCL in composite state |
| CB | Cassie-Baxter state |
| i, ii′, ii″ | State (i, ii′, ii″) of droplets on biaxial structure |
| LV1 | Liquid-vapor interface 1 |
| LV2 | Liquid-vapor interface 2 |
| SL | Solid-liquid interface |
| SV | Solid-vapor interface |
| T1-3 | Position of interior TPCL in wetting transition |
| W | Wenzel state |
| W1-4 | Position of exterior TPCL in noncomposite state |

# Chapter 1 Introduction

## 1.1 Background

Liquid wetting of solid surfaces is an ubiquitous phenomenon in nature [1]. The wettability of solid surfaces, which is often assessed by sessile droplet contact angles [2], is an important property to various applications related to energy [3], environment [4], health [5], etc.

Figure 1.1 shows the classification of surface wettability based on the contact angle: (A) superhydrophilicity, (B) hydrophilicity, (C) hydrophobicity, and (D) superhydrophobicity. Specifically, a hydrophilic surface has a strong affinity to liquid, thereby showing a contact angle less than 90˚. The surface is superhydrophilic if its contact angle is lower than 5˚-10˚ [6]. Conversely, a hydrophobic surface repels liquid and shows a contact angle greater than 90˚. When the contact angle is greater than 150˚, the surface can be defined as a "lotus" or "rose-petal" superhydrophobic surface depending on its adhesion strength to droplets. For the lotus superhydrophobicity, as shown in Figure 1.1 (D-1), the sliding angle, which is the threshold tilting angle of the surface when droplets start to slide, is usually less than 10˚ [7]. In contrast, the rose-petal superhydrophobicity has strong droplet adhesion, so droplets stay pinned on the surface even by turning upside down [8], as shown in Figure 1.1 (D-2).

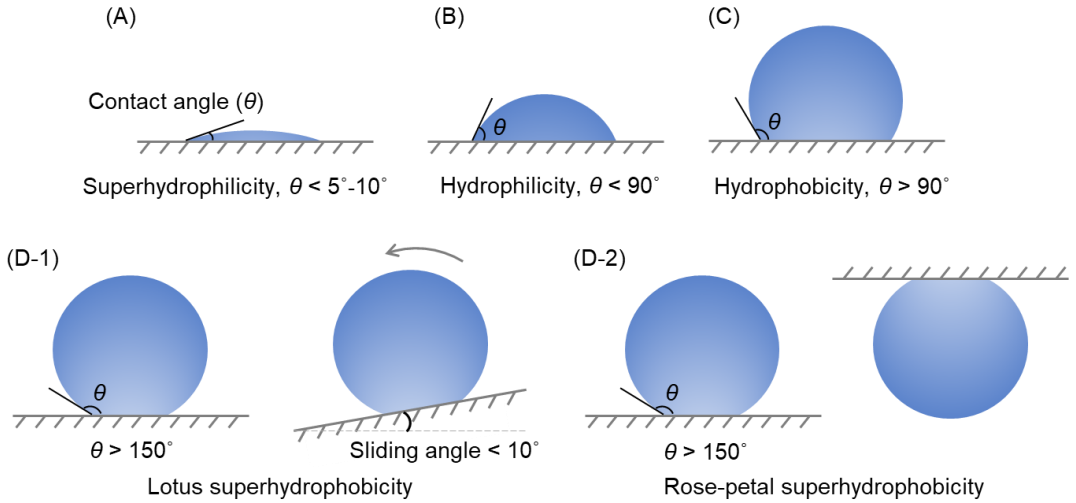


**Figure 1.1.** Classification of solid surface wettability based on contact angle: (A) super-hydrophilicity, (B) hydrophilicity, (C) hydrophobicity, and (D) superhydrophobicity.

Figure 1.2 demonstrates that water droplets roll off (A) lotus leaf while rain droplets are retained on (B) rose petals. The lotus superhydrophobicity, also known as “lotus effect”, originates from the extreme water repellency and the self-cleaning property of lotus leaf (*Nelumbo nucifera*) [9, 10]. Similarly, the rose-petal superhydrophobicity, or “petal effect”, is defined based on the phenomenon that water droplets remain spherical on rose petals but cannot roll off even by turning the petals upside down [11].

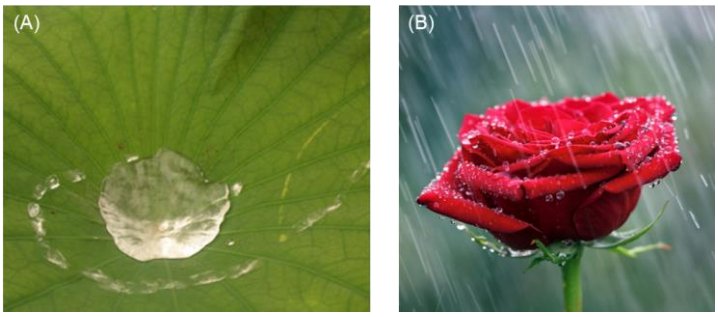


**Figure 1.2.** Droplets on (A) lotus leaf [12] and (B) rose petals [13].

Both lotus effect and petal effect have received much attention for their wide applications. For the lotus effect, the ability to remove surface contaminants such as dust particles using droplets allows for developing self-cleaning surfaces; its applications can be found in any field where clean surfaces are necessary, such as sensors, solar cells, textiles [14]. Moreover, the surfaces with lotus-effect also exhibit properties of anti-corrosion [15], anti-icing [16], anti-fogging [17], etc. For the petal effect, retaining spherical droplets with strong adhesion are promising for microdroplet transportation [18], lap-on-chip devices [19], single molecule spectroscopy [20], etc.

## 1.2 Motivations and challenges

The wettability of a solid surface is controlled by surface roughness and surface energy. For a flat surface, its apparent contact angle, which equals the intrinsic contact angle of surface material, cannot exceed 120˚ because a material with an intrinsic contact angle greater than 120˚ is rarely found [6]. Therefore, proper surface roughness is needed to develop lotus or rose-petal superhydrophobicity, which requires an apparent contact angle greater than 150˚.

Various fabrication technologies such as lithography [21], chemical [22] or plasma [23] etching, laser micromachining [24], and electrospinning [25] have been used for developing superhydrophobic surfaces. Among them, electrospinning is a facile and versatile technology to produce fibers in micro- and nanoscale by applying a high voltage on a viscous polymer solution. The produced fibers, which may also have a secondary fiber morphology, increase surface roughness, enabling superhydrophobicity. Moreover, electrospinning is considered an additive manufacturing technology, and the introduced fibrous structure is featured with a high air permeability due to the interconnectivity between inter-fiber pores [26], which is needed for many applications. Thus, using electrospinning to develop superhydrophobicity receives growing attention in recent years as evidenced by the rising numbers of the annual publications, as shown in Figure 1.3.

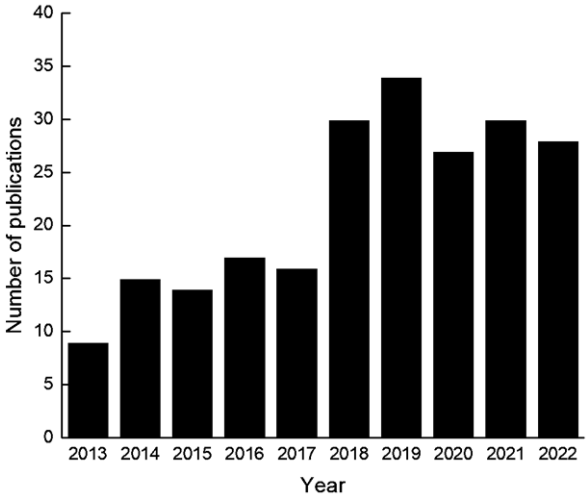


**Figure 1.3.** Number of publications in creating superhydrophobicity by electrospinning (data obtained by searching keywords “electrospinning” and “superhydrophobicity” from Web of Science database on April 28, 2023)

The electrospinning-based methods for developing superhydrophobicity can be classified into one-step electrospinning and electrospinning followed by post treatments. For the one-step electrospinning methods, superhydrophobicity is directly realized on the as-spun fibrous structures. For those with post treatments, superhydrophobicity is achieved by modifications of fiber surfaces after electrospinning.

At present, most electrospinning methods realize superhydrophobicity by increasing fiber surface roughness and/or reducing fiber surface energy. To increase fiber surface roughness, a secondary fiber morphology including beads [27] and nanoparticles [28] is often created on the fiber surfaces in electrospinning [29] or after electrospinning by post treatments [30]. Moreover, methods such as copolymer [31] and coaxial [32] electrospinning of a low surface energy polymer with an electrospinnable polymer, and coating the as-spun fibers with a thin layer of a low surface energy material such as poly(perfluoroalkyl ethyl methacrylate) [33] after electrospinning have been reported to reduce the fiber surface energy.

However, a strategic approach to superhydrophobicity in electrospun fibers is still lacking. Current theoretical works have limited abilities in guiding the development of fiber-based superhydrophobicity because either the works are limited to only investigating the stability of wetting state or the theoretical structures are difficult to replicate. The control of fiber morphology parameters, including fiber diameter, inter-fiber distance, and fiber orientation, in previous works has often relied on trial-and-error approaches. As a result, thick fibrous mats are usually made to reduce the heterogeneity of fiber morphology, reducing the air permeability and transparency. In addition, the fibers may show different wettability despite similar intrinsic contact angles and secondary fiber morphologies [27, 34, 35].

Moreover, existing electrospinning-based methods usually involve complex fabrication processes for achieving superhydrophobicity. To induce secondary fiber morphologies, for example, nanoparticles are blended with polymer solutions for electrospinning or coated on the fibers after electrospinning. Homogeneous mixing of nanoparticles with a polymer solution takes extra efforts to disperse the nanoparticles [36], and post treatments are needed to coat fibers with nanoparticles. Alternatively, copolymer and coaxial electrospinning, and coating fiber surface after electrospinning are often adopted to reduce fiber surface energy. All these can complicate the fabrication and limit their applications. Therefore, a simple one-step electrospinning method without additive is needed to develop superhydrophobicity.

## 1.3 Research objectives

This thesis aims to develop simple electrospinning-based methods for the fabrication of petal and lotus superhydrophobic surfaces with strategic approach. The objective is achieved by the following steps. First, understanding the droplet wetting behavior on parallel-structured surfaces helps to develop superhydrophobicity. The influence of fiber morphology on the wettability is modeled and experimentally validated. Then, superhydrophobic surfaces with petal effect are developed using aligned fibers fabricated by one-step electrospinning. After that, the wetting behavior of droplets on uniaxially (mono layer) and biaxially (dual layers) aligned porous fibers is studied. Later, lotus surfaces are fabricated using biaxially aligned porous fibers made by one-step electrospinning. Finally, the developed lotus surface is used to develop a waterproof, breathable, and superhydrophobic membrane, and a surface layer for wearable electronics.

The following specific tasks are completed in this thesis work:

1) Develop an integrated thermodynamic model for wetting various parallel-structured surfaces.
2) Quantify the influence of fiber morphology parameters on the wettability of surfaces structured by aligned electrospun fibers.
3) Develop petal superhydrophobic surfaces using aligned electrospun fibers.
4) Compare the wetting behavior on uniaxially and biaxially aligned porous fibers.
5) Develop lotus superhydrophobic surfaces using biaxially aligned porous fibers.
6) Demonstrate the potential applications of the developed lotus surfaces.

## 1.4 Thesis structure

The thesis is organized as follows. Chapter 1 presents the background of superhydrophobic surfaces with lotus and rose-petal effects, followed by introducing current electrospinning-based methods for developing superhydrophobic surfaces. Despite the substantial progress

in research, these electrospinning-based methods still involve complexity in fabrication and lack strategic approach to superhydrophobicity. Therefore, this thesis is motivated to develop simple on-step electrospinning methods for fabrication of lotus and petal superhydrophobic surfaces based on a strategic approach.

Chapter 2 starts with the wetting theory and the methods to modify surface wettability by electrospinning. The surface wettability can be modified by controlling fiber morphology, fiber surface chemistry, or both. Based on the fundamentals and the methods, a detailed literature review about developing superhydrophobicity based on electrospinning is provided. For both lotus and rose-petal superhydrophobicity, the electrospinning-based methods can be classified into one-step electrospinning and electrospinning followed by post treatments based on the fabrication steps.

Chapter 3 details an integrated thermodynamic model for droplets wetting on parallel-structured surfaces with various cross-sections, including circle, elongated circle, trapezoid, rectangle, and inverted trapezoid. The model relates free energy to the continuous movement of three-phase contact lines in different wetting states, and the forming conditions for free energy barrier are specified. Then, the model and the forming conditions of energy barrier are validated experimentally by electrospun fibers and existing experimental and theoretical works. Based on the validated model, the wetting behaviors on various parallel-structured surfaces are studied and compared.

Chapter 4 introduces the development of petal-effect surfaces based on uniaxially aligned electrospun fibers. First, aligned polystyrene fibers with various fiber diameters and inter-fiber distances are produced onto substrates by simple one-step electrospinning, followed by characterization of fiber morphology and wettability. The influence of fiber morphology parameters on the wettability of surfaces dressed by aligned fibers is experimentally studied with explanation of mechanism based on a wetting model for aligned fibers. The model is specified from the integrated model introduced in Chapter 3. Then petal-effect surfaces are constructed using aligned fibers based on the influence of fiber parameters.

Chapter 5 adopts aligned porous fibers to develop lotus effect because the porous fiber surface reduces the contact area between fibers and droplets and the alignment serves as a track to facilitate droplets rolling off. First, uniaxially and biaxially aligned porous fibers are deposited onto substrate surfaces by one-step electrospinning with controlled relative humidity. Then the measured hydrophobicity of surfaces dressed by uniaxially and biaxially aligned porous fibers is compared and explained by numerical modeling. A numerical model is developed in Surface Evolver to determine the wetting state of droplets on fiber-dressed surfaces. Finally, based on the biaxially aligned porous fibers, lotus surfaces are constructed following a strategic approach considering the influence of porous fiber parameters.

Chapter 6 demonstrates the potential engineering applications of the biaxial structure in Chapter 5 based on the lotus effect and the expected high breathability, only consisting of two layers of aligned fibers. Two engineering applications are demonstrated, including 1) development of waterproof, breathable, and superhydrophobic membrane, and 2) a surface layer for protecting wearable electronics.

Chapter 7 summarizes the conclusions of this thesis research and then recommends the research directions for the future.

# Chapter 2 Literature Review

## 2.1 Basics of surface wetting

This section introduces the wetting theories for flat and rough surfaces that are needed to understand various wetting phenomena.

### 2.1.1 Wetting on ideal flat surface

Figure 2.1 presents the schematic of a droplet wetting on an ideal flat surface. The apparent contact angle (APCA, $\theta_A$), which is the macroscopically observed contact angle [37], can be expressed by the well-known Young's equation [38, 39]:

$$\cos\theta_A = \frac{\gamma_{SV} - \gamma_{SL}}{\gamma_{LV}} \tag{2.1}$$

where $\gamma$ is surface tension; the subscripts S, L, and V represent solid, liquid, and vapor, respectively. The APCA for a flat surface is also known as the intrinsic contact angle (ICA, $\theta_Y$) [40] of the surface material, which is determined by the chemical composition of the surface. Note that surface tension varies among different liquids, so the contact angle for a certain solid surface varies with different probing liquids. In this thesis, the contact angle refers to water contact angle unless specified otherwise.

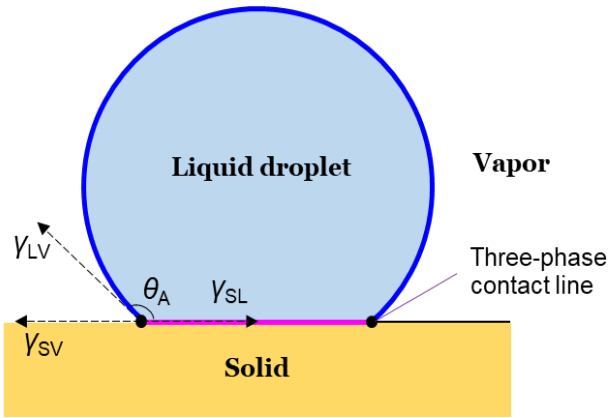


**Figure 2.1.** Schematic of droplet wetting on an ideal flat surface

Figure 2.2 shows the schematic of the change of Gibbs free energy with APCA on a flat surface. From a thermodynamic perspective, the spreading of a droplet on a solid surface can be regarded as a Gibbs free energy minimization process with the movement of three-phase contact line (TPCL, Figure 2.1). The movement of TPCL along the solid surface changes APCA. The three-phase system is at the global minimum of free energy when $\theta_Y$ is reached. Therefore, $\theta_Y$ is the equilibrium contact angle (ECA) for flat surfaces.

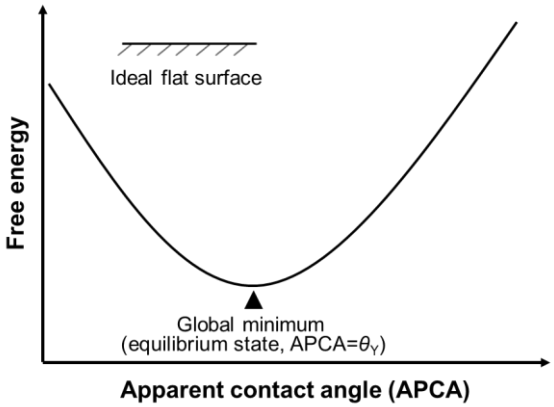


**Figure 2.2.** Schematic of the change of free energy with APCA on flat surfaces.

### 2.1.2 Wetting on rough surface

In reality, most surfaces exhibit a certain degree of roughness. Figure 2.3 shows two potential wetting states on rough surfaces: (A) composite state and (B) noncomposite state.

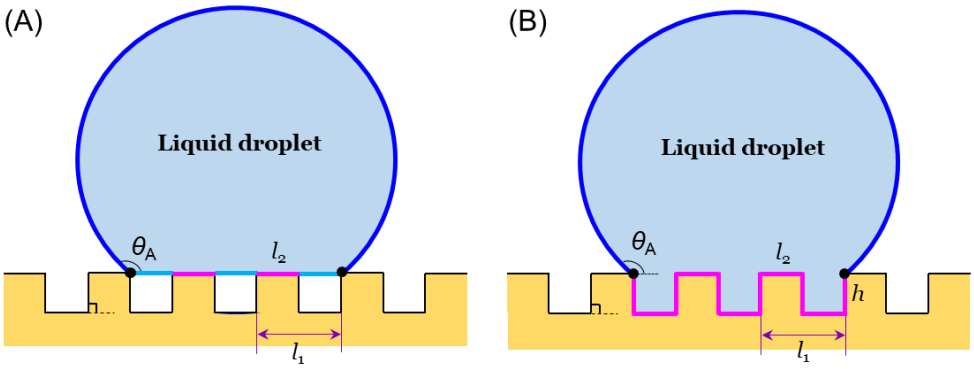


**Figure 2.3.** Schematics of (A) composite wetting and (B) noncomposite wetting on rough surfaces.

In composite state, also known as Cassie-Baxter state [41], air is trapped under the droplet, and the contact angle $\theta_A$ can be modeled using Cassie-Baxter equation [41]:

$$\cos\theta_A = f_1 \cos\theta_Y - f_2 \tag{2.2}$$

where $f_1$ and $f_2$ are the ratios of solid-liquid and liquid-vapor interface areas, respectively, under the droplet to the droplet basal area. In Figure 2.3(A), $f_1 = l_2/l_1$, $f_2 = 1 - l_2/l_1$ given that the structure surface has negligible roughness.

In noncomposite state, or Wenzel [42] state, the solid surface under the droplet is fully wetted by liquid, and the contact angle $\theta_A$ can be analyzed using Wenzel equation [42]:

$$\cos\theta_A = r_w \cos\theta_Y \tag{2.3}$$

where $r_w$ is the ratio of the actual to the projected solid-liquid interface area, which is $r_w = (l_1+2h)/l_1$ as shown in Figure 2.3(B) given that the structure surface has negligible roughness. For an intrinsically hydrophobic or hydrophilic surface, the noncomposite state enhances its hydrophobicity or hydrophilicity since $r_w$ is always greater than 1.

Figure 2.4 shows a schematic of the change of Gibbs free energy with APCA on a rough surface. The Cassie-Baxter equation and Wenzel equation give the ECA for composite and noncomposite state, respectively [43]. Different from Figure 2.2, local minima of free energy exist in Figure 2.4, so a droplet may be pinned at a metastable state and exhibit a metastable contact angle (MCA), because of free energy barrier [37, 44]. The largest and the smallest MCAs are advancing contact angle (ACA) and receding contact angle (RCA), respectively [2]. The difference between ACA and RCA is known as contact angle hysteresis (CAH).

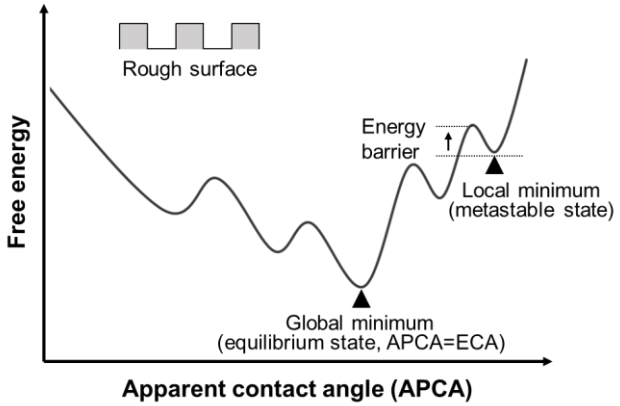


**Figure 2.4.** Schematic of the change of free energy with APCA on rough surfaces.

### 2.1.3 Wetting transition

Even if on the same rough surface, the wetting state of a liquid droplet may transit from the composite to noncomposite state upon receiving external perturbations, resulting in different ECAs and CAHs [9]. This transition process is termed wetting transition: liquid penetrates into the surface grooves, and finally the liquid-vapor interface under the droplet disappears. Wetting transition can be attributed to the lower system energy of the noncomposite state compared to the composite state. The two wetting states are separated by asymmetric free energy barriers, so wetting transition is generally considered to be irreversible [45]. When the composite state is energetically favorable, transition from noncomposite to composite state can be achieved [46, 47].

Figure 2.5 presents two possible mechanisms of wetting transition: (A) sagging and (B) depinning. For the sagging transition, the internal TPCLs remain pinned at the top edges of surface structures, while the liquid-vapor interface under droplet deforms and touches the groove bottom. The sagging transition is likely to occur on the surfaces with low structure [48]. The depinning transition occurs when the droplet gains enough energy to overcome the free energy barrier between composite and noncomposite states. As a result, the internal TPCLs are de-pinned and proceed down the structure.

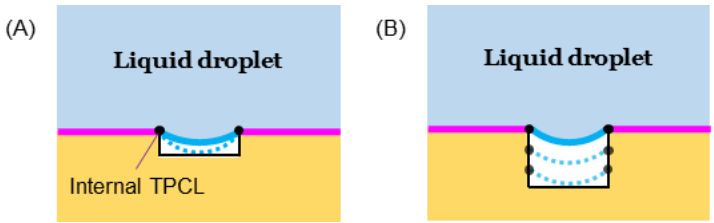


**Figure 2.5.** Schematics of wetting transition from composite to noncomposite state because of (A) the sagging of liquid-vapor interface and (B) the depinning of internal TPCL [9].

Composite state is usually featured with high contact angle and low CAH [9], which are needed for lotus superhydrophobic surfaces. Therefore, many efforts have been devoted to enhancing the stability of composite state by modifying surface structure and chemistry. For surface chemistry, post-treatment methods such as chemical or physical vapor deposition

[33, 49] and plasma treatment [50] have been used to introduce chemicals or chemical groups to reduce surface energy. For surface structures, re-entrant structures such as micro hoodoo [51] and inverted trapezoid [52], and hierarchical structures [53] are developed to stabilize the metastable composite state. These surface structures can be fabricated by techniques such as reactive ion etching followed by isotropic etching [51], 3D diffuser lithography [52], or electrospinning [53].

## 2.2 Modifying surface wettability by electrospinning

There are a few methods, such as template synthesis, sol-gel method, laser/plasma/chemical etching, layer-by-layer deposition, and electrospinning [25, 54], to modify the wettability of a solid surface. Among them, electrospinning is a facile and versatile technique to produce continuous micro- and nanofibers [55], providing adjustable surface roughness to control surface wettability [54]. Moreover, electrospinning is considered an additive manufacturing technology, allowing for surface modification on valuable substrate (e.g., for in-situ wound dressing [56]), and the introduced fibrous structure is featured with a high air permeability.

Figure 2.6 depicts a typical electrospinning setup that consists of three parts: a feeding device with a metallic needle, a high-voltage power supply, and a grounded collector [57]. The high-voltage power supply is connected to the needle, creating an electric field between the needle and grounded collector. As the polymer solution from the feeding device forms a droplet at the needle tip, surface charges are induced on the droplet, and the electrostatic repulsion of surface charges deforms the droplet into a conical shape (also known as Taylor cone) [58]. Once the supply voltage exceeds a threshold value, the electrostatic repulsion overcomes the surface tension of droplet and a charged jet (fiber) is ejected from the droplet toward the collector. The charges on the fiber induce bending instability, causing stretching of the fiber and rapid evaporation of solvent [57]. At the end of the process, the fiber reaches the collector and non-woven mat is formed. It is worth noting that single-spinneret electro-spinning may suffer from low throughput, resulting in a low production rate. This issue can be addressed by multiple-needle electrospinning [59].

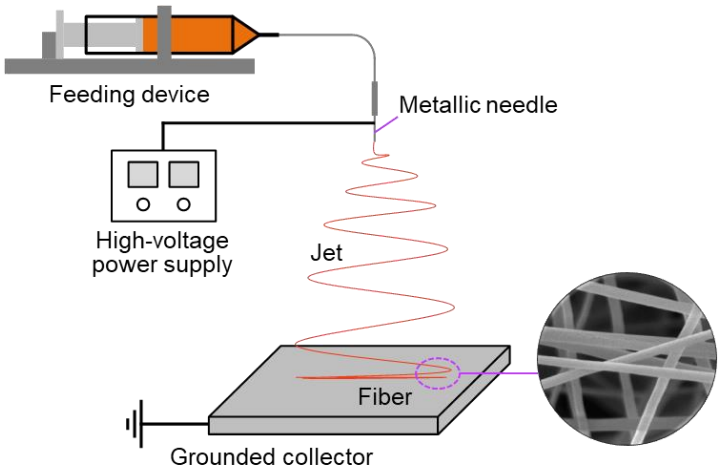


**Figure 2.6.** Schematic of a typical electrospinning setup for fiber fabrication [57]

Surface wettability is controlled by surface structure and surface energy. Based on this principle, modifying surface wettability using electrospun fibers is realized by controlling fiber morphology and/or fiber surface chemistry, which are discussed in detail as follows.

### 2.2.1 Modifying surface wettability by controlling fiber morphology

Based on surface morphology, the electrospun fibers can be categorized into (1) fibers with smooth surface and (2) fibers with secondary morphology including beads, pores, grooves, and roughness [60]. Droplets on these two types of fibers have different wetting behaviors, so they are discussed separately.

For ordinary fibers with relatively smooth surface, the diameter, inter-fiber distance, and spatial distribution of fibers can influence surface wettability. For example, Ma et al. [61] fabricated randomly distributed poly(caprolactone) (PCL) fibers with various diameters by adjusting the PCL solution concentration for electrospinning; water contact angle increases from 119˚ to 129˚ as fiber diameter decreases from 2.2 to 0.58 μm. The increase of contact angle was attributed to the higher surface roughness by thinner fibers.

Compared to fiber diameter, the inter-fiber distance and spatial distribution show greater impact on surface wettability. For example, Kakunuri et al [62] fabricate cellulose acetate nanofibers using mesh collectors with various opening sizes, i.e., 50 μm, 100 μm, and 200

μm; fibers have higher distribution density around mesh lines, i.e., 77% coverage compared to 28% coverage around mesh openings, so the fibrous mat is patterned following the mesh. As a result, the contact angle of the patterned fibrous mats increases from 90˚ to 138˚ by decreasing the mesh opening from 200 μm to 50 μm, while non-patterned mat has a contact angle of 30˚. A transition from hydrophilicity to hydrophobicity is achieved by controlling fiber spatial distribution given that the fibers have similar diameter distribution. Moreover, Bagrov et al. [63] modifies the wettability of aluminum foil by depositing nylon-11 nano-fibers with varying inter-fiber distance. Surface coverage rate of fibers increases from 0.7% to 20%, where the inter-fiber pore size is around 2.5 μm, by increasing electrospinning time from 2 min to 5 min. As a result, contact angle increases from ~70˚ to 124˚.

The large variation of contact angle in ref. [62, 63] is explained by the change of wetting state. Specifically, droplets on fibers-dressed surfaces tend to change from Wenzel state to Cassie-Baxter state with decreasing inter-fiber distance, leading to larger equilibrium contact angles. However, the influence of fiber diameter on wetting state is relatively small due to the limited adjustable range of fiber diameter by electrospinning.

Based on electrospinning, fibers with various secondary morphologies can be generated. Figure 2.7 shows the scanning electron microscope (SEM) images of (A) beaded [64], (B) porous, (C) grooved [65], and (D) wrinkled [66] fibers. These secondary morphologies are proven to have significant influences on the wetting properties of fibers.

Beaded fiber, or bead-on-string structure, which can be produced by reducing the applied voltage or the concentration of the precursor solution for electrospinning [67], can enhance the surface hydrophobicity. For example, Hong et al. [34] prepared beaded poly(vinylidene fluoride) (PVDF) fibers by reducing the concentration of PVDF solution from 25 wt%, which is for beadless fibers, to 20 wt%. The beaded fibers are featured with 5-9 μm beads and 100 -150 nm interconnected fibers, while the diameter of beadless fibers is around 960 nm. As a result, the contact angle increases from 128˚ to 150˚ [34]. The reason lies in that the large beads, as protrusions of fibrous mat, hold droplet with air pockets underneath. However,

the beaded fibers also show high CAH, indicating that there is contact between droplet and fibers along TPCL.

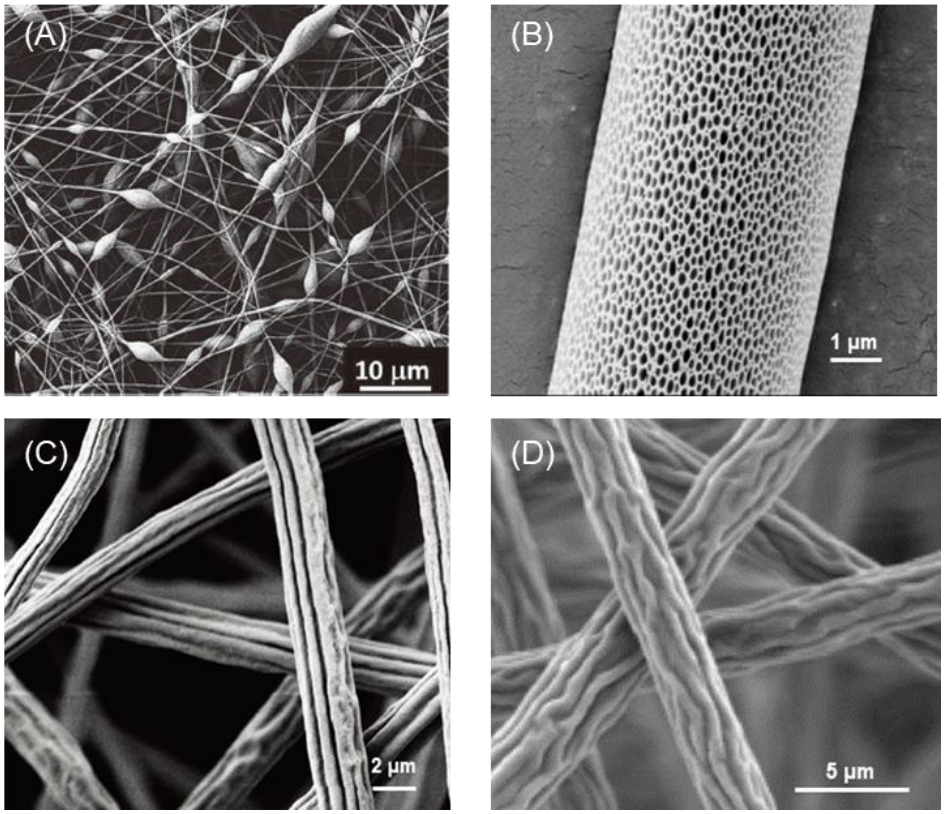


**Figure 2.7.** Scanning electron microscope image of (A) beaded [64], (B) porous, (C) grooved [65], and (D) wrinkled [66] electrospun fibers.

As another example, Wong et al. [53] used polystyrene (PS) solutions with concentration of 8 wt%, 10 wt%, and 20 wt% for electrospinning, resulting in heavily beaded fibers (~650 beads/ $mm^2$), partially beaded fibers (~160 beads /$mm^2$), and beadless fibers, respectively. The average bead diameter is 5.0 μm and 13.5 μm for heavily and partially beaded fibers, respectively. It turns out that contact angle increases from ~140˚ for beadless fibers to ~150˚ and ~160˚ for partially and heavily beaded fibers, respectively. In addition, droplets with a volume of 5 μL can roll off from the surfaces covered by beaded fibers with roll-off angles of 28˚-46˚.

Porous fibers can be fabricated by (1) phase separation of solution jets in electrospinning, (2) condensation of water vapor onto the jets in electrospinning, and (3) selective removal

of sacrificial component after electrospinning [68]. For porous fibers, a composite of solid-liquid and liquid-air interfaces may be formed at fiber surface, resulting in an increment of hydrophobicity [33]. For example, Miyauchi et al. [69] fabricated porous PS fibers based on the phase separation of solution jet in electrospinning; the solvent to prepare PS solution is a mixture of N,N-dimethylformamide (DMF) and tetrahydrofuran (THF). As a result, the pores on the fiber surface increase contact angle from 144˚, for smooth fibers, to 158˚, and decrease roll-off angle for 12 μL droplet by 25˚. Moreover, McCann et al. [70] and Ma et al. [33] have proven that porous PVDF and poly(methyl methacrylate) PMMA, respectively, fibers can also increase contact angle compared to nonporous fibers.

Different from porous fibers, a noncomposite solid-liquid contact interface can form at fiber surface for grooved or wrinkled fibers because the grooves or wrinkles may be wetted by liquid for their low structure height and large opening area [71, 72]. As a result, a higher CAH is created and contact angle may also increase with the increased fiber roughness. For instance, Liang et al. [72] compared the wetting behaviors of grooved and smooth poly(L-lactic acid) (PLLA) fibers. The grooved fibers have a contact angle of 145˚, compared with that of 135˚ for the smooth fibers. CAHs are compared by aligning fibers and measuring the difference of the roll-off angles along two directions: parallel and normal to the alignment. Consequently, the roll-off angle difference for grooved fibers is 4˚ higher than that for smooth fibers, indicating a higher CAH.

### 2.2.2 Modifying surface wettability by controlling fiber surface energy

Fiber surface energy is determined by the chemical compositions at the fiber surface. There are mainly two ways to control the surface chemistry: (1) adjust precursor solution before electrospinning, and (2) apply post treatment after electrospinning.

Polymer blending in precursor solution before electrospinning is a simple and efficient way to modify the wettability of fibrous surfaces, especially in creating superhydrophilicity. Usually, two polymers with opposite wettability, i.e., hydrophobic or weak hydrophilic and hydrophilic, are blended. For instance, Kurusu et al. [73] blended poly(styrene-*b*-(ethylene-

*co*-butylene)-*b*-styrene) (SEBS) with Pluronic F127 to turn hydrophobic electrospun SEBS fibers hydrophilic. Pure SEBS fibers have a contact angle of 139˚. By adding 15-20 wt% Pluronic F127 into SEBS solution, the obtained SEBS/F127 fibers show a contact angle of 0˚. Moreover, Li et al. [74] blended hydrophobic poly(ethylene terephthalate) (PET) and hydrophilic poly(vinyl alcohol) (PVA) in hexafluoro isopropanol (HFIP) for electrospinning. Compared with the contact angle of 131˚ for pure PET fibers, the obtained PET/PVA fibers show 0˚ contact angle even when a small amount of PVA is used, i.e., 1/20 weight of PET. However, for the polymer blending method, the change of contact angle with blending ratio is not continuous because the hydrophilic polymer tends to aggregate at fiber surface [73, 74].

In addition to the polymer blending, the precursor solution can also be adjusted by adding inorganics. In contrast with that by polymer blending, the change of contact angle by adding inorganics can be continuous. For example, Abdal-hay et al. [75] added hydroxyapatite (Hap) into nylon-6 solution for electrospinning. The nylon-6/Hap composite fibers show contact angles continuously varying from 130˚ to 0˚ with increasing Hap from 0 wt% to 10 wt%. This continuous change of contact angle can also be achieved by adding Triton X-100 non-ionic surfactant into polyamide 6 (PA6) solution [76].

Compared to adjusting precursor solution, applying post treatments after electrospinning to modify fiber surface chemistry has less restriction on applicable polymers, electrospinning parameters, etc. A few post-treatment methods have been used, including initiated chemical vapor deposition (iCVD) [33, 61], plasma etching [34], dip coating [77, 78]. For example, Ma et al. [61] used iCVD to deposit poly(perfluoroalkyl ethyl methacrylate) (PPFEMA), a low surface energy (0.0093 J/m$^2$) polymer, onto electrospun PCL fibers. After iCVD, the contact angle of PCL fibers increases from 120˚-130˚ to 150˚-160˚, and 20 μL droplets can roll off the surface at threshold tilting angles of 6˚-12˚. As another example, Schoolaert et al. [77] modified poly(2-n-propyl-2-oxazoline) (PnPrOx) nanofibers with diameter of 200-400 nm by dip-coating into tannic acid. By increasing tannic acid concentration from 0 wt%

to 10 wt%, contact angle decreases from 120˚ to 40˚. It should be noted that many relevant works also combine the modification of fiber morphology, so they are discussed in section 2.2.3 and section 2.3.

### 2.2.3 Modifying surface wettability by combining fiber morphology and surface energy

Controlling both fiber morphology and surface energy is usually aimed at creating extreme wettability, i.e., superhydrophilicity or superhydrophobicity. To develop superhydrophilic fibrous surfaces, the basic principle is to increase fiber surface energy on a rough surface. As explained by Wenzel's equation, Eq. (2.3), roughness intensifies the hydrophilicity for intrinsic hydrophilic materials.

To increase fiber surface energy, many scholars add inorganics such as metal oxides [79, 80] and silicate minerals [81] into precursor solution, followed by thermal treatment after electrospinning to expose inorganics at fiber surfaces. For example, Wang et al. [79] added $Ti(Obu)_4$ into poly(vinyl pyrrolidone) (PVP) solution for electrospinning. After calcination of as-spun fibers under 500℃, $TiO_2$ nanofibers with nanochannels on surfaces are obtained. The contact angle of 2 μL droplet reaches 0˚ within 30 ms after droplet deposition. Similarly, Zhu et al. [80] mixed $FeAc_2$ and PVA for precursor solution, and α-$Fe_2O_3$ nanofibers with rough surfaces were obtained after calcination. As a result, droplets on the α-$Fe_2O_3$ fibrous surfaces spread to 0˚ contact angle within hundreds of milliseconds. In addition, Tijing et al. [81] decorated hydrophobic polyurethane (PU) fibers with hydrophilic tourmaline I nanoparticles by adding TM nanoparticles into PU precursor solution. Without the need for thermal treatment, the as-spun beaded fibers have contact angles varying from 125˚ to 13˚ by increasing TM amount from 0 to 5 wt%.

## 2.3 Developing superhydrophobicity by electrospinning

Electrospinning is proven an efficient method for fabricating superhydrophobic surfaces. In this section, the electrospinning-based methods for fabricating superhydrophobic surfaces

are introduced. Based on the fabrication steps involved, the methods are classified into (1) one-step electrospinning and (2) electrospinning followed by post treatment.

### 2.3.1 One-step electrospinning

One-step electrospinning refers to that superhydrophobic surfaces can be directly obtained after electrospinning without any post treatment. Table 2.1 summarizes the one-step methods in literature. The first two columns explain the mechanism and materials, respectively, to achieve superhydrophobicity, and the third and fourth columns show the measured surface wettability. The mechanism is essentially controlling fiber morphology or/and fiber surface energy, as discussed in Section 2.2.

**Table 2.1.** One-step electrospinning to develop lotus superhydrophobicity

| Mechanism | Materials | Contact angle | Roll-off angle (droplet volume) | Ref. |
|---|---|---|---|---|
| Beaded fibers | PS | 160˚ | - | [27] |
| Beaded fibers | PANI/PS | 162˚ | <5˚ | [82] |
| Beaded fibers | PS | 155˚ | 5˚ | [83] |
| Beaded fibers | PVDF-HFP | 157˚ | 6˚(10 μL) | [84] |
| Beaded fibers doped with $TiO_2$ NPs | PCL/$TiO_2$ | 156˚ | - | [85] |
| Fibers with nano-protrusions | PS | 154˚ | - | [86] |
| Fibers doped with $TiO_2$ NPs or graphene NFs | PVC/$TiO_2$<br>PS/$TiO_2$<br>PVC/graphene | 168˚<br>178˚<br>166˚ | - | [87] |
| Fibers doped with $SiO_2$ NPs | PS/$SiO_2$ | 157˚ | 2.2˚[a] | [28] |
| Patterned fibers | PS | 167˚ | 5˚ (5 μL) | [88] |
| Copolymer fibers | PS-PDMS/PS | 163˚ | 15˚[a] | [31] |
| Grooved fibers with Teflon outer layer | PCL/Teflon | 158˚ | 7˚ (10 μL) | [32] |

PANI: polyaniline; PVDF-HFP: poly(vinylidene fluoride-co-hexafluoropropylene); PVC: polyvinyl chloride; PDMS: poly(methylhydrosiloxane); NPs: nanoparticles; NFs: nanoflakes.
[a]: contact angle hysteresis.

As shown in Table 2.1, most one-step methods rely on fabricating fibers with secondary morphology, especially beaded fibers, to realize lotus superhydrophobicity. A hydrophobic or weak hydrophilic polymer such as PS [27, 82, 83] and PCL [85] is often used to prepare a precursor solution that has a lower concentration than that for beadless fibers. As a result, beaded fibers with microbeads and interconnected nanofibers are obtained. When droplets are deposited on the surface, the intrinsically hydrophobic or weak hydrophilic microbeads with higher height than nanofibers can support the droplets in Cassie-Baxter state, resulting in lotus superhydrophobicity. For example, Jiang et al. [27] fabricated beaded PS fibers using 7 wt% PS/DMF solution. The diameter of beads and fibers is 3-7 μm and 60-140 nm, respectively. The bead-on-string structure increases contact angle to 160˚, compared to 139˚ for beadless fibers of 420 nm by 25 wt% PS/DMF solution. Based on Cassie-Baxter model, Eq. (2.2), the fraction of liquid-air interface is calculated to be 0.934 [27]. However, beaded fibers have high structural heterogeneity, resulting in a low mechanical strength [67] or even being hard to be free-standing [27].

Another common secondary fiber morphology in developing superhydrophobicity is the nano-protrusions on fiber surface, which are created by adding nano-particles [28, 87] or flakes [87] into the polymer solution before electrospinning. For example, Lin et al. [28] added $SiO_2$ nanoparticles into PS/DMF solution. Figure 2.8 shows the obtained PS fibers with varying content of $SiO_2$ nanoparticles. Nano-protrusions form at the fiber surfaces and increase with the content of $SiO_2$ nanoparticles. By adding 7.7 wt% and 14.3 wt% of $SiO_2$, contact angle increases from 148˚ to 153˚ and 157˚, and CAH decreases from 7˚ to 3˚ and 2˚, respectively. The obtained superhydrophobicity is attributed to the nano-protrusions and the grooves on the fiber surfaces, which held liquid from penetrating to the inside of fibrous mat. Based on similar mechanism, $TiO_2$ nanoparticles and graphene nano-flakes are doped into PS and PCL fibers for superhydrophobicity [87].

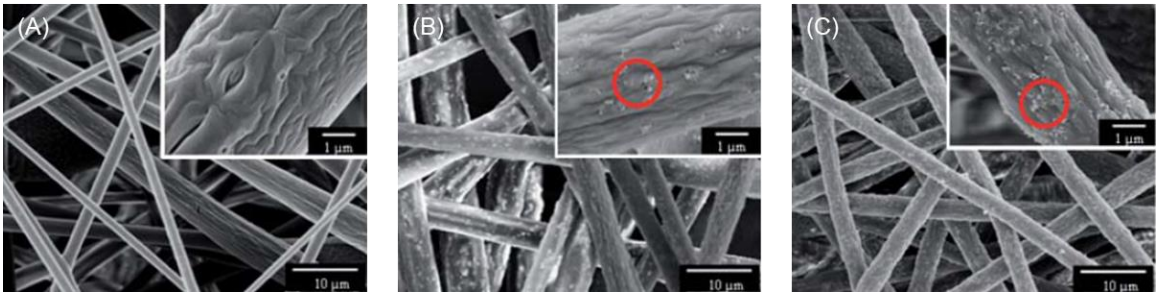


**Figure 2.8.** Electrospun PS fibers doped with (A) 0 wt%, (B) 7.7 wt%, and (C) 14.3 wt% of $SiO_2$ nanoparticles [28].

Without engineering the secondary morphologies of fibers, Wong et al. [88] proposed a method to develop superhydrophobicity by patterning smooth PS fibers. The collector for electrospinning consists of a PDMS substrate and two parallel-arranged electrodes on the top. Before electrospinning, the substrate is pre-stretched with varying strain, i.e., 0-100%. In electrospinning, PS fibers are deposited onto the pre-stretched substrate with alignment by the two parallel-arranged electrodes. After electrospinning, the pre-stretched substrate is relaxed and gets shrunk, resulting in wake-like PS fibers. By increasing the strain of pre-stretched substrate from 0% to 100%, contact angle increases from 138˚ to 167˚ and sliding angle decreases from 90˚ pinning to 5˚. The lotus superhydrophobicity can be attributed to the large curvature of the wake-like fibers, which help trap air under droplets and maintain Cassie-Baxter state.

In addition to adjusting fiber morphology, superhydrophobicity may also be reached by lowering fiber surface energy. For one-step method, this can only be realized by adopting low surface energy precursor for electrospinning. However, polymers with very low surface energy like PDMS and poly(tetrafluoroethylene) (PTFE), often have low electrospinnability. To overcome this problem, methods such as polymer blending [31, 89] and coaxial electro-spinning [32] are proposed.

As an example, Ma et al. [31] blended copolymer poly(styrene-*b*-dimethylsiloxane) (PS-PDMS) with PS for electrospinning: PDMS has a very low surface energy of 19.9 mN/m, given the lowest surface energy of 18 mN/m by PTFE [90]; PS has high electrospinnability.

The obtained PS-PDMS/PS nanofibers have diameter of 150-400 nm, with a contact angle of 163° and CAH of 15°. The high hydrophobicity is attributed to the aggregation of PDMS blocks at fiber surfaces, as verified by X-ray photoelectron spectrometer. Furthermore, Han et al. [32] produced coaxial fibers with Teflon AF as sheath and PCL as core by coaxial electrospinning. The obtained coaxial fibers have diameter of 1-2 μm with grooves on fiber surface; the coaxial structure is verified by energy-dispersive X-ray spectroscopy. As a result, the contact angle is characterized to be 158˚ and 10 μL droplets can roll off the surface at a tilting angle of ~7˚.

### 2.3.2 Electrospinning followed by post treatment

Table 2.2 summarizes the methods of electrospinning followed by post treatment to develop lotus superhydrophobicity. Most of the superhydrophobicity in Table 2.2 are developed in a way that fiber surface roughness is first modified by creating secondary morphology in electrospinning or by post treatment after electrospinning, and then fiber surface energy is reduced by coating a thin layer of low surface energy material. In other words, the super-hydrophobicity is achieved by controlling both fiber morphology and fiber surface energy.

**Table 2.2.** Electrospinning followed by post treatment for lotus superhydrophobicity

| Post treatment methods | Materials | Contact angle | Roll-off angle (droplet volume) | Ref. |
|---|---|---|---|---|
| CVD | PVDF/DMDCS | 153˚ | - | [91] |
| iCVD | PMMA/PPFEMA | 163˚ | - | [33] |
| iCVD | PCL/PPFEMA | 175˚ | 2.5˚ (20 μL) | [61] |
| Annealing | Poly(AN-co-TMI)/ fluorolink-D/T2EH | 167˚ | 4˚ (5 μL) | [92] |
| Thermal imidization | PI | 160˚ | - | [93] |
| $CF_4$ plasma etching | PVDF | 164˚ | 5˚ (12.5 μL) | [34] |
| LBL/CVD | Nylon 6/PAH/$SiO_2$ NPs/ $(CF_3)(CF_2)_5(CH_2)_2SiCl_3$ | 168˚ | - | [33] |

| | | | | |
|---|---|---|---|---|
| LBL/FAS modification | Cellulose acetate/PAA/ $TiO_2$ NPs | 162˚ | 2˚ (12 μL) | [78] |
| Calcination/fluorination | PEO/$SiO_2$ NPs/FDTS<br>PAM/$SiO_2$ NPs/FDTS<br>PAM/PS/$SiO_2$ NPs/FDTS | 160˚<br>149˚<br>152˚ | <2˚ (10 μL) | [94] |
| Calcination/FAS modification | PVA/silica gel/$SiO_2$ NPs | 155˚ | 3˚ (12 μL) | [95] |
| Dip coating | PAN/$SiO_2$ NPs/Ag/PFDT | 157˚ | - | [96] |
| Dip coating | SBS/$SiO_2$ NPs/FDTS | 156˚ | 8˚ (5 μL) | [97] |
| Dip coating/blade coating | PAN/ASO/$SiO_2$ NPs | 156˚ | - | [98] |
| Physical deposition | PU/$SiO_2$ NPs/DTMS | 157˚ | 5˚ (12 μL) | [29] |
| Surface grafting/ hydrothermal method | PU/$SiO_2$ particles | 152˚ | 5˚ (10 μL) | [30] |

CVD: chemical vapor deposition; iCVD: initiated chemical vapor deposition; LBL: layer-by-layer deposition; FAS: fluoroalkylsilane;
DMDCS: dichlorodimethyl silane; fluorolink-D: perfluorinated linear diol; T2EH: tin(ii) ethyl hexanoate; PI: polyimide; PAH: poly(allylamine hydrochloride); PAA: poly(acrylic acid); PEO: poly(ethylene oxide); FDTS: (heptadecafluoro-1, 1, 2, 2-tetrahydrodecyl)trichlorosilane; PAM: poly(acryl amide); PAN: polyacrylonitrile; PFDT: 1H,1H,2H,2H-perfluorodecanethiol; SBS: poly(styrene-b-butadiene-b-styrene) ASO: amino-silicone oil; DTMS: *n*-dodecyltrimethoxysilane.

In Table 2.2, a few secondary fiber morphologies are included: porous fibers [33], beaded fibers [34, 61, 92, 93], and nanoparticle decorated fibers [29, 30, 33, 78, 94-96, 98]. Here the nanoparticle decorated fibers are discussed in detail since porous fibers and beaded fibers are introduced in Sections 2.2.1 and 2.3.1. Nanoparticle decorated fibers can be produced by either adding nanoparticles into precursor solution before electrospinning [29, 94-96] or coating nanoparticles onto the fibers after electrospinning [30, 33, 78, 98].

For adding nanoparticles into precursor solution, the nanoparticles may be partially buried in the electrospun fibers, as shown in Figure 2.8. Post treatment by calcination can roughen fiber surfaces by pyrolysis of polymer matrix. Figure 2.9 compares the morphology of (A)

PEO/$SiO_2$ and (B) PVA /$SiO_2$ fibers before and after calcination. The calcination exposes the $SiO_2$ particles by melting or burning out the PEO or PVA, resulting in enhanced fiber surface roughness.

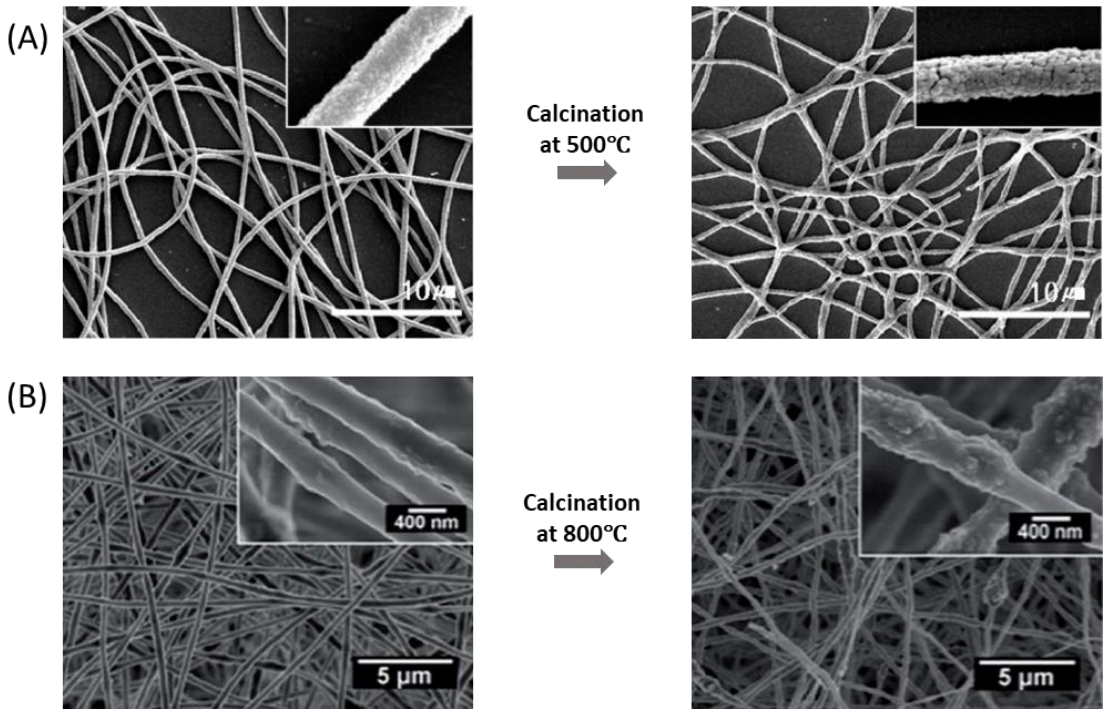


**Figure 2.9.** Change of surface morphology of (A) PEO/$SiO_2$ [94] and (B) PVA/$SiO_2$ [95] fibers before and after calcination.

Different from one-step methods, various post treatments allow to coat fibers with nano-particles after electrospinning. Figure 2.10 shows the SEM images of various electrospun fibers coated with $SiO_2$ nanoparticles by post treatments. In Figure 2.10(A), nylon-6 fibers are coated with positively charged PAH and negatively charged 50 nm $SiO_2$ nanoparticles by LBL deposition [33]. In Figure 2.10(B), PAN fibers are first modified by ASO using dip coating and then coated by 7-40 nm $SiO_2$ nanoparticles using blade coating [98]. In Figure 2.10(C), PU fibers are first grafted with -NCO group, and then treated with (3-aminoproyl) triethoxysilane (APTES), and finally coated by $SiO_2$ particles by hydrothermal method [30]. Compared with the doped fibers in Figure 2.8 and Figure 2.9, the fibers in Figure 2.10 show higher surface roughness.

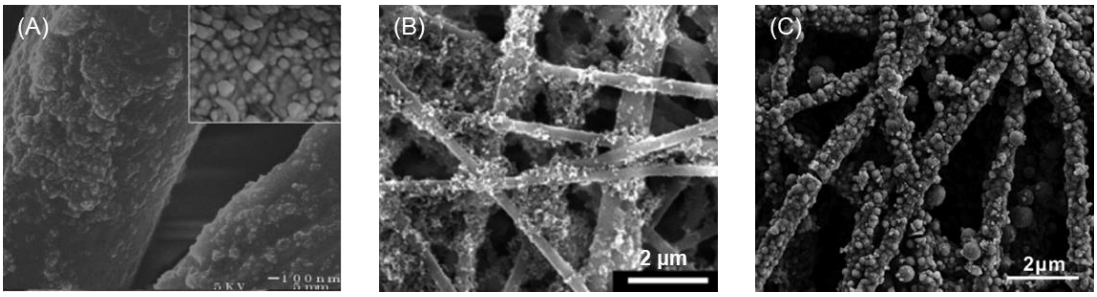


**Figure 2.10.** SEM images of (A) nylon-6 fibers [33], (B) PAN fibers [98], and (C) PU fibers [30] coated with $SiO_2$ nanoparticles after electrospinning.

After developing surface structure onto fibers, post treatment such as iCVD, dip coating, physical deposition, can coat fibers with a thin layer of low surface energy material to help maintain droplets in Cassie-Baxter state. As shown in Table 2.2, the low surface energy material can be fluoride such as PPFEMA [33, 61], FDTS [94] and PFDT [96], and silicide such as DMDCS [91]. Note that the coated layer should be thin to reserve the developed surface structure of fibers. For example, Ma et al. [33] fabricated porous PMMA microfibers with average pore size of 80 nm. The porous fibers have a contact angle of 147˚. To increase the hydrophobicity of the porous fibers, a PPFEMA layer with thickness of 30 nm is coated. As a result, the PPFEMA coated fibers retained the porous structure and show a contact angle of 163˚.

### 2.3.3 Superhydrophobicity with "rose-petal" effect

Superhydrophobicity with "rose-petal" effect, also known as sticky superhydrophobicity, is also important to many applications including microdroplet transportation/collection [18] and lap-on-chip devices [19]. On a sticky superhydrophobic surface, a droplet takes a quasi-spherical shape with contact angle greater than 150˚, so the contact area between droplet and solid surface is small. Meanwhile, the droplet can be hold in place without movement because of the high adhesive force by the surface.

Table 2.3 summarizes the electrospinning-based methods for developing rose-petal effect surfaces, which are categorized into one-step electrospinning and electrospinning followed by post treatment. The first column lists the post treatment involved; the second and third

columns list the surface morphology and the materials, respectively, of fibers; the fourth and fifth columns show the wetting behaviors on the fibers.

**Table 2.3.** Electrospinning-based methods for petal superhydrophobic surfaces

| Post-treatment | Fiber morphology | Material | Contact angle | Adhesion strength (droplet volume) | Ref. |
|---|---|---|---|---|---|
| - | Smooth fibers | CA | 154˚ | 90˚ pinning | [99] |
| - | Smooth fibers | PolyPhe | 160˚ | 180˚ pinning (2 μL) | [100] |
| - | Beaded fibers | FPI | 158˚ | 98 μN | [101] |
| - | Smooth fibers | γ-PGA-Phe | 154˚ | 180˚ pinning (1 μL) | [102] |
| - | Beaded fibers | PVDF | 150˚ | 180˚ pinning (3 μL) | [34] |
| - | Beaded fibers | PS | 152˚ | 113 μN | [53] |
| Thermal imidization | Beaded fibers | PI | 151˚ | 80 μN | [93] |
| $SiCl_4/H_2O$ treatment/ silanization | Beaded fibers | PVA/silica | 168˚[a] | 180˚ pinning (2 μL) | [103] |

CA: cellulose acetate; PolyPhe: poly(L-phenylalanine); FPI: fluorinated polyimide; γ-PGA-Phe: γ-PGA modified with *L*-phenylalanine ethylester;

[a]: advancing contact angle.

Lotus fibers require droplets staying in the Cassie-Baxter state, so a proper combination of structured fiber surface and low fiber surface energy is needed. However, for rose-petal fibers, droplets can be in partial wetting or Wenzel state. Therefore, most of the rose-petal fibers in Table 2.3 are produced by one-step electrospinning without post treatment to coat nanoparticles or low surface energy layer. For example, Figure 2.11 presents three rose-petal fibers that have smooth fiber surface and are fabricated using hydrophilic polymers. Figure 2.11(A) shows cellulose acetate, which has an intrinsic contact angle of 64˚, fibers with diameter of 350-400 nm [99]. As shown in the inset, the cellulose acetate fibers have a contact angle of 154˚ and droplets are pinned even by tilting the fibrous mat 90˚. Figure 2.11(B) and (C) are for PolyPhe [100] and γ-PGA-Phe [102] fibers, respectively. The

intrinsic contact angle of the PolyPhe and γ-PGA-Phe is 75˚ and 70˚, respectively. Both fibers have contact angle greater than 150˚ and can pin droplets at a tilting angle of 180˚.

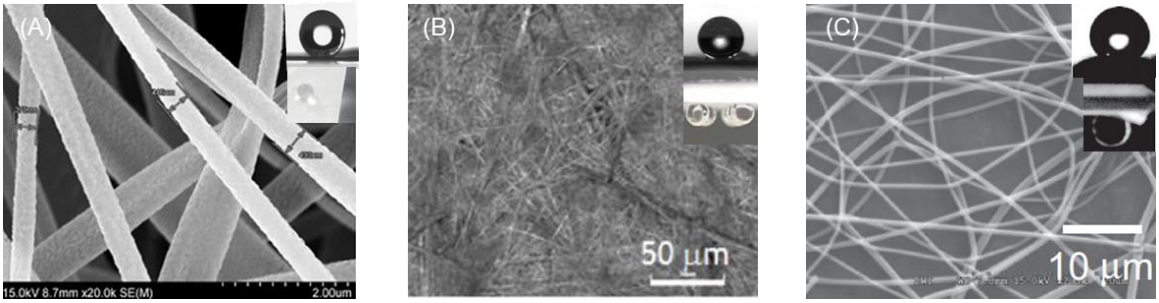


**Figure 2.11.** SEM images of superhydrophobic (A) cellulose acetate [99], (B) PolyPhe [100], and (C) γ-PGA-Phe [102] fibers with rose-petal effect.

Beaded fibers are also widely used to create rose-petal superhydrophobicity. For example, Gong et al. [101] fabricated beaded FPI fibers using one-step electrospinning. Nanopapillae form on the bead surface, increasing the surface roughness of bead. The beaded FPI fibers have contact angle of 158˚ and adhesion force of 98 μN. The high adhesion is attributed to the noncomposite interface between fibers and droplet, and the hydrophilic groups of FPI molecules. The composite interface between beads and droplet contributes to the high contact angle. In addition, beaded PVDF [34], PS [53], PI [93], and PVA/silica [103] fibers are also reported for the feasibility of developing rose-petal superhydrophobicity. Compared to the lotus beaded fibers reported in Table 2.1 and Table 2.2, rose-petal beaded fibers have higher fiber surface energy, smaller size contrast between beads and fibers, and lower distribution density of beaded fibers.

## 2.4 Summary

In this chapter, Section 2.1 provides the fundamentals of droplets wetting on flat and rough surfaces that are needed to understand various wetting phenomena. On an ideal flat surface, droplets wetting is governed by the intrinsic contact angle of surface material based on the Young equation. On a rough surface, a droplet can be in either composite or noncomposite state depending on the existence of air pockets under the droplets, and the contact angle can be predicted by Cassie-Baxter or Wenzel model, respectively. Moreover, wetting transition

from the composite state to noncomposite state may occur if composite state is not thermodynamically stable.

Section 2.2 introduces the methods to modify surface wettability using electrospinning. In essence, surface wettability is determined by surface roughness and surface energy, which can be controlled by electrospun fiber morphology and fiber surface chemistry, respectively. The fiber morphology including fiber diameter, inter-fiber distance, spatial distribution, and secondary fiber morphology such as beads, pores, and grooves are shown to be effective in controlling surface wettability. The fiber surface chemistry can be manipulated by adjusting precursor solution and applying post treatment such as CVD and dip coating to fibers.

Based on Section 2.2, Section 2.3 first reviews the electrospinning-based methods to create lotus superhydrophobicity. Based on the fabrication steps involved, the methods are classified into one-step electrospinning and electrospinning followed by post treatments.

The most commonly used one-step method is creating protrusions on fiber surfaces, i.e., beaded fibers and nanoparticle-decorated fibers. The mechanism for creating lotus effect is that the protrusions can support droplets in Cassie-Baxter state with less continuous liquid-fiber contact interface, resulting in high contact angle and low droplet adhesion. However, the beaded fibers suffer from low mechanical strength due to the high heterogeneity; complex preparation for a homogeneous solution is needed for electrospinning nanoparticle-decorated fibers. Moreover, methods using patterned fibers, coaxial or copolymer electrospinning are also reported, but limited by the complex setup or operation.

For the electrospinning followed by post treatments, most of the lotus-effect surfaces are developed in a procedure that fiber surface roughness is first modified by creating secondary fiber morphology, especially surface protrusions, in electrospinning or by post treatments, and then fiber surface energy is reduced by coating a layer of low surface energy material after electrospinning. Even though the post treatment after electrospinning allows to separate fiber fabrication and surface modification, the fabrication is complicated by the multistep process.

In comparison, developing petal-effect surfaces by electrospinning has less requirement on the fiber morphology and surface energy than that for lotus surfaces. The reason lies in that liquid can penetrate into the inter-fiber spaces so a complete Cassie-Baxter state is not needed for petal effect. Therefore, the petal effect has been achieved using both smooth and beaded fibers with a relatively high surface energy, for example, smooth cellulose acetate nanofibers with random distribution.

Despite the substantial progress in developing electrospun superhydrophobic surfaces, several limitations preventing broad applications exist. First, a strategic approach to super-hydrophobicity considering the influences of fiber morphology is needed. Currently, most works rely on increasing fiber surface roughness and/or reducing fiber surface energy with low surface energy materials to realize superhydrophobicity, so fibers are usually randomly deposited with little control. As a result, a thick fibrous mat is usually made to reduce the heterogeneity of fiber distribution, causing a decrease of air permeability and transparency, and also a waste of materials.

Second, current methods often involve complex fabrication processes. To increase fiber surface roughness, nanoparticles are widely adopted before or after electrospinning. Before electrospinning, nanoparticles should be homogeneously blended with the polymer solution, so an extra step might be needed to disperse the nanoparticles. After electrospinning, post treatment is needed to coat fibers with nanoparticles. To reduce the surface energy of fibers, copolymer (low surface energy polymer and electrospinnable polymer) or coaxial electro-spinning, or surface coating after electrospinning are often used. All these methods can increase the fabrication complexity.

# Chapter 3 An Integrated Thermodynamic Model for Wetting Various Parallel-Structured Surfaces*

## 3.1 Introduction

The wettability of a solid surface is often characterized with a sessile droplet contact angle [44, 104]. A hydrophilic surface has strong affinity to liquid, thereby showing a static contact angle less than 90˚. They are needed in anti-fogging glasses [105], heat pipes [106], contact lenses [107], etc. Conversely, a hydrophobic surface, showing a static contact angle greater than 90˚, is desirable for self-cleaning [108] and anti-icing [16] surfaces.

Patterning surfaces with parallel structures or grooves is an effective and facile method to control the wettability of solid surfaces. Structures with various cross-section shapes are fabricated, including rectangle and trapezoid structures by photolithography [109], micro-milling [110-112], and laser micromachining [113], and round structures by electrospinning [51, 114, 115]. The mechanism of modifying surface wettability by parallel structures is by changing surface roughness.

The wetting state of a liquid droplet on a rough surface can be either composite or non-composite. In composite state, which is also known as Cassie-Baxter state [41], air pockets form along the solid-liquid interface. In the noncomposite state, or Wenzel state [42], the solid surface under droplet is fully wetted by liquid. The equilibrium contact angle (ECA) on a rough surface can be predicted using Cassie-Baxter model [41] or Wenzel model [42]. In reality, however, the free energy barriers that prevent a wetting system from reaching its global minimum of free energy may deviate the actual contact angle from the ECA [44]. In addition, a free energy barrier may separate composite and noncomposite states and hinder the wetting transition between these two states [116, 117].

* The contents have been published in *Colloids and Surfaces A: Physicochemical and Engineering Aspects 655: 130214*

Therefore, the energy barriers are important to predict wetting behaviors. Many articles [51, 118-124] have reported thermodynamic models describing the change of free energy in wetting to analyze energy barrier. These models can be divided into two categories based on the calculation of the solid-liquid or liquid-vapor area under droplet. Specifically, some works calculate the solid-liquid or liquid-vapor area using a statistical distribution density of structures; the energy barriers in wetting transition for pillars [118-120], spheres [120], and micro hoodoo structures [51] are obtained. However, the energy barriers formed along the movement of exterior three-phase contact line (TPCL) are difficult to analyze with the statistical distribution density.

Alternatively, the solid-liquid or liquid-vapor area can be correlated with the position of exterior TPCL on every structure. For example, Li et al. [121] and He et al. [123] studied the energy barriers in wetting pillar structures with different top-views by calculating the energy difference between discrete positions of exterior TPCL; Tie et al. [122] studied the energy barriers in wetting trapezoid, rectangle, paraboloid, and triangle strips. However, the variation of free energy with the movement of exterior TPCL inside structure grooves was not included. Kim et al. [124] modeled the exterior TPCL moving in rectangle grooves by assuming the liquid front inside grooves as a vertical line, but this assumption cannot fit re-entrant structures, e.g., inverted trapezoid. In addition, numerically calculating the energy difference between discrete TPCL positions can only give the magnitude of energy barriers.

Besides the magnitude, the forming conditions of energy barriers are also important. For example, specifying the forming conditions of energy barrier helps to maximize metastable contact angles for superhydrophobicity [125] and analyze the advancing and receding contact angles for contact angle hysteresis [121]. To this end, Shuttleworth and Bailey [126] studied the movement of exterior TPCL on wavy surfaces (with inclination angle less than 90˚) by considering intrinsic contact angle (ICA) as local contact angle. They modeled the initiating and ending conditions of the energy barrier in noncomposite state. Later, Eick et al. [125] related free energy to apparent contact angle (APCA) as droplets spread along sawtooth

surfaces. They derived similar equations by minimizing system free energy. More recently, Long et al. [2] extended the application of the model for the initiating and ending conditions of energy barrier to parallel-structured surfaces. Moreover, other scholars model contact angle hysteresis, which is same with the initiating and ending conditions of energy barriers without external perturbations [124], for pillars [127, 128], spheres [129], and re-entrant structures [130] in composite state. However, the forming conditions of energy barrier may be discontinuous and complicated by (1) the interplay between ICA and the multiple surface inclination angles of round or quadrilateral structures, and (2) the penetration of exterior TPCL inside the grooves [114].

In addition, the reported thermodynamic models [111, 114, 122, 124] relating free energy with the exterior TPCL position for parallel structures are shape specific. There is a lack of an integrated model for various simple geometries, such as trapezoid [112, 113], rectangle [109-111], inverted trapezoid [131], circle [51, 114], and elongated circle [115]. Besides evaluating the wetting behaviors of existing structures, an integrated model can also guide the design of new structures.

Therefore, the objectives of this chapter are to build an integrated thermodynamic model relating free energy with the continuous movement of TPCLs and then specify the forming conditions of energy barrier in wetting various parallel-structured surfaces. Figure 3.1 shows the cross section of the studied parallel structures: (A) sharp-edge and (B) round structures, which are often reported in the literature. As illustrated, both types of structures are specific case of the base structure. This analysis enables the development of an integrated model in this work. Accordingly, the rest of the chapter is organized as follows. Section 3.2 introduces the thermodynamic models for different wetting states. The critical conditions for creating energy barriers are derived from the models. Then Section 3.3 validated the thermodynamic models and the forming conditions of energy barrier using experimental data by electrospun fibers and existing experimental and theoretical works. Section 3.4 compares the forming conditions and magnitude of energy barrier for various parallel structures.

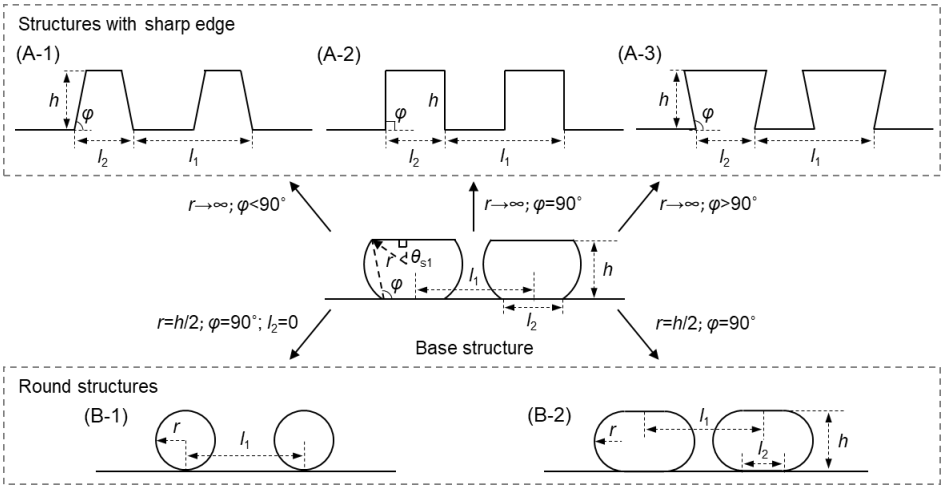


**Figure 3.1.** Cross-section view of various structures: (A-1) trapezoid; (A-2) rectangle; (A-3) inverted trapezoid; (B-1) circle; (B-2) elongated circle.

## 3.2 Theoretical Analyses

Figure 3.2 presents the schematic of a liquid droplet on a parallel-structured surface. Two-dimensional thermodynamic models relating system free energy with the position of TPCLs are built for the composite and noncomposite states, and wetting transition. The assumptions are made as follows: 1) the liquid-vapor interface 1 is treated as a circular segment with a radius of $R_1$ by ignoring the effect of gravity for droplet smaller than capillary length [132]; 2) the liquid-vapor interface 2 is assumed planar by ignoring the effect of Laplace pressure [132]; 3) the line tension is ignored so Young equation is locally valid [133]; 4) the droplet volume remains constant by ignoring droplet evaporation.

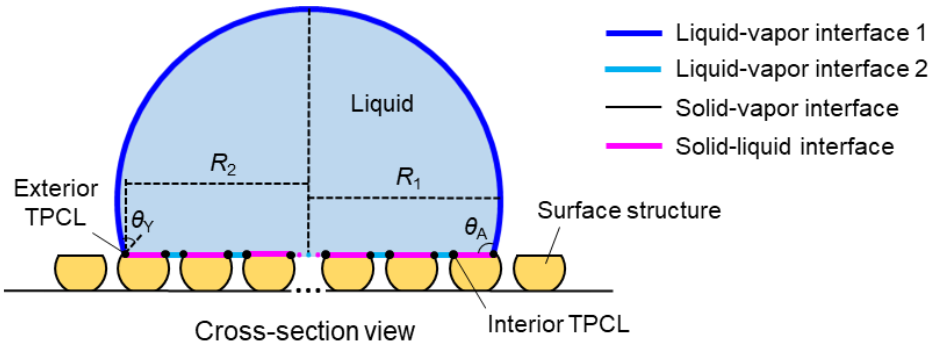


**Figure 3.2.** Schematic of a liquid droplet on a parallel-structured surface

The change of free energy per unit depth, $\Delta E$, before and after the droplet contacts the structure surface in Figure 3.2 is:

$$\Delta E = \left(L_{\mathrm{LV1}} + L_{\mathrm{LV2}}\right)\gamma_{\mathrm{LV}} + L_{\mathrm{SL}}\left(\sigma_{\mathrm{SL}} - \sigma_{\mathrm{SV}}\right) \tag{3.1}$$

where $L$ and $\gamma$ are interface length and surface tension, respectively; L, V, and S represent liquid, vapor, and solid, respectively. Then dividing Eq. (3.1) by $\gamma_{\mathrm{LV}}$ and applying the Young equation [38, 39] give

$$\Delta E/\gamma_{\mathrm{LV}} = L_{\mathrm{LV1}} + L_{\mathrm{LV2}} - L_{\mathrm{SL}}\cos\theta_{\mathrm{Y}} \tag{3.2}$$

where $\theta_{\mathrm{Y}}$ is the ICA of solid surface. For a given volume of a liquid, the system free energy before contacting and $\gamma_{\mathrm{LV}}$ are constant; thus, the $\Delta E/\gamma_{\mathrm{LV}}$ of Eq. (3.2) stands for system free energy per unit depth for the rest of this chapter. Based on the geometric relationship shown in Figure 3.2 and the constant cross-section area, $S$, of the droplet [122, 134], we have

$$L_{\mathrm{LV1}} = 2R_1\theta_{\mathrm{A}} = 2R_2\theta_{\mathrm{A}}/\sin\theta_{\mathrm{A}} \tag{3.3}$$

$$S = \left(\theta_{\mathrm{A}} - \sin\theta_{\mathrm{A}}\cos\theta_{\mathrm{A}}\right)R_2^2/\sin^2\theta_{\mathrm{A}} + S_2 \tag{3.4}$$

where $\theta_{\mathrm{A}}$ is the APCA, and $S_2$ is the area difference between the liquid below external TPCL and the structure above external TPCL to account for the liquid penetration into the grooves. The $L_{\mathrm{LV2}}$ and $L_{\mathrm{SL}}$ in Eq. (3.2) are functions of APCA and the position of TPCLs, and they depend on the wetting states, which are specified as follows.

Figure 3.3 shows the composite and noncomposite states, and wetting transition for the sharp-edge and round structures in Figure 3.1. Different from earlier 2D models [121, 122], the model in this paper considers the movements of exterior TPCL along each structure, so the energy barrier encountered at each surface can be analyzed. As the droplet spreads along the structures, the exterior TPCL moves in a cyclic pattern. The position of the exterior TPCL is described using $n$, $s$, $\delta_{\mathrm{o}}$ and $\theta_{\mathrm{o}}$: $2(n\text{-}1)$ is the number of structure units that have been fully covered by droplet; $s$ and $\delta_{\mathrm{o}}$ are the wetted length of the $n$-th structure unit along horizontal

and inclined surfaces, respectively; $\theta_o$ is the angular position of exterior TPCL. The interior TPCL uses $\delta_i$ or $\theta_i$ for inclined or curved surfaces.

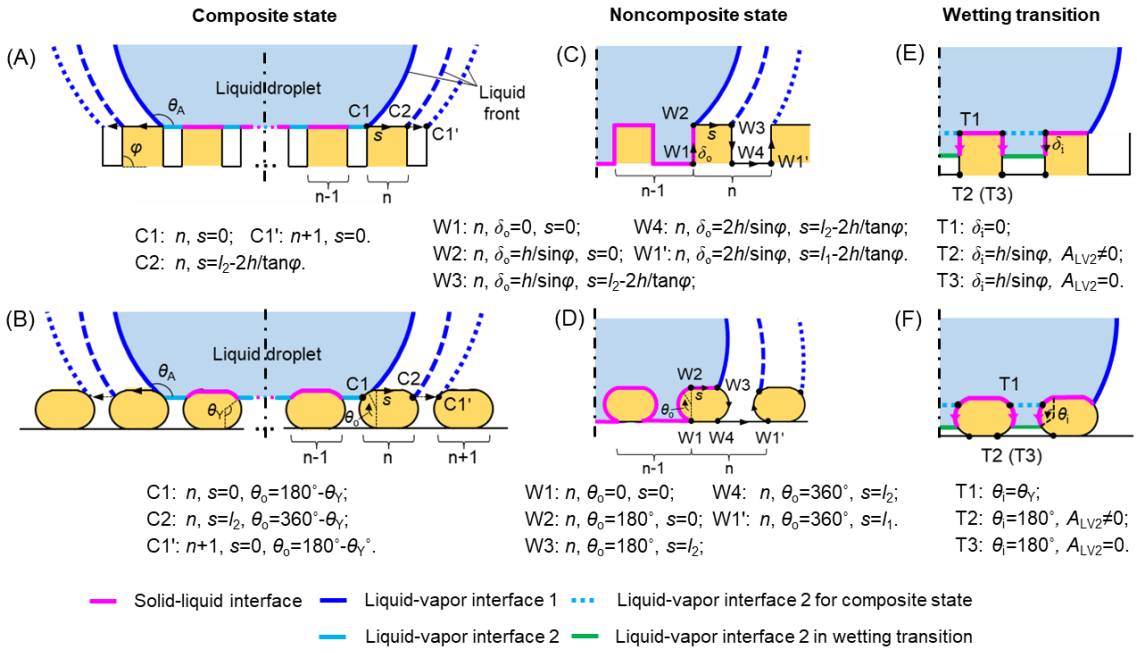


**Figure 3.3.** Schematics of composite states for the (A) sharp-edge and (B) round structures; noncomposite states for the (C) sharp-edge and (D) round structures; the wetting transition for (E) sharp-edge and (F) round structures. (trapezoid: $\varphi < 90^\circ$; rectangle: $\varphi = 90^\circ$; inverted trapezoid: $\varphi > 90^\circ$; circle: $l_2 = 0$; elongated circle: $l_2 \neq 0$)

However, a few geometry constraints limit the movement of exterior TPCL, because the liquid front cannot intercept with structures at any point besides exterior TPCL. Figure 3.4 (A) and (B) illustrate the geometry constraints for the exterior TPCL on the sharp-edge and round structures, respectively. As shown in Figure 3.4(A-1), the two green dotted lines set the boundary of the liquid front, which is denoted by the blue line. It should be noted that the liquid front inside grooves is treated as a straight line, which is tangent to the liquid front curve outside grooves [2, 114], for simplicity. As a result, there are upper and lower limits for $\theta_A$ corresponding to boundary of the liquid front.

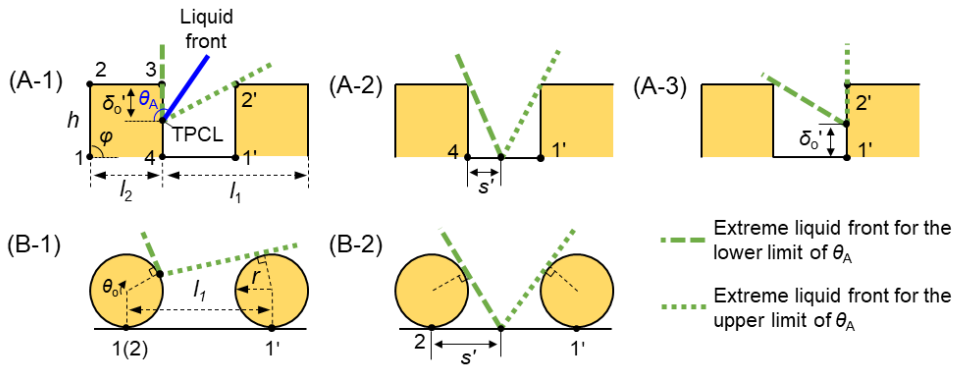


**Figure 3.4.** Geometry constraints for the movement of exterior TPCL on the (A) sharp-edge and (B) round structures

For the sharp-edge structures in Figure 3.4(A), there is no constraint for the path 2-3, i.e., when the external TPCL is on path 2-3, because 2-3 is the top surface. For the paths 3-4, 4-1′, and 1′-2′, which correspond to Figure 3.4(A-1) to (A-3), respectively, the constraints, i.e., the upper and lower limits of $\theta_A$, are expressed using Eq. (3.5), which is derived based on geometric relationships.

$$
\begin{aligned}
&3-4:\ \varphi < \theta_A < 180^\circ - \arctan\frac{\delta_o' \sin\varphi}{l_1 - l_2 + 2h/\tan\varphi - \delta_o' \cos\varphi} \\
&4-1':\ \arctan\frac{h}{h/\tan\varphi + s'} < \theta_A < 180^\circ - \arctan\frac{s'\sin\varphi}{l_1 - l_2 + h/\tan\varphi - s'} \\
&1'-2':\ \arctan\frac{h - \delta_o' \sin\varphi}{l_1 - l_2 + h/\tan\varphi + \delta_o' \cos\varphi} < \theta_A < 180^\circ - \varphi
\end{aligned}
\qquad (3.5)
$$

where $\varphi$, $l_1$, $l_2$, and $h$ are all geometry parameters as introduced in Figure 3.1; $s'$ and $\delta_o'$ are the wetted length of each horizontal and non-horizontal surfaces, respectively, by exterior TPCL. For the round structures,

$$
\begin{aligned}
&1-2: \arcsin\frac{r}{\sqrt{\left(l_1 - r\sin\theta_o\right)^2 + \left(r\cos\theta_o\right)^2}} + \arctan\frac{r\cos\theta_o}{l_1 - r\sin\theta_o} < \theta_A < \theta_o \qquad \text{if } \theta_o < 180^\circ \\
&\theta_o - 180^\circ < \theta_A < 180^\circ - \arcsin\frac{r}{\sqrt{\left(l_1 - r\sin\theta_o\right)^2 + \left(r\cos\theta_o\right)^2}} - \arctan\frac{r\cos\theta_o}{l_1 - r\sin\theta_o} \quad \text{if } \theta_o > 180^\circ \\
&2-1': 2\arctan\frac{r}{s'} < \theta_A < 180^\circ - 2\arctan\frac{r}{l_1 - s'}
\end{aligned}
\qquad (3.6)
$$

where $r$ and $l_1$ are geometry parameters; $\theta_0$ is the location of external TPCL on each round structure.

### 3.2.1 Geometric transformation

Figure 3.5 defines the geometry of the base structure in Figure 3.1. The positions of exterior and interior TPCLs are described using $\theta_o$ and $\theta_i$ in Figure 3.5 (A) and (B), respectively. In both figures, the gold (color) region represents a single base structure, and its side walls are two arcs with a radius of $r$. As $r$ approaches infinity, the arc walls become straight, so the base structure becomes a sharp-edge structure with an internal angle of $\varphi$, as shown Figure 3.1(A). With a finite $r$, the base structure becomes an elongated circle when $h = 2r$ and $\varphi = 90^{\circ}$, and then becomes a circle as $l_2$ equals zero, as shown Figure 3.1(B).

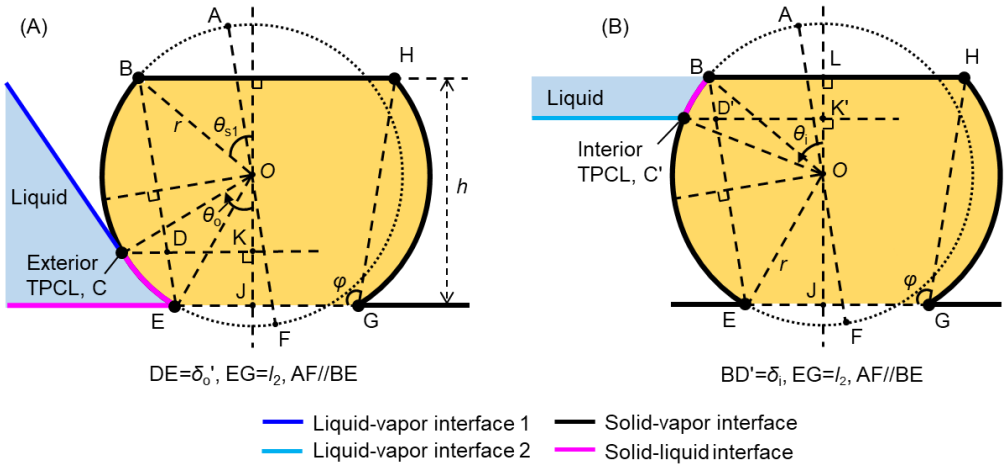


**Figure 3.5.** Geometry of the base structure in Figure 3.1 with (A) exterior and (B) interior TPCLs.

In the geometric transformation from the base to sharp-edge structures, as $r$ approaches infinity, the exterior TPCL at the point C in Figure 3.5 (A) moves right to the point D, and the interior TPCL at the point C′ in Figure 3.5 (B) moves right to the point D′. So, the heights of exterior TPCL (length of KJ) and interior TPCL (length of K′J′) are fixed at $\delta_o' \cdot \sin\varphi$ and $h - \delta_i \cdot \sin\varphi$, respectively. Then Eqs. (3.7-3.8) are obtained based on the geometric relationship of $KJ = OE \cdot \cos(\angle JOE) - OC \cdot \cos\theta_o$ and $LK' = OB \cdot \cos(\angle BOK') - OC' \cdot \cos\theta_i$, respectively.

$$\delta_{\mathrm{o}}^{'}\sin\varphi = r\cos\left(180^{\circ}-2\varphi+\theta_{\mathrm{s1}}\right)-r\cos\theta_{\mathrm{o}} \tag{3.7}$$

$$\delta_{\mathrm{i}}\sin\varphi = r\cos\theta_{\mathrm{s1}}-r\cos\theta_{\mathrm{i}} \tag{3.8}$$

where $r$, $\varphi$, and $\theta_{s1} = \varphi - \arcsin(h/(2r\sin\varphi))$ are all structure parameters. Meanwhile, for the exterior TPCL, the length of arc CE approaches $\delta_o'$ and the difference between the projections of OC and OE on CD approaches $-\delta_o'\cdot\cos\varphi$. Then the following relations can be obtained,

$$\lim_{r\to\infty} r\left(\theta_{\mathrm{o}}-180^{\circ}+\theta_{\mathrm{s2}}\right)=\delta_{\mathrm{o}}^{'} \tag{3.9}$$

$$\lim_{r\to\infty} r\sin\theta_{\mathrm{o}}-r\sin\theta_{\mathrm{s2}}=-\delta_{\mathrm{o}}^{'}\cos\varphi \tag{3.10}$$

where $\theta_{s2}$ is defined as $2\varphi-\theta_{s1}$ for $\theta_o$ <180˚, and $-\theta_{s1}$ for $\theta_o$ >180˚ to simplify Eqs. (3.9) and (3.10). Similarly, for the interior TPCL in Figure 3.5 (B),

$$\lim_{r\to\infty} r\left(\theta_{\mathrm{i}}-\theta_{\mathrm{s1}}\right)=\delta_{\mathrm{i}} \tag{3.11}$$

$$\lim_{r\to\infty} r\sin\theta_{\mathrm{i}}-r\sin\theta_{\mathrm{s1}}=\delta_{\mathrm{i}}\cos\varphi \tag{3.12}$$

The geometric relationships of Eqs. (3.7)-(3.12) are used to integrate various structures.

### 3.2.2 Composite state

In the composite state, the exterior TPCL moves in a cyclic pattern of C1-C2-C1′ as shown in Figure 3.3(A-B). Substituting Eq. (3.3) into Eq. (3.2) gives,

$$\frac{\Delta E}{\gamma_{\mathrm{LV}}}=2R_2\frac{\theta_{\mathrm{A}}}{\sin\theta_{\mathrm{A}}}+L_{\mathrm{LV2}}-L_{\mathrm{SL}}\cos\theta_{\mathrm{Y}} \tag{3.13}$$

where $R_2$, $L_{LV2}$, and $L_{SL}$ are specified based on the geometric relationships in Figure 3.3(A-B) and Figure 3.5. For the base structure, the half basal width, $R_2$, is expressed as Eq. (3.14),

$$R_2=\frac{l_1-l_2}{2}+\left(n-1\right)l_1-r\left(\sin\theta_{\mathrm{o}}-\sin\theta_{\mathrm{s2}}\right)+s \tag{3.14}$$

where $\varphi$, $l_1$, $l_2$, $h$, and $\theta_{s2}$ are geometry parameters; $n$, $s$, and $\theta_o$ describe the location of external TPCL. Note that the $r(\sin\theta_0-\sin\theta_{s2})$ and $s$ of Eq. (3.14) represent the accumulated wetting

length of the inclined and flat surfaces, respectively, in one structure unit. The liquid-vapor interface under the droplet $L_{LV2}$ is expressed as

$$L_{LV2} = (2n-1)\left[ l_1 - l_2 + \frac{2h}{\tan\varphi} - 2r(\sin\theta_i - \sin\theta_{s1}) \right] \tag{3.15}$$

where $\theta_i$ describe the location of internal TPCL. The liquid-solid interface $L_{LV2}$ is

$$L_{SL} = 2(n-1)\left( l_2 - \frac{2h}{\tan\varphi} + 2r(\theta_i - \theta_{s1}) \right) + 2r\left(\theta_o - (\theta_o)_{C1} - 2\theta_{s3}\right) + 2s \tag{3.16}$$

where $(\theta_o)_{C1}$ is the angle of initial point in the cyclic pattern of C1-C2-C1′; $\theta_{s3} = 0$ for $\theta_o < 180^\circ$ and $\theta_{s3} = \theta_{s1}$ for $\theta_o > 180^\circ$. Eqs. (3.13)-(3.16) are the integrated model for composite state.

Particularly, for the sharp-edge structures in Figure 3.1, $\delta_i = 0$; $\delta_o' = (\delta_o')_{C1} = h/\sin\varphi$ for $\theta_o < 180^\circ$ and $\delta_o' = 0$ for $\theta_o > 180^\circ$; $\theta_o = (\theta_o)_{C1} + 2\theta_{s3}$. The integrated model can be specified into the sharp-edge model by substituting Eqs. (3.10), (3.12), and (3.11) into Eqs. (3.14-3.16), respectively.

$$\begin{aligned} \frac{\Delta E}{\gamma_{LV}} = &\left[ \left( l_1 - l_2 + \frac{2h}{\tan\varphi} \right) + 2(n-1)l_1 + 2s \right] \frac{\theta_A}{\sin\theta_A} + (2n-1)\left( l_1 - l_2 + \frac{2h}{\tan\varphi} \right) - \\ &\left[ 2(n-1)\left( l_2 - \frac{2h}{\tan\varphi} \right) + 2s \right] \cos\theta_Y \end{aligned} \tag{3.17}$$

For the round structures, $\theta_i = 180^\circ - \theta_Y$ and $(\theta_o)_{C1} = \theta_Y$. The model is specified into

$$\begin{aligned} \frac{\Delta E}{\gamma_{LV}} = &\left[ l_1 - l_2 + 2(n-1)l_1 - 2r\sin\theta_o + 2s \right] \frac{\theta_A}{\sin\theta_A} + (2n-1)(l_1 - l_2 - 2r\sin\theta_Y) - \\ &\left[ 2(n-1)\left( l_2 + 2r(180^\circ - \theta_Y) \right) + 2r(\theta_o - \theta_Y) + 2s \right] \cos\theta_Y \end{aligned} \tag{3.18}$$

The next step is to analyze the variation of free energy with the exterior TPCL. The $\Delta E/\gamma_{LV}$ varies continuously as the exterior TPCL moves from C1 to C2. Then the variation of $\Delta E/\gamma_{LV}$ with $s$ for the sharp-edge structures is calculated by taking the derivative of Eq. (3.17) with respect to $s$,

$$\frac{\mathrm{d}\left(\Delta E/\gamma_{\mathrm{LV}}\right)}{\mathrm{d}s}=2R_2\frac{\mathrm{d}\left(\theta_{\mathrm{A}}/\sin\theta_{\mathrm{A}}\right)}{\mathrm{d}R_2}\frac{\mathrm{d}R_2}{\mathrm{d}s}+2\left(\frac{\theta_{\mathrm{A}}}{\sin\theta_{\mathrm{A}}}-\cos\theta_{\mathrm{Y}}\right) \tag{3.19}$$

From the derivative of Eq. (3.4), where $S_2$ is zero in composite state, with respect to $R_2$,

$$\frac{\mathrm{d}\theta_{\mathrm{A}}}{\mathrm{d}R_2}=\frac{\sin\theta_{\mathrm{A}}\left(\theta_{\mathrm{A}}-\sin\theta_{\mathrm{A}}\cos\theta_{\mathrm{A}}\right)}{R_2\left(\theta_{\mathrm{A}}\cos\theta_{\mathrm{A}}-\sin\theta_{\mathrm{A}}\right)} \tag{3.20}$$

Substituting Eq. (3.20) into Eq. (3.19) gives,

$$\frac{\mathrm{d}\left(\Delta E/\gamma_{\mathrm{LV}}\right)}{\mathrm{d}s}=2\left(\cos\theta_{\mathrm{A}}-\cos\theta_{\mathrm{Y}}\right) \tag{3.21}$$

Then the variation of $\Delta E/\gamma_{\mathrm{LV}}$ with $s$ from C1 to C2 can be determined as,

$$\begin{cases}\dfrac{\mathrm{d}\left(\Delta E/\gamma_{\mathrm{LV}}\right)}{\mathrm{d}s}<0 & \theta_{\mathrm{A}}>\theta_{\mathrm{Y}}\\ \dfrac{\mathrm{d}\left(\Delta E/\gamma_{\mathrm{LV}}\right)}{\mathrm{d}s}>0 & \theta_{\mathrm{A}}<\theta_{\mathrm{Y}}\end{cases} \tag{3.22}$$

Based on the same method, Eq. (3.23) can be obtained for C1-C2 of the round structures,

$$\begin{cases}\dfrac{\mathrm{d}\left(\Delta E/\gamma_{\mathrm{LV}}\right)}{\mathrm{d}\theta_{\mathrm{o}}}<0 & \theta_{\mathrm{A}}-\left(180^\circ-\theta_{\mathrm{Y}}\right)<\theta_{\mathrm{o}}<\theta_{\mathrm{A}}+\left(180^\circ-\theta_{\mathrm{Y}}\right)\\ \dfrac{\mathrm{d}\left(\Delta E/\gamma_{\mathrm{LV}}\right)}{\mathrm{d}\theta_{\mathrm{o}}}>0 & \theta_{\mathrm{o}}<\theta_{\mathrm{A}}-\left(180^\circ-\theta_{\mathrm{Y}}\right)\ \textit{or}\ \theta_{\mathrm{o}}>\theta_{\mathrm{A}}+\left(180^\circ-\theta_{\mathrm{Y}}\right)\end{cases} \tag{3.23}$$

For either type of structure, the exterior TPCL jumps from C2 to C1′ because there is no intermediate point in between. From Eq. (3.17), the change of $\Delta E/\gamma_{\mathrm{LV}}$ from C2 to C1′ is expressed as

$$\Delta\left(\frac{\Delta E}{\gamma_{\mathrm{LV}}}\right)_{\mathrm{C2\text{-}C1'}}=2\left(l_1-l_2+\frac{2h}{\tan\varphi}\right)+\left(\frac{2R_2\theta_{\mathrm{A}}}{\sin\theta_{\mathrm{A}}}\right)_{\mathrm{C1'}}-\left(\frac{2R_2\theta_{\mathrm{A}}}{\sin\theta_{\mathrm{A}}}\right)_{\mathrm{C2}} \tag{3.24}$$

The derivative of $2R_2\theta_{\mathrm{A}}/\sin\theta_{\mathrm{A}}$ with respect to $R_2$ is

$$\frac{\mathrm{d}\left(2R_2\theta_{\mathrm{A}}/\sin\theta_{\mathrm{A}}\right)}{\mathrm{d}R_2}=2\frac{\theta_{\mathrm{A}}}{\sin\theta_{\mathrm{A}}}+2R_2\frac{\sin\theta_{\mathrm{A}}-\theta_{\mathrm{A}}\cos\theta_{\mathrm{A}}}{\sin^2\theta_{\mathrm{A}}}\frac{\mathrm{d}\theta_{\mathrm{A}}}{\mathrm{d}R_2} \tag{3.25}$$

Substituting Eq. (3.20) into Eq. (3.25) gives

$$\frac{\mathrm{d}\left(2R_2\theta_\mathrm{A}/\sin\theta_\mathrm{A}\right)}{\mathrm{d}R_2} = 2\cos\theta_\mathrm{A} \tag{3.26}$$

Then Eq. (3.24) can be re-written as

$$\Delta\left(\frac{\Delta E}{\gamma_\mathrm{LV}}\right)_{\mathrm{C2\text{-}C1'}} = 2\left(\left(l_1 - l_2 + \frac{2h}{\tan\varphi}\right) + \int_{R_2}^{R_2+\left(l_1-l_2+\frac{2h}{\tan\varphi}\right)} \cos\theta_\mathrm{A}\,\mathrm{d}R_2\right) \tag{3.27}$$

where $\cos\theta_\mathrm{A}$ is higher than -1, so the integration is always larger than $-(l_1-l_2+2h/\tan\varphi)$. As a result, $\Delta(E/\gamma_\mathrm{LV})_{\mathrm{C2\text{-}C1'}}$ is always positive, indicating that free energy increases from C2 to C1′.

Figure 3.6 illustrates the general approach to determine the forming conditions of energy barrier. After calculating the critical APCAs, the full APCA range, [0˚, 180˚], is divided into several sub-ranges by the critical APCAs. The next step is to determine the local minima of free energy, which indicate the formation of energy barrier, by analyzing the variation of $\Delta E/\gamma_\mathrm{LV}$ along one movement cycle of external TPCL for each APCA sub-range. Then the APCA sub-ranges that form energy barrier are located and the forming conditions of energy barrier are specified. Take the sharp-edge structures in composite state as an example. The critical APCA of $\theta_\mathrm{Y}$ from Eq. (3.22) divides the full APCA range into [0˚, $\theta_\mathrm{Y}$] and [$\theta_\mathrm{Y}$, 180˚]. In [0˚, $\theta_\mathrm{Y}$], $\Delta E/\gamma_\mathrm{LV}$ keeps decreasing as the external TPCL moves from C1-C2-C1′. In [$\theta_\mathrm{Y}$, 180˚], $\Delta E/\gamma_\mathrm{LV}$ first decreases along C1-C2 and then increases along C2-C1′, creating a local minima at C2 and an energy barrier forms. For a higher accuracy, unrealistic energy barriers due to the geometry constraints (*see* Figure 3.4) for TPCL should be removed.

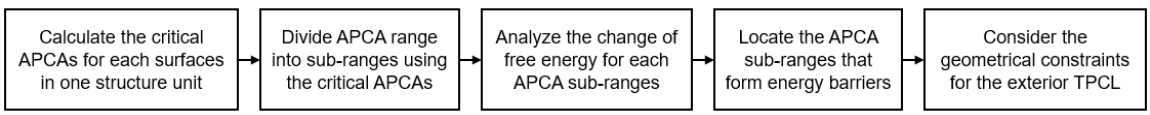


**Figure 3.6.** Procedure to specify the forming conditions of energy barrier

In the composite state, the forming conditions of energy barrier are as follows. For the sharp-edge structures, energy barrier forms when APCA is greater than $\theta_Y$, i.e., [$\theta_Y$, 180˚]. The round structures can extend the range of APCA for energy barrier to [$2\theta_Y - 180^\circ$, 180˚] because the surface of a round structure has continuous inclination angles to the horizontal plane. However, the APCA range for round structures may shrink because of the geometry constraints, which can only be determined with known structure parameters and thereby presented as part of the results in Section 3.4.

### 3.2.3 Noncomposite state

Figure 3.3(C-D) present the noncomposite state. In this case, exterior TPCL can enter the grooves and move in the cyclic pattern of W1-W2-W3-W4-W1′ or W1-W2-W1′ for circle. Mathematically, $L_{LV2}$ =0 for no liquid-vapor interface under droplet, resulting in

$$\frac{\Delta E}{\gamma_{LV}} = 2R_2 \frac{\theta_A}{\sin\theta_A} - L_{SL}\cos\theta_Y \tag{3.28}$$

where $R_2$ and $L_{SL}$ are specified based on the geometric relationships in Figure 3.3(C-D) and Figure 3.5. The half basal width $R_2$ is the same with that for composite state, as expressed in Eq. (3.14). The liquid-solid interface $L_{LV2}$ is

$$L_{SL} = l_1 - l_2 + 2(n-1)\left[l_1 - \frac{2h}{\tan\varphi} + 2r\left(\theta_i - \theta_{s1}\right)\right] + 2r\left(\theta_o - \left(\theta_o\right)_{W1} - 2\theta_{s3}\right) + 2s \tag{3.29}$$

where $(\theta_o)_{W1}$ is the angle of initial point in the noncomposite cyclic pattern; $\theta_{s3} = 0$ for $\theta_o$ <180˚ and $\theta_{s3} = \theta_{s1}$ for $\theta_o$ >180˚. Eqs. (3.28), (3.14) and (3.29) are the integrated model for noncomposite state. Particularly, $\delta_i = h/\sin\varphi$ and $(\delta_e)_{W1} = 0$ for the sharp-edge structures. The integrated model becomes the sharp-edge model by substituting Eqs. (3.10) and (3.11) into Eqs. (3.14) and (3.29), respectively.

$$\frac{\Delta E}{\gamma_{LV}} = 2R_2 \frac{\theta_A}{\sin\theta_A} - \left[l_1 - l_2 + 2(n-1)(l_1 - \frac{2h}{\tan\varphi} + \frac{2h}{\sin\varphi}) + 2\delta_o + 2s\right]\cos\theta_Y \tag{3.30}$$

For the round structures, $\theta_i = 180^\circ$ and $(\theta_o)_{W1} = 0^\circ$. The model is specified into

$$\frac{\Delta E}{\gamma_{LV}} = 2R_2 \frac{\theta_A}{\sin\theta_A} - \left[ l_1 - l_2 + 2(n-1)(l_1 - \frac{2h}{\tan\varphi} + 2\pi r) + 2r\theta_o + 2s \right] \cos\theta_Y \qquad (3.31)$$

For both the sharp-edge and round structures, the variations of $\Delta E/\gamma_{LV}$ with $s$ along W2-W3 and W4-W1′ (or W2-W1′ for circle) are the same as that for C1-C2. For W2-W3 and W4-W1′, Eq. (3.4) becomes

$$\begin{aligned} &\text{W2-W3:}\ R_0^2\pi = R_2^2 \frac{\theta_A - \sin\theta_A \cos\theta_A}{\sin^2\theta_A} + (2n-1) S_{groove} \\ &\text{W4-W1':}\ R_0^2\pi = R_2^2 \frac{\theta_A - \sin\theta_A \cos\theta_A}{\sin^2\theta_A} - 2nS_{structure} \end{aligned} \qquad (3.32)$$

where $S_{groove}$ is the cross-section area of single groove between two adjacent structures, and $S_{structure}$ is the cross-section area of one structure. However, $S_{groove}$ and $S_{structure}$ are constants when TPCL moves from W2 to W3 or W4-W1′, respectively. Thus, Eqs. (3.20) and (3.22) are still valid.

For W3-W4 of the sharp-edge structures, $\Delta E/\gamma_{LV}$ with $\delta_o$, so Eq. (3.30) is specified as,

$$\frac{\Delta E}{\gamma_{LV}} = 2R_2 \frac{\theta_A}{\sin\theta_A} - \left[ l_1 - l_2 + 2(n-1)(l_1 - \frac{2h}{\tan\varphi} + \frac{2h}{\sin\varphi}) + 2\left( l_2 - \frac{2h}{\tan\varphi} + \frac{h}{\sin\varphi} \right) + 2\delta_o \right] \cos\theta_Y \qquad (3.33)$$

The derivative of Eq. (3.33) with respect to $\delta_o$ is

$$\frac{d(\Delta E/\gamma_{LV})}{d\delta_o} = 2R_2 \frac{\sin\theta_A - \theta_A \cos\theta_A}{\sin^2\theta_A} \frac{d\theta_A}{d\delta_o} + 2\left( \cos\varphi \frac{\theta_A}{\sin\theta_A} - \cos\theta_Y \right) \qquad (3.34)$$

The Eq. (3.4) becomes

$$R_0^2\pi = R_2^2 \frac{\theta_A - \sin\theta_A \cos\theta_A}{\sin^2\theta_A} + (2n-1) S_{groove'} - 2nS_{structure'} \qquad (3.35)$$

where $S_{groove'}$ and $S_{structure'}$ are the partial area of groove and structure, respectively, as shown in Figure 3.7. From Figure 3.7, the following relationship can be obtained,

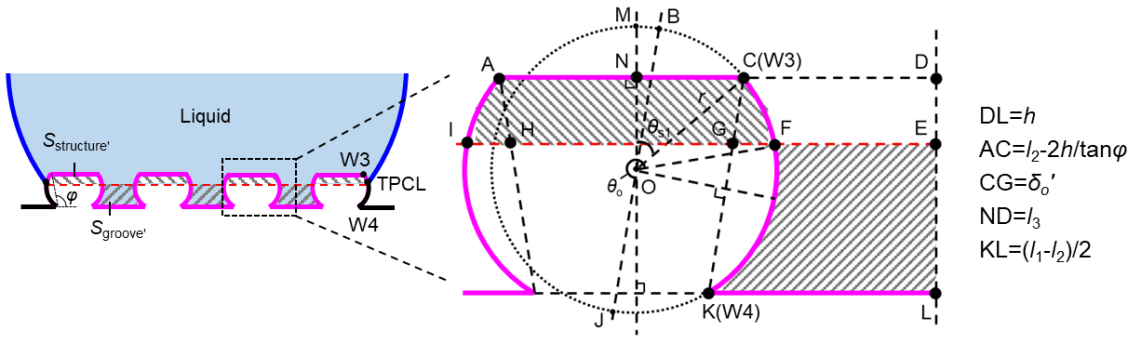


**Figure 3.7.** Schematics of $S_{groove'}$ and $S_{structure'}$ for the base structure.

$$S_{structure'} = S_{AHGC} + 2S_{CGF} \tag{3.36}$$

where $S_{AHGC}$ and $S_{CGF}$ are expressed as Eqs. (3.37) and (3.38), respectively, based on the geometric relationships shown in the inset of Figure 3.7.

$$S_{AHGC} = \left( l_2 - \frac{2h}{\tan\varphi} + \delta_o' \cos\varphi \right) \delta_o' \sin\varphi \tag{3.37}$$

$$S_{CGF} = \frac{r^2}{2}\left[ \theta_o - \pi - \theta_{s1} + \frac{1}{2}\sin(2\theta_{s1}) - \frac{1}{2}\sin(2\theta_o) \right] - \left( r\sin\theta_{s1} + \frac{1}{2}\delta_o' \cos\varphi \right) \delta_o' \sin\varphi \tag{3.38}$$

For $S_{groove'}$, point K can be treated as the location of the interior TPCL. Then $S_{groove'}$ can be calculated by

$$S_{groove'} = 2S_{EFKL} = 2l_3\left(\delta_i - \delta_o'\right)\sin\varphi - r^2\left[ \theta_o - \pi - \theta_{s1} - \theta_i - \frac{1}{2}\sin\theta_o + \frac{1}{2}\sin(2\theta_i + 2\theta_{s1}) \right] \tag{3.39}$$

where $l_3$ is expressed by $l_1/2 - l_2/2 + h/\tan\varphi + r\sin\theta_{s1}$. In composite state, $\theta_i = \pi - \theta_Y$ or 0 when there is no penetration of droplet. In noncomposite state, $\theta_i = 2(\varphi - \theta_{s1})$. In wetting transition, $\theta_i$ varies with penetration depth. For the sharp-edge structures in noncomposite state, $S_{groove'}$ and $S_{structure'}$ are specified as

$$\begin{aligned} S_{structure'} &= \delta_o'\left( l_2 - \frac{2h}{\tan\varphi} + \delta_o'/\tan\varphi \right) \\ S_{groove'} &= \left(h - \delta_o'\right)\left(l_1 - l_2 + \left(h - \delta_o'\right)/\tan\varphi\right) \end{aligned} \tag{3.40}$$

After substituting Eq. (3.40) into Eq. (3.35), Eq. (3.41) is obtained from the derivative of Eq. (3.35) with respect to $\delta_o'$ (same with $\delta_o$ for derivative).

$$\frac{\mathrm{d}\theta_A}{\mathrm{d}\delta_o} = \frac{\sin^3\theta_A \sin\varphi - \sin\theta_A \cos\varphi\left(\theta_A - \sin\theta_A \cos\theta_A\right)}{R_2\left(\sin\theta_A - \theta_A \cos\theta_A\right)} \tag{3.41}$$

Substituting Eq. (3.41) into Eq. (3.34) gives

$$\frac{\mathrm{d}\left(\Delta E/\gamma_{LV}\right)}{\mathrm{d}\delta_o} = 2\left(\cos\left(\theta_A - \varphi\right) - \cos\theta_Y\right) \tag{3.42}$$

Solving $\mathrm{d}(\Delta E/\gamma_{LV})/\mathrm{d}\delta_o > 0$ and $\mathrm{d}(\Delta E/\gamma_{LV})/\mathrm{d}\delta_o < 0$ for Eq. (3.42) gives

$$\begin{cases} \dfrac{\mathrm{d}\left(\Delta E/\gamma_{LV}\right)}{\mathrm{d}\delta_o} > 0 & \varphi - \theta_Y < \theta_A < \varphi + \theta_Y \\ \dfrac{\mathrm{d}\left(\Delta E/\gamma_{LV}\right)}{\mathrm{d}\delta_o} < 0 & \theta_A < \varphi - \theta_Y \ \textit{or}\ \varphi + \theta_Y < \theta_A \end{cases} \tag{3.43}$$

For W1-W2, Eq. (3.44) can be obtained by the same derivation method with that of W3-W4.

$$\frac{\mathrm{d}\left(\Delta E/\gamma_{LV}\right)}{\mathrm{d}\delta_o} = 2\left(\cos\left(\theta_A + \varphi\right) - \cos\theta_Y\right) \tag{3.44}$$

Solving $\mathrm{d}(\Delta E/\gamma_{LV})/\mathrm{d}\delta_o > 0$ and $\mathrm{d}(\Delta E/\gamma_{LV})/\mathrm{d}\delta_o < 0$ for Eq. (3.44) gives

$$\begin{cases} \dfrac{\mathrm{d}\left(\Delta E/\gamma_{LV}\right)}{\mathrm{d}\delta_o} < 0 & \theta_Y - \varphi < \theta_A < 360° - \left(\varphi + \theta_Y\right) \\ \dfrac{\mathrm{d}\left(\Delta E/\gamma_{LV}\right)}{\mathrm{d}\delta_o} > 0 & \theta_A < \theta_Y - \varphi \text{ or } 360° - \left(\varphi + \theta_Y\right) < \theta_A \end{cases} \tag{3.45}$$

For the round structures, the critical APCAs are the same as those shown in Eq. (3.23). However, the restriction of $\theta_Y < \theta_o < 360^\circ - \theta_Y$ in composite state is unneeded in noncomposite state. Thus, a local minimum of $\Delta E/\gamma_{LV}$ at $\theta_o = \theta_A + (180^\circ - \theta_Y)$ can be attained for each round structure.

The forming conditions of energy barrier in noncomposite state depend on the ICA and structure parameters because the relative size of the multiple critical APCAs is needed for the procedure in Figure 3.6. Therefore, a case study is shown in Section 3.4 to illustrate the use of this model.

### 3.2.4 Wetting transition

Figure 3.3(E-F) shows the wetting transition from composite to noncomposite state: liquid penetrates into the surface grooves, and finally the liquid-vapor interface under the droplet disappears. The level of penetration is described by the position of the interior TPCL, i.e., the penetration length ($\delta_i$) and angle ($\theta_i$) for the inclined and curved surfaces, respectively. Additionally, the exterior TPCLs are fixed at C2 in the wetting transition.

Considering that the exterior TPCLs are fixed at C2, the free energy per unit depth for the base structure at any penetration level between T1 and T2 is calculated by Eq. (3.46), which is derived from Eqs. (3.14)-(3.16).

$$\begin{aligned}\frac{\Delta E}{\gamma_{LV}} = {} & 2R_2\frac{\theta_A}{\sin\theta_A} + (2n-1)\left(l_1 - l_2 + \frac{2h}{\tan\varphi} - 2r\left(\sin\theta_i - \sin\theta_{s1}\right)\right) - \\ & \left[2n\left(l_2 - \frac{2h}{\tan\varphi}\right) + 2(2n-1)r\left(\theta_i - \theta_{s1}\right) + 2r\left(\theta_o - (\theta_o)_{C1} - 2\theta_{s3}\right)\right]\cos\theta_Y\end{aligned} \tag{3.46}$$

where $r(\theta_o - (\theta_o)_{C1} - \theta_{s3})$ is constant. Particularly, $(\delta_i)_{C1}=0$ for the sharp-edge structures and $(\theta_i)_{C1}=180^\circ-\theta_Y$ for the round structures. Then the variation of free energy per unit depth is analyzed by differentiating $\Delta E/\gamma_{LV}$ with respect to $\theta_i$. Solving $d(\Delta E/\gamma_{LV})/d\theta_i=0$ leads to

$$\cos\theta_i + \cos\theta_Y = -\frac{\sin\theta_A}{2R_2}\left[l_1 - l_2 + \frac{2h}{\tan\varphi} - 2r\left(\sin\theta_i - \sin\theta_{s1}\right)\right]\sin\theta_i \tag{3.47}$$

In the case of neglecting the influence of liquid penetration (into grooves) on $\theta_A$ [133], $\theta_A$ can be treated constant. Then the right side of Eq. (3.47), from the $d(2R_2\theta_A/\sin\theta_A)/d\theta_i$, becomes zero. Then for the sharp-edge structures, $\Delta E/\gamma_{LV}$ increases from T1 to T2 when $\theta_Y > 180^\circ - \varphi$, leading to an energy barrier. For the round structures, $\Delta E/\gamma_{LV}$ always increases from T1 to T2 because $180^\circ - \theta_Y < \theta_i < 180^\circ$, so an energy barrier forms too.

From T2 to T3, the liquid-vapor interface 2 disappears ($L_{LV2}$ =0), so the change of free energy per unit depth is

$$\Delta\left(\frac{\Delta E}{\gamma_{LV}}\right)_{T2\text{-}T3} = -\left(2n-1\right)\left(l_1 - l_2\right)\left(1+\cos\theta_Y\right) \tag{3.48}$$

where $(\Delta E/\gamma_{LV})_{T3}$ is calculated by Eq. (3.28). The Eq. (3.48) is always negative, indicating that T2-T3 process is thermodynamically spontaneous. Conversely, $\Delta(E/\gamma_{LV})_{T3\text{-}T2}$ is the free energy barrier to be overcome for the transition from noncomposite to composite states.

Then we evaluate the stability at T1, which corresponds to the composite state, by the difference between $(\Delta E/\gamma_{LV})_{T1}$ from Eq. (3.46) and $(\Delta E/\gamma_{LV})_{T3}$:

$$\begin{aligned}\Delta\left(\frac{\Delta E}{\gamma_{LV}}\right)_{T1\text{-}T3} &= -\left(2n-1\right)\left(l_1 - l_2 + \frac{2h}{\tan\varphi} - 2r\left(\sin\left(\theta_i\right)_{T1} - \sin\theta_{s1}\right)\right) + \\ 2R_2\left[\left(\frac{\theta_A}{\sin\theta_A}\right)_{T3} - \left(\frac{\theta_A}{\sin\theta_A}\right)_{T1}\right] &+ \left(2n-1\right)\left[2r\left(\left(\theta_i\right)_{T1} - \left(\theta_i\right)_{T3}\right) - \left(l_1 - l_2\right)\right]\cos\theta_Y\end{aligned} \tag{3.49}$$

where a positive $\Delta(E/\gamma_{LV})_{T1\text{-}T3}$ indicates a stable composite state, while a negative $\Delta(E/\gamma_{LV})_{T1\text{-}T3}$ indicates either a metastable or unstable composite state. Particularly, for the sharp-edge structures, $(\delta_i)_{T1}$=0 and $(\delta_i)_{T3} = h/\sin\varphi$. Then neglecting the change of $\theta_A$ and equating Eq. (3.49) to zero give

$$\cos\theta_Y = -\frac{l_1 - l_2 + 2h\cot\varphi}{l_1 - l_2 + 2h\csc\varphi} \tag{3.50}$$

For the round structures, $(\theta_i)_{T1}$ =180˚$-\theta_Y$ and $(\theta_i)_{T3}$ =180˚. Then Eq. (3.51) is obtained.

$$\cos\theta_Y = -\frac{l_1 - l_2 + 2r\sin\theta_Y}{l_1 - l_2 + 2r\theta_Y} \tag{3.51}$$

## 3.3 Model validation

The preceding models are validated using data in the literature and those experimentally obtained in our lab. First, the thermodynamic model is validated with experimental data in reference. Then the forming conditions of energy barriers in noncomposite state are verified

with an existing model and validated by experimental data using electrospun microfibers. Last, the model for wetting transition is validated with an existing model and experimental data from the literature.

Figure 3.8 compares our thermodynamic model for composite state with the experiment data and theoretical models from Ding *et al*. [110] for rectangle structures and Wang *et al.* [113] for trapezoid structures in terms of the equilibrium contact angle (ECA). Specifically, our model relates free energy to APCA, so ECA can be predicted by the global minimization of free energy. Our model accurately interprets the experiment data with mean differences of 1.85% for rectangles (vs. 3.49% in ref. [110]) and 1.89% for trapezoids (vs. 3.06% in ref. [113]), respectively. Thus, our thermodynamic model is validated and can be used to analyze free energy barrier.

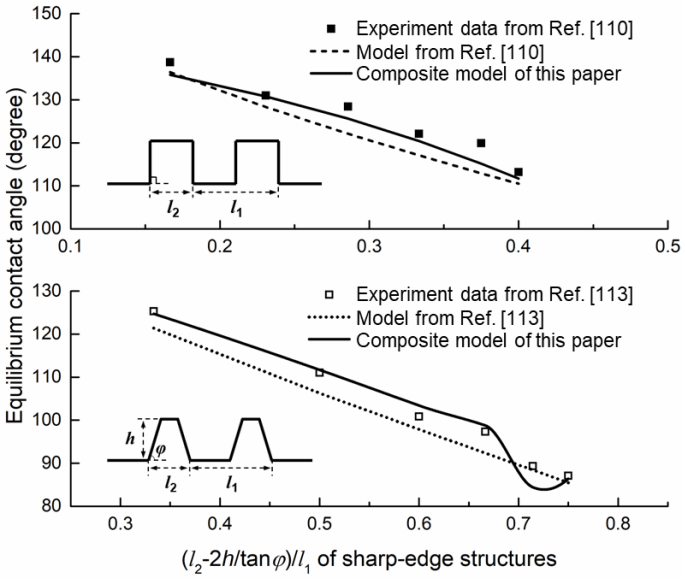


**Figure 3.8.** Validation of the thermodynamic model with experimental data in the literature [110, 113].

Figure 3.9 shows the verification of our model for the forming conditions of free energy barrier with the model from Eick *et al*. [125]. The forming conditions of energy barrier for sharp-edge structures in the noncomposite state are specified using Eqs. (3.22), (3.44), and (3.45) and following the procedure in Figure 3.6. Here we use hydrophobic materials (i.e.,

120˚> $\theta_Y$ >90˚) as an example. Three critical APCAs from the Eqs. (3.22), (3.44), and (3.45) divide the full APCA range of [0˚, 180˚] into four sub-ranges. The variation of free energy in each sub-range is analyzed for the cyclic pattern of W1-W2-W3-W4-W1′ to determine the formation of energy barriers. As a result, the solid lines with arrows denote our model for sharp-edge structures, covering triangle, trapezoid, rectangle, and inverted trapezoid as $\varphi$ increases from arctan($2h/l_2$) to 90˚ or greater. The line with stars shows the model for triangle reported by Eick *et al*. [125], and it coincides with our model for the triangle case. Thus, our model is partially verified, and our model can extend to quadrilateral structures. It should be noted that the forming conditions of energy barriers are discontinuous when $\theta_Y$ >180˚– $\varphi$/2 because of the monotonical variation of free energy for $\theta_Y$ >$\theta_A$ >180˚–|180˚– $\theta_Y$– $\varphi$|.

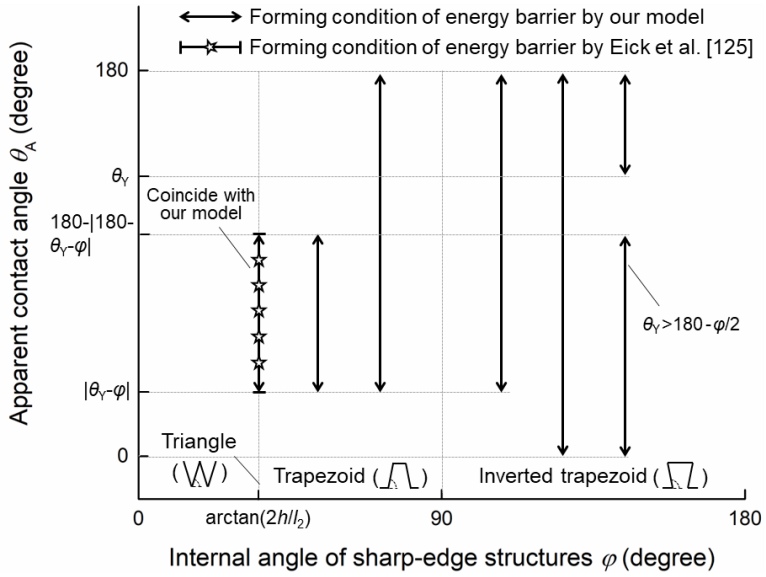


**Figure 3.9.** Verification of the forming condition of energy barriers with model reported in reference; the model in ref. [125] is for triangle structure, a specific case of our model at $\varphi$ =arctan($2h/l_2$).

For the round strucures, model or experimental data for the forming conditions of energy barrier in the noncomposite state are rarely found in the literture. Thus, we experimentally validate our model using aligned electrospun microfibers.These fibers can be treated as the round structures shown in Figure 3.1 (B-1). The details for fabrication and characterization of the fibers can be found in Section 4.2. Figure 3.10 shows the validation with experiment

data. Based on Eq. (3.23), a free energy barrier forms at each round structure if the exterior TPCL is not limited by the geometry constraints. This statement is validated by that three aligned fibers (with a mean radius of 0.9 μm) are able to pin the droplet from spreading and no energy barrier forms at the middle fiber because of the droplet deformation by gravity. Then the APCA is predicted by Eqs. (3.4) and (3.31) at the first advancing energy barrier. Meanwhile, the ECA calculated using Eqs. (3.4) and (3.31) is shown for comparison. The prediction fits with the experimental data with a mean difference of 2.30%.

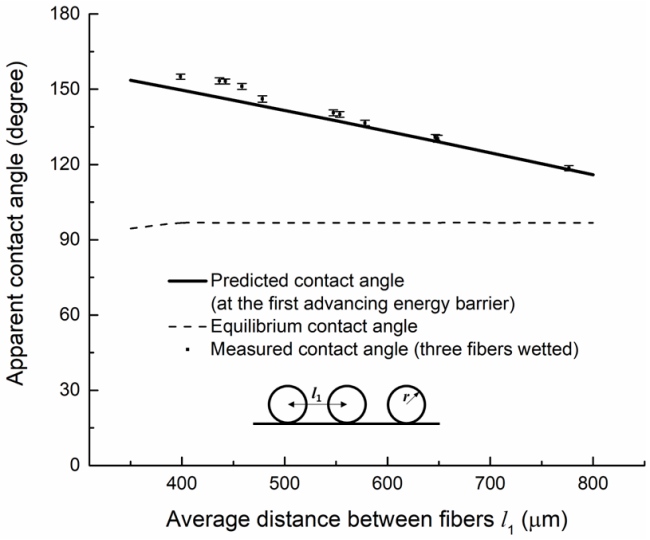


**Figure 3.10.** Validation of the forming condition of energy barrier for round structure using aligned electrospun microfibers ($r = 0.9$ μm).

Figure 3.11 verifies our model for the wetting transition using the model form Vrancken *et al*. [47]. The critical ICAs separating stable composite and noncomposite states for the sharp-edge structures are calculated using Eq. (3.50) and plotted as the dashed lines, which exemplify trapezoid, rectangle, and inverted trapezoid when $\varphi$ increases from 80˚ to 110˚. Here the change of APCA due to droplet penetration into grooves is neglected. As depicted by the inset, the region above or under the critical ICA line indicates that the composite or noncomposite state is thermodynamically stable. The solid line is the modeled critical ICA line for the rectangle structure reported by Vrancken *et al*. [47]; it coincides with our model when $\varphi$ is 90˚. In addition, the square points in the inset are predicted to be in composite

state, which agrees with the observations in the experiment and Lattice Boltzmann Method (LBM) simulation. Then the ICAs of square points are reduced to below critical ICA line, as depicted by the round hollow points, via electrowetting. As a result, wetting transition is observed in experiment and LBM simulation [47].

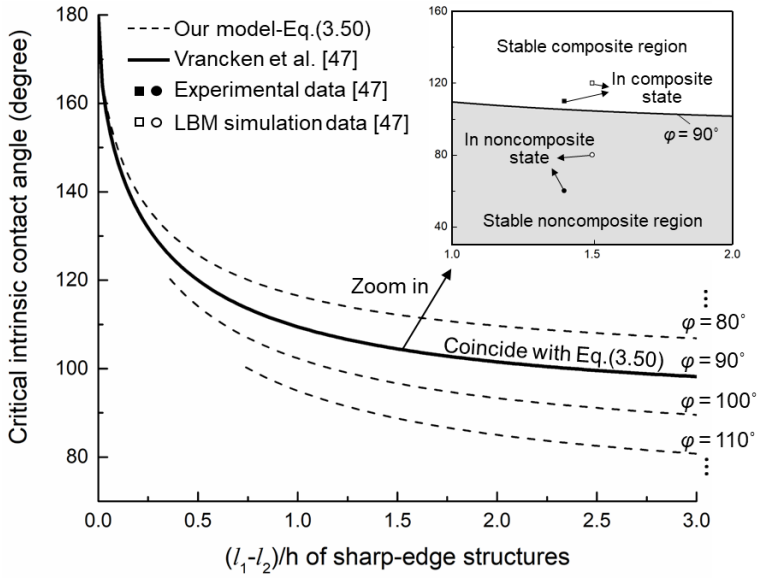


**Figure 3.11.** Validation of the model for evaluating the stability of composite wetting state with the results in reference; the model in ref. [47] is for rectangle structure, a specific case of this paper at $\varphi$ =90˚.

## 3.4 Results and discussion

This section compares the energy barriers of the structures in Figure 3.1 using the validated models with specific structure parameters and ICA. The structures adopted have the same height and spacing, and our focus is on comparing the shapes of structures: $l_1$ = 10 μm, $l_2$ = 4 μm, $h$ = 3 μm, $r$ = 1.5 μm, $\theta_Y$ = 95˚. The internal angle $\varphi$ of the sharp-edge structures varies from 65˚ to 115˚, and the droplet volume is 2 μL.

Figure 3.12 specifies the forming conditions of energy barrier in the noncomposite state following the procedure in Figure 3.6 without considering the geometry constraints. The critical APCAs for energy barrier are calculated using Eqs. (3.22), (3.43) and (3.45) for the sharp-edge structures and Eq. (3.23) for round structures. For the trapezoid with $\varphi$ = 65˚,

energy barrier forms at W3, where the external TPCL locates, when APCA is between $\theta_Y$ and $\theta_Y + \varphi$, and at W2 when APCA is between $\theta_Y - \varphi$ and $\theta_Y$. When $\varphi$ increases to 90˚, the upper limit of APCA for the energy barrier increases to 180˚ because the critical APCA, $\theta_Y + \varphi$ (at W3), exceeds 180˚. As $\varphi$ increases to 115˚ for an inverted trapezoid, the lower limit of APCA decreases to 0˚ since the critical APCA, $\theta_Y - \varphi$ (at W2), is below 0˚.

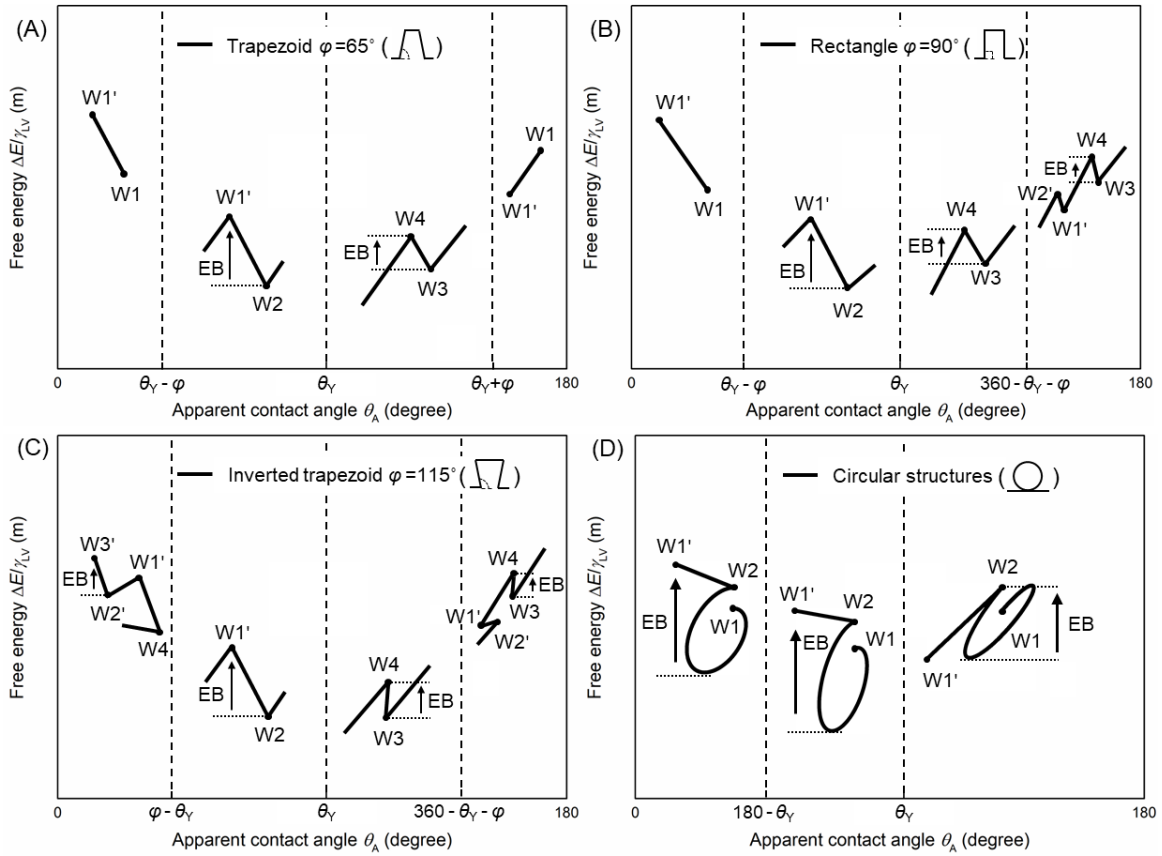


**Figure 3.12.** The forming conditions of energy barrier for (A) trapezoid, (B) rectangle, (C) inverted trapezoid, and (D) the round structures in noncomposite state ($\theta_Y = 95˚$; EB: energy barrier).

For circular structure, the variation of free energy from W1 to W2 is curved because the round surface has continuously varying inclination angle against horizontal plane; energy barrier may form at every structure because a local minimum of free energy at $\theta_o = \theta_A + (180˚ - \theta_Y)$ exists within W1-W2. For the elongated circle, the forming conditions of energy

barrier are the same: the local minima of free energy are at $\theta_o = \theta_A + (180^\circ - \theta_Y)$, which lies in W3-W4 when $\theta_A > \theta_Y$ and W1-W2 when $\theta_A < \theta_Y$.

Figure 3.13 shows the magnitude and forming conditions of energy barrier considering the geometry constraints. For the sharp-edge structures, the APCA ranges for energy barrier are independent on the geometry constraints: $[\theta_Y, 180^\circ]$ for composite state and $[\theta_Y - \varphi, \theta_Y + \varphi]$ for noncomposite state. In composite state, droplet sits on the top surfaces (C1-C2) of structures, so the movement of the external TPCL is not limited by the geometry constraints. In noncomposite state, energy barrier forms at W3 and W2 when APCA is in the range of $[\theta_Y, \theta_Y + \varphi]$ and $[\theta_Y - \varphi, \theta_Y]$, respectively. Even though the exterior TPCL is limited by the geometry constraints, it can still encounter the energy barrier at W3 for large APCA, i.e., around $\theta_Y + \varphi$, as shown in Figure 3.13(B), and at W2 for small APCA, i.e., $\theta_Y - \varphi$. However, the APCA range may be discontinuous as shown in Figure 3.9: for hydrophobic materials, an ICA more than $180^\circ - \varphi/2$ causes a monotonical variation of free energy when APCA is between $[360^\circ - \theta_Y - \varphi, \theta_Y]$ based on Eqs. (3.22), (3.43), (3.45) and Figure 3.6. Similarly, for hydrophilic materials, an ICA below $\varphi/2$ results in a monotonical variation of free energy when APCA lies between $[\theta_Y, \varphi - \theta_Y]$. For round structures, the APCA range decreases to $[10^\circ, 171^\circ]$ for circle and $[17^\circ, 165^\circ]$ for elongated circle. The reduction is due to the short gap distance between adjacent structures, preventing the exterior TPCL from reaching the local minimum at $\theta_o = \theta_A + (180^\circ - \theta_Y)$.

In summary, the round structures extend the range of APCA, especially the lower limit, that forms energy barrier in composite state. This indicates that round structures may cause higher contact angle hysteresis along the direction perpendicular to the surface structure in developing superhydrophobic surfaces. In noncomposite state, the re-entrant structures, i.e., inverted trapezoid and round structures, can increase the APCA range for energy barrier. This result can guide the development of "rose petal" effect for applications such as water harvesting [135] and droplet transportation [136].

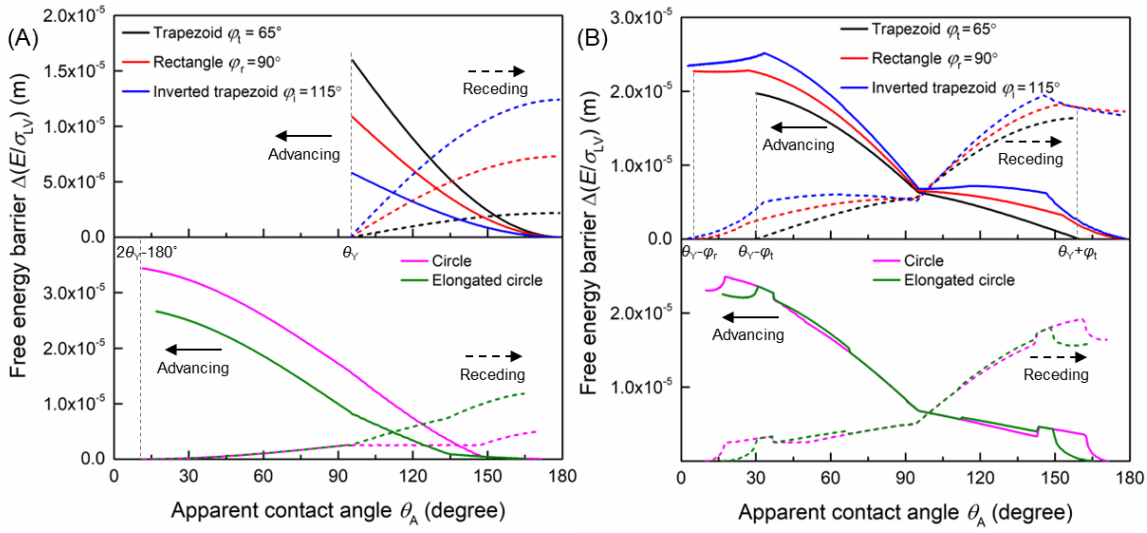


**Figure 3.13.** The magnitudes of energy barrier in the (A) composite and (B) noncomposite states.

In Figure 3.13, both advancing (solid line) and receding (dash line) energy barriers are presented. In composite state, the energy barriers increase toward the moving direction of liquid front because of the monotonically increased $\Delta L_{LV1}$. Based on Eq. (3.2), $L_{LV1}$ and $L_{LV2}$ dominate the change of free energy per unit depth, so the magnitude of energy barrier is mostly influenced by $\Delta L_{LV1}$ since $\Delta L_{LV2}$ is constant. From Eq. (3.26),

$$\Delta L_{LV1} = \frac{d\left(2R_2\theta_A/\sin\theta_A\right)}{dR_2} = 2\cos\theta_A \tag{3.52}$$

Then the variation of $\Delta L_{LV1}$ with $R_2$ is expressed as

$$\frac{d\Delta L_{LV1}}{dR_2} = \frac{d^2\left(2R_2\theta_A/\sin\theta_A\right)}{dR_2^2} = -2\frac{\sin^2\theta_A}{R_2}\frac{\left(\theta_A - \sin\theta_A\cos\theta_A\right)}{\left(\theta_A\cos\theta_A - \sin\theta_A\right)} \tag{3.53}$$

where the right side is proved positive for $\theta_A$ in the range of [0, π], so $\Delta L_{LV1}$ monotonically increases with $R_2$. The trapezoid and circle show relatively greater advancing energy barrier, resulting from the longer distance of C2-C1′ (a local minimum at C2), while their smaller receding energy barriers are derived from the shorter distance of C1-C2. In noncomposite state, the inverted trapezoid shows relatively greater energy barriers in both advancing and receding directions. The round structures have similar energy barriers because of the same

forming conditions of energy barriers. In addition, the cusps in Figure 3.13 (B) result from that the geometry constraints also vary with the APCA.

Figure 3.14(A) presents the variation of free energy per unit depth with the penetration depth in wetting transition given that the APCAs equal to the ECAs in the composite state, which are calculated to be 153˚, 129˚, 113˚, 138˚, and 112˚ for trapezoid, rectangle, inverted trapezoid, circle, and elongated circle, respectively, using Eqs. (3.17)-(3.18). As the internal TPCLs move from T1 to T2, an energy barrier forms for the rectangle, inverted trapezoid, and round structures because free energy increases according to Eq. (3.47). Moreover, the energy barrier for the re-entrant structures, i.e., inverted trapezoid and round structures, is greater because of the increased liquid-vapor interface under the droplet with penetration depth. From T2 to T3, the liquid-vapor interface under the droplet suddenly disappears, causing a reduction of free energy for all structures. Conversely, the wetting transition from noncomposite to composite needs to overcome this energy difference between T2 and T3.

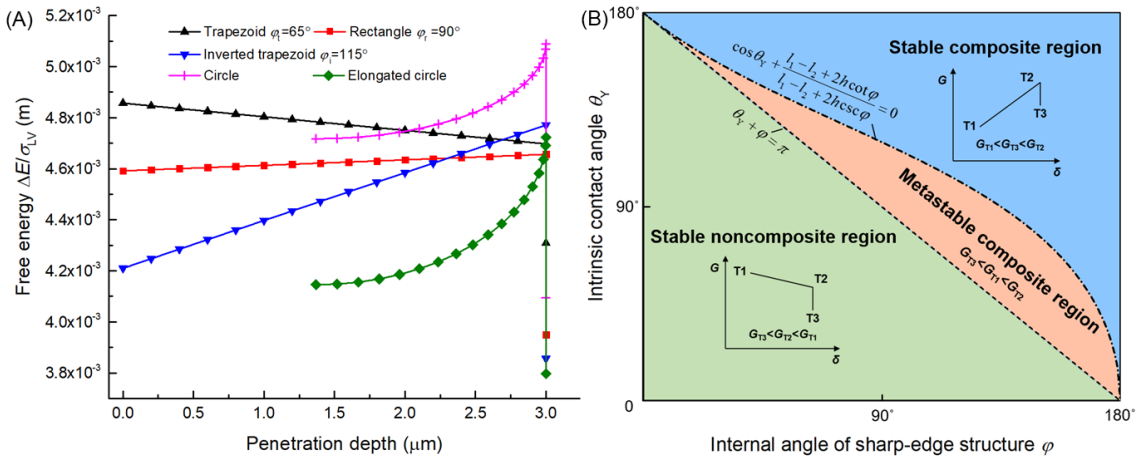


**Figure 3.14.** (A) Variation of free energy per unit depth in wetting transition at the ECAs in the composite state; (B) the stability of wetting states for the sharp-edge structures with varying internal angle and ICA ($l_1 = 10$ μm, $l_2 = 4$ μm, $h = 3$ μm).

Figure 3.14(B) presents the stability of wetting states for the sharp-edge structures. The two critical (dashed) lines are plotted by substituting structure parameters into Eqs. (3.47) and (3.50) by ignoring the change of APCA in wetting transition. Depending on the relative

sizes of free energy per unit depth at T1, T2, and T3, the whole map is divided into stable noncomposite, metastable and stable composite regions. In the stable noncomposite region, free energy decreases from T1 to T3, so noncomposite state is energetically favored. In the metastable composite region, noncomposite state is more stable than composite state but the wetting transition from composite to noncomposite state needs to overcome an energy barrier. In the stable composite region, composite state is thermodynamically more stable. Practically, the area of the stable composite region is discounted because a material with $\theta_Y$ above 120˚ is rarely found [137]. For the round structures, two regions, i.e., metastable and stable composite regions, exist based on Eqs. (3.47) and (3.51) by ignoring the sagging effect. In both regions, an energy barrier forms in transition to noncomposite state for the increased free energy from T1 to T2. In reverse, there is also an energy barrier for transition from noncomposite to composite state due to the increased free energy from T3 to T2.

## 3.5 Summary

This chapter reports an integrated thermodynamic model, which relates system free energy to the continuous movement of three-phase contact lines, for five parallel structures based on geometric transformation. Earlier works [125, 126] reported the initiating and ending conditions of free energy barriers for inclined surfaces. In this work, the forming conditions of energy barriers for the sharp-edge and round structures are derived from the integrated model, and validated with experimental data from our lab and existing model. The specific results and implications are as follows.

(1). For sharp-edge structures with an internal angle $\varphi$ and intrinsic contact angle $\theta_Y$, the initiating and ending APCAs for energy barriers in noncomposite state are $\theta_Y + \varphi$ and $\theta_Y - \varphi$, respectively. Therefore, increasing $\varphi$ can expand the APCA range for forming energy barrier. However, the APCA range may be discontinuous when $\theta_Y$ is smaller than $\varphi/2$ or larger than $180^\circ - \varphi/2$.

(2). For round structures in noncomposite state, an energy barrier may form for every structure at $\theta_A + (180^\circ - \theta_Y)$ because the round surface has continuous inclination angles

with respect to the horizontal plane. However, the geometry constraints can decrease the APCA range for energy barriers to [10˚, 171˚] for the structure parameters of this work. Increasing the gap or reducing the height of the structure can relax the geometry constraints.

(3). In practice, round structures, e.g., aligned electrospun microfibers (with a mean radius of 0.9 μm), are able to pin the droplet at the first advancing energy barrier. Metastable contact angles greater than 150˚ are feasible. Therefore, surfaces patterned with round structures can achieve large contact angle with high contact angle hysteresis. These findings are helpful in developing rose petal effect for applications like microdroplet transportation and water harvesting.

Overall, this work provides insights into the interfacial behavior, especially in metastable state, of wetting rough surfaces. The integrated model can guide the design of structures to control surface wettability. However, the relationship between metastable contact angles and the magnitude of energy barrier is unknown. Therefore, quantifying the influences of energy barrier on metastable contact angle is needed in future work. Moreover, analyzing the energy barriers for hierarchically roughened fibers deserves attention in the future.

# Chapter 4 Developing Superhydrophobic Surfaces with "Rose-Petal" Effect using Aligned Electrospun Fibers

## 4.1 Introduction

Superhydrophobic surfaces with rose-petal effect, also referred to as petal-effect surfaces, show contact angles greater than 150˚ and high droplet adhesion, which can pin the droplets even by turning upside down [8]. The petal-effect surfaces have such potential applications as in droplet transportation [18], lap-on-chip device [19], single molecule spectroscopy [20].

Petal-effect surfaces can be fabricated using chemical etching [138], electroless galvanic deposition [136], plasma reactive ion etching [20], and electrospinning [101]. Among them, electrospinning is a versatile technology to develop sufficient surface roughness for petal-effect surfaces by fabricating micro- and nanofibers. In contrast to subtractive manufacturing, electrospinning has little destruction on the surface to be modified.

Detailed electrospinning-based methods for the fabrication of petal-effect surfaces have been introduced in Section 2.3.3. In brief, petal-effect surfaces are produced by either one-step electrospinning [99-102] or electrospinning followed by post treatments [93, 103]. The high contact angle, i.e., greater than 150˚, is realized by the surface roughness generated by fibers or beads; the high adhesion is achieved by droplets penetrating into inter-fiber spaces, resulting in increased liquid-solid contact interface. However, a fundamental understanding of achieving fiber-based petal effect by controlling fiber morphology is still lacking.

The fiber morphology parameters, including fiber diameter, inter-fiber distance, and fiber orientation, can influence the surface wettability as reported by earlier experimental studies. For example, decreasing poly(caprolactone) (PCL) fiber diameter from 2.2 μm to 0.58 μm increases contact angle from 119˚ to 129˚ [61]; decreasing the inter-fiber distance of nylon-11 nanofibers by increasing the surface coverage rate of fiber from 0.7% to 20% increases contact angle from 70˚ to 124˚ [63]; compared to randomly distributed fibers, directionally

aligned polystyrene (PS) fibers show greater contact angle hysteresis of 57˚ than 34˚ [71].

A few theoretical works have studied the wetting on fibrous surfaces while most of them are focused on the stability Cassie-Baxter (CB) state to guide the design of lotus effect. For instance, Rawal [139] built an analytical model relating fiber parameters with the stability of CB state for randomly distributed fibers; Bucher et al. [140] modeled the critical hydrostatic pressure of the CB state for aligned fibers using numerical simulation. However, as reported by Meng et al. [114], droplets on fibers-dressed surfaces can be pinned by the free energy barriers in the Wenzel state, resulting in a higher contact angle than the ECA. Thus, the CB state may not be necessary in developing petal-effect surfaces.

Therefore, the objective of this research is to strategically approach petal effect based on the understanding of the influence of fiber morphology on the surface wettability. A strategic approach enables to achieve petal effect with less fibers than that by random deposition, so less impact, such as reduction of transparency and air permeability, is caused to the original surfaces. Aligned electrospun fibers are used herein for the simplicity in leveling the contact interface and quantifying fiber parameters. Accordingly, the rest of this chapter is organized as follows. Section 4.2 introduces the experimental methods for fabricating aligned fibers, and characterizing fiber morphology and surface wettability; a theoretical wetting model is built based on the integrated model in Section 3 to help understand the wetting behavior on surfaces dressed by aligned fibers. Then Section 4.4 experimentally studies the influence of fiber parameters on the wettability of surfaces dressed by aligned fibers with explanation of mechanism based on the wetting model; petal-effect surfaces are developed considering the influence of fiber morphology.

## 4.2 Methods

### 4.2.1 Materials

Polystyrene (PS, MW=280 kDa, ICA=95˚ [114]) and N,N-Dimethylformamide (DMF, ACS reagent, ≥99.8%) are purchased from Sigma Aldrich, US. All chemicals are used as received

without any purification. It is worth noting that this thesis selected PS as an example. Other polymers such as PVDF and PMMA may also be used to develop petal effect. Transparent tape, with a water contact angle measured to be 97˚, is supplied from Wisdom Electronics Inc. Deionized water is used for contact angle measurement.

### 4.2.2 Fabrication of aligned fibers

Aligned fibers are fabricated as follows. First, 3.2 g of PS pellets is dissolved in 10 mL of DMF to prepare a 32% (w/v) PS/DMF solution. Then the polymer solution is transferred to a syringe connected to a metallic needle (22 gauge) for electrospinning: the solution feeding rate is 0.8 mL/h; the applied voltage is 13.5 kV; the distance between collector and needle tip is 10 cm. A rotating fin collector, as shown in Figure 4.1, with a rotating speed of 3100 rpm is used to align fibers. The alignment of fibers was driven by the mechanical stretching exerted by the rotating collector and the electrostatic force between the adjacent fins [141]. Transparent tapes are attached to the collector, so aligned fibers are deposited on the tapes in electrospinning. To fabricate fibers with a greater diameter, 36% (w/v) PS/DMF solution and accordingly voltage of 13.0 kV are used. The electrospinning time varies from 1 to 30 seconds to control inter-fiber distances. After electrospinning, fibers are dried in a vacuum oven to remove residual DMF.

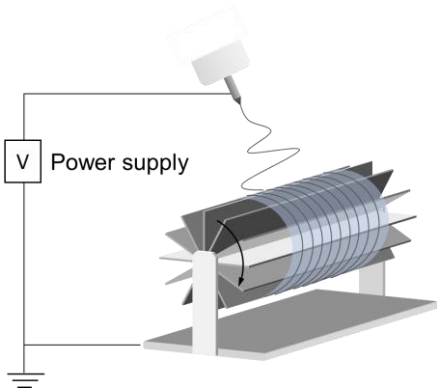


**Figure 4.1.** Schematic of electrospinning with a rotating fin collector

### 4.2.3 Characterization of aligned fibers

The fiber morphology is characterized using a field-emission scanning electron microscope (Zeiss Leo 1530) at 5.0 kV. SEM images at magnifications of 1.0-2.0kX are analyzed by

ImageJ, an image processing software, for fiber diameter. In addition, an optical microscope (Swift SW380B, USA) with a digital in-lens camera is used to capture images of the fibers at low magnifications of 40-1,000X. These images are then analyzed using Swift Imaging 3.0 software to determine the average center-to-center inter-fiber distance.

Then the apparent contact angles of the prepared fiber-dressed surfaces, with varying fiber diameters and inter-fiber distances, are measured using a contact angle goniometer (Ossila Ltd., UK) with sessile drop method: a 2 μL water droplet with standard deviation of 0.04 μL is generated by a 10 μL syringe (minimum graduation of 0.2 μL) with a gauge 32 stainless steel needle; then the 2 μL droplet is gently deposited onto the testing surfaces at a height of 1.5 mm; the measurement process is video recorded and the image for measuring contact angle is captured from the video 5 seconds after the droplet is deposited.

### 4.2.4 Theoretical analysis

A theoretical model is built based on Chapter 3 by treating fibers as circular structure with a smooth surface (or negligible surface roughness), to help understand the wetting behavior on surfaces dressed by aligned fibers. The wetting state of a droplet on a rough surface can be either composite or noncomposite. In this chapter, the droplet is expected to be in the noncomposite state because the inter-fiber distance, *l*, is much larger than the fiber radius, *r*,. Specifically, Figure 4.2 shows the geometry of fiber structure that causes a noncomposite state because of the sagging of underneath liquid-vapor interface onto the substrate. The relationship between *r* and *l* for a specific droplet volume is provided as follows.

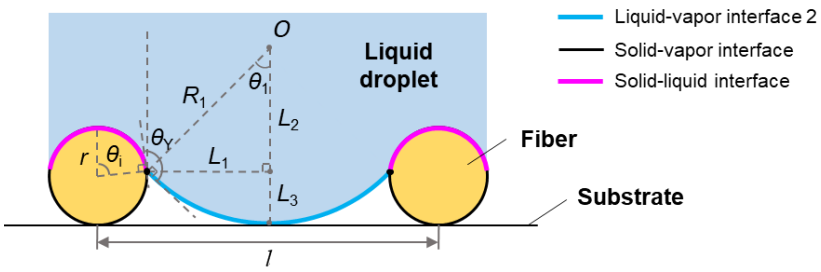


**Figure 4.2.** Fiber structure for a noncomposite wetting state by sagging effect.

To ensure a noncomposite state, the lowest point of the sagged liquid-vapor interface in

Figure 4.2 should have touched the bottom substrate even if there is no external perturbation to the three-phase system. Therefore, the following relationship should hold,

$$L_3 = r + r\cos\theta_i \tag{4.1}$$

where $L_3$ is the sagging depth of liquid-vapor interface, and $\theta_i$ is the angle representing the location of internal three-phase contact line (TPCL) on fiber, as shown in Figure 4.2.

Based on the geometry relationship in Figure 4.2, we can obtain Eqs. (4.2) and (4.3).

$$L_3 = R_1 - \sqrt{R_1^2 - L_1^2} \tag{4.2}$$

$$\theta_i = \pi - \theta_Y + \arcsin\left(L_1/R_1\right) \tag{4.3}$$

where $R_1$ is the radius of the sagged liquid-vapor interface; $\theta_Y$ is the intrinsic contact angle of fiber; $L_1$ is the horizontal distance between the internal TPCL and the lowest point of the sagged interface. Substituting Eqs. (4.2) and (4.3) into (4.1) gives,

$$R_1 - \sqrt{R_1^2 - L_1^2} = r\left(1 + \cos\left(\pi - \theta_Y + \arcsin\left(L_1/R_1\right)\right)\right) \tag{4.4}$$

Solving Eq. (4.4) gives the $L_1$, which can be substituted into Eqs. (4.3) and (4.5) for $l$.

$$L_1 = l/2 - r\sin\theta_2 \tag{4.5}$$

Then the relationship between $r$ and $l$ for noncomposite state is obtained.

Figure 4.3 shows the schematic of a liquid droplet on a surface dressed by aligned fibers in noncomposite state. The fiber can be treated as the circular structure in Figure 3.1(B-1).

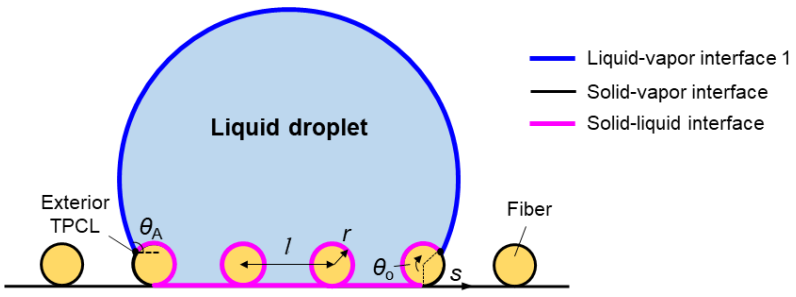


**Figure 4.3.** Schematic of a droplet on a surface dressed by aligned fibers in noncomposite state.

For a surface patterned by fibers with an inter-fiber distance of $l$ and a fiber radius of $r$, Eq. (3.4) can be specified into Eq. (4.6).

$$S = \frac{\left(\theta_A - \sin\theta_A \cos\theta_A\right) R_2^2}{\sin^2\theta_A} + \left(2n-1\right) r\left[l\left(1-\cos\theta_o\right) - r\pi\right] + r^2\left(\pi - \theta_o + \sin\theta_o \cos\theta_o\right) \quad (4.6)$$

where $S$ is the constant [122, 134] cross-section area of droplet; $\theta_A$ is the apparent contact angle (APCA); $R_2$ is half of the basal contact width and can expressed using $n$, $\theta_0$, and $s$, which are used to locate the external TPCL, as follows.

$$R_2 = \left(2n-1\right) l/2 - r\sin\theta_o + s \quad (4.7)$$

Then Eq. (3.8) can be specified into Eq. (4.8).

$$\frac{\Delta E}{\gamma_{LV}} = 2R_2 \frac{\theta_A}{\sin\theta_A} - \left[4(n-1)\pi r + 2r\theta_o\right]\cos\theta_{Y1} - \left[(2n-1)l + 2s\right]\cos\theta_{Y2} \quad (4.8)$$

where $E$ is the free energy of the three-phase system per unit depth; $\gamma_{LV}$ is the liquid-vapor surface tension; $\theta_{Y1}$ and $\theta_{Y2}$ are the intrinsic contact angles of the fibers and the substrate, respectively. Eqs. (4.6-4.8) are the wetting model that relates free energy to the movement of the exterior TPCLs, which relates to APCA, on a surface dressed by aligned fibers.

## 4.3 Results and discussion

Figure 4.4(A-B) present the typical optical microscope images of the produced aligned PS fibers using 32% and 36% (w/v) PS/DMF solution, respectively. Average inter-fiber distance, which is controlled by the electrospinning time as increasing the time decreases the distance, is characterized by dividing the covered width of fibers, normal to the alignment direction, by the number of inter-fiber spaces. Figure 4.4(C-D) show the SEM images for the aligned PS fibers. Each image can only show 2 fibers at maximum because of the sparse distribution. Then Figure 4.4(E-F) provide the fiber diameter distribution by measuring more than 30 fibers for each concentration. As a result, 32% and 36% (w/v) solution generates beadless fibers with diameter of $0.9 \pm 0.1$ μm and $1.8 \pm 0.2$ μm, respectively, which are used to study

the influence of fiber diameter on surface wettability. The solution viscosity increases with polymer concentration, resulting in thicker fibers; further increasing polymer concentration causes quick solidification of solution out of the spinning needle tip.

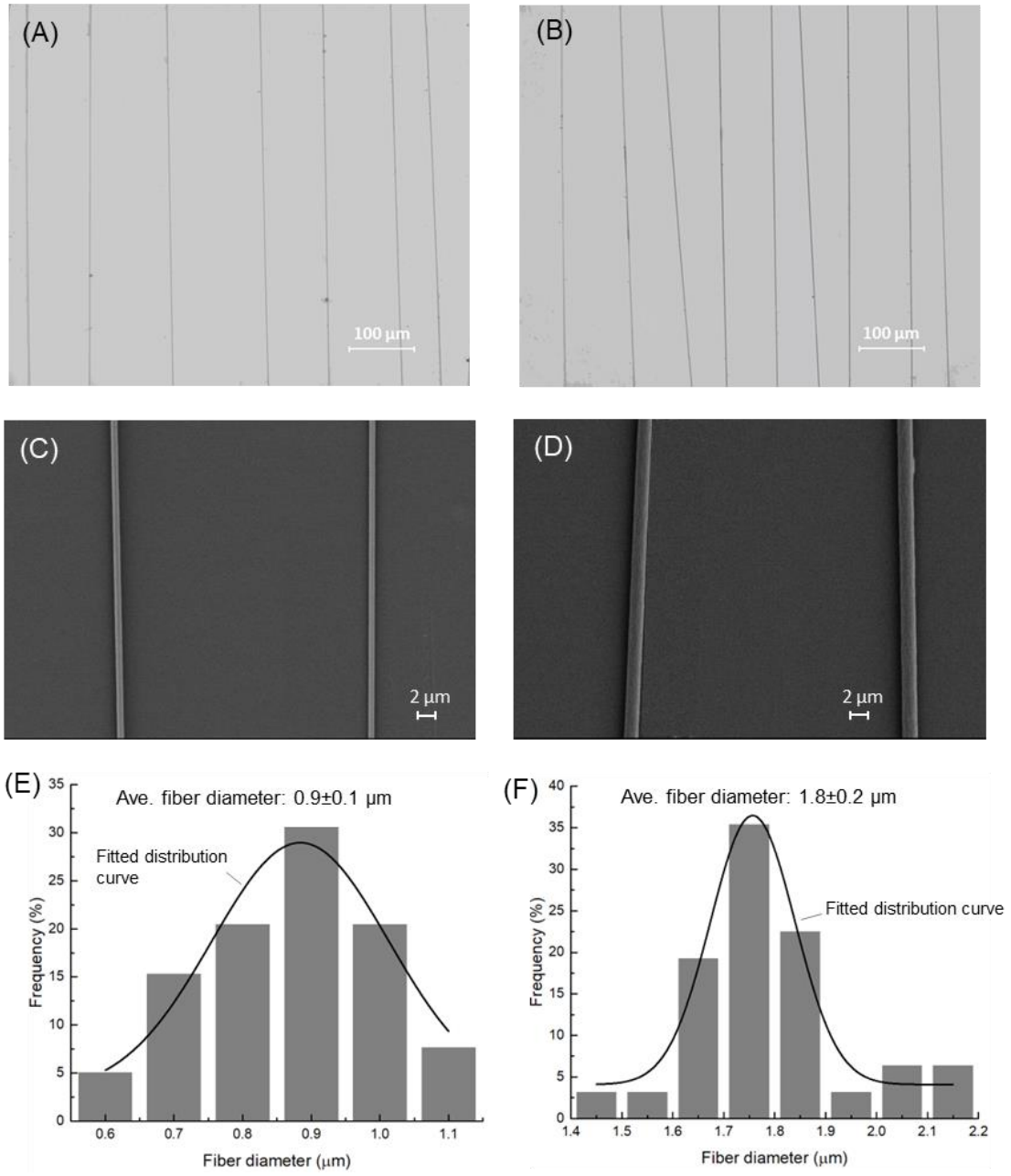


**Figure 4.4.** (A-B) Optical microscope images (40X magnification) of the fabricated aligned PS fibers using (A) 32% and (B) 36% (w/v) PS/DMF solution; (C-D) SEM images (2.0kX magnification) of (C) 32% and (D) 36% (w/v); (E-F) fiber diameter distribution of (E) 32% and (F) 36% (w/v) by measuring more than 30 fibers.

For fibers with diameter of 0.9 μm and 1.8 μm, the inter-fiber distance that ensures a 2 μL droplet, which is used in experiment, in noncomposite state is calculated to be greater than 39 μm and 56 μm, respectively, based on Eqs. (4.4) and (4.5). The inter-fiber distances in the following study are all greater than 70 μm, so droplets are in the noncomposite state.

Figure 4.5 shows the influence of fiber diameter (*d*) on the wettability of surfaces dressed by aligned fibers. We focus on that only two fibers are wetted by the droplet, such that the results are not interfered by the number and distribution of in-between fibers. The triangle and inverted triangle symbols denote the measured APCAs for fibers with *d* of 0.9 μm and 1.8 μm, respectively. The black dashed line shows the theoretical equilibrium contact angle (ECA), predicted using Eqs. (4.6-4.8) by locating the global minimum of free energy. The experimental APCAs deviate from the theoretical ECAs in Figure 4.5, indicating that the droplets should be pinned at metastable states.

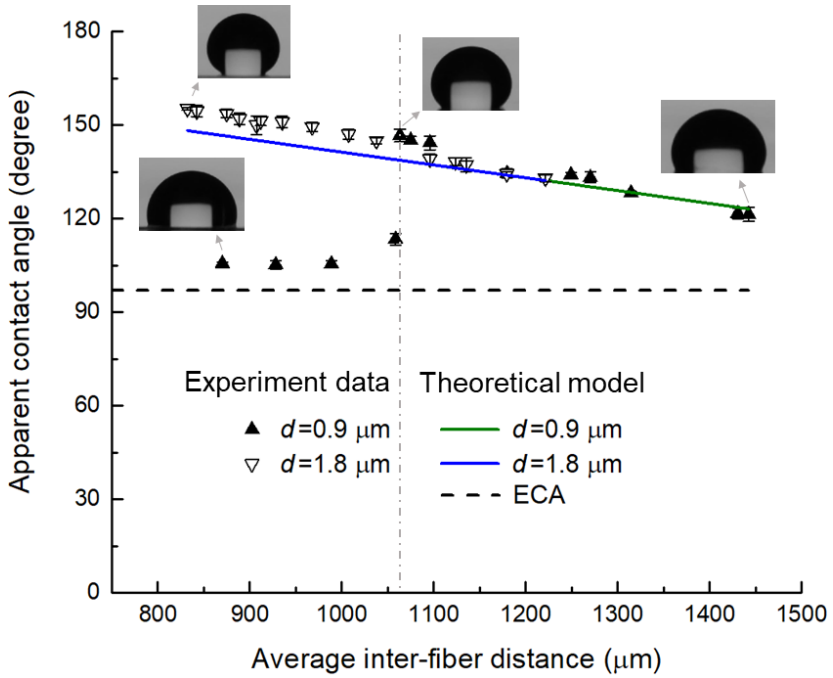


**Figure 4.5.** Influence of fiber diameter on the wettability of surfaces dressed by aligned fibers (average fiber diameter: 0.9 μm and 1.8 μm; droplet volume: 2.0 μL)

To explain the metastable state in Figure 4.5, Figure 4.6 shows the variation of free energy per unit depth with APCA by substituting fiber parameters of *d*=1.8 μm, *l*=1060 μm (as an

example to explain the metastable state), droplet volume of 2 μL, $\theta_{Y1}$=95˚, $\theta_{Y2}$=97˚ into Eqs. (4.6-4.8). The ECA corresponds to the APCA where the global minimum of free energy is located. As indicated by the inset of Figure 4.6, an energy barrier, which can hinder the three-phase system from reaching the global minimum of free energy, is formed at the location where fibers are located. As a result, the droplet is pinned at the local minimum of free energy.

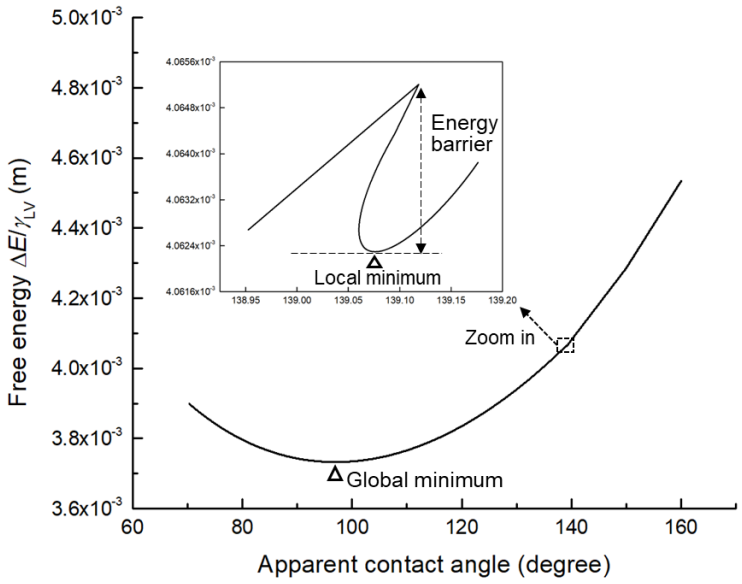


**Figure 4.6.** Variation of free energy per unit depth with APCA and illustration of energy barrier ($d$ = 1.8 μm; $l_1$=1060 μm; droplet volume: 2 μL; $\theta_{Y1}$=95˚; $\theta_{Y2}$=97˚).

Based on Figure 4.6, the predicted contact angles for the experimental fiber parameters are calculated using Eqs. (4.6-4.8) at the first energy barrier, since only two fibers wetted, and plotted as the solid lines in Figure 4.5. The prediction fits with the experimental data with a mean difference of 2.9%. Then the influence of $d$ is discussed as follows.

In Figure 4.5, when $l$ is above 1060 μm, the APCAs for both fiber diameters increase with decreasing $l$ if only the energy barrier can pin the droplet from further spreading. The same increasing pattern for both fiber diameters is attributed to that the $d$ is much smaller than the scale of droplet (< 2 μm vs ~1600 μm), thus APCA is dominated by the basal width of droplet according to Eq. (4.6). However, the APCA of 0.9 μm fibers falls to 113˚ and then 105˚ when $l$ is below 1060 μm because the droplet overcomes the energy barrier and cross

the two fibers. In contrast, the APCA of 1.8 μm fibers keeps increasing to 155˚ until $l$ =830 μm. The difference of the maximum APCAs between the two fibers indicates the difference of magnitude of energy barrier.

Figure 4.7 shows the variation of magnitude of free energy barrier with the basal width of droplet ($2R_2$) for different fiber diameters. The magnitude of energy barrier is calculated by subtracting the free energy at one metastable state from the following peak of free energy, as explained in the inset of Figure 4.6. The basal width of droplet, equals to the $l$ when only two fibers are wetted. As indicated in Figure 4.7, the magnitude of energy barrier increases with the basal width and $d$. Specifically, the increment with basal width is essentially due to the increased $\Delta L_{LV1}$ as explained in Section 3.4. For the increment with $d$, the local minimum of free energy locates at the same angular position of fiber for different $d$ based on Eq. (3.23), but fiber with larger diameter has a greater arc length along the spreading of droplets. Thus, the larger maximum APCA for 1.8 μm fiber in Figure 4.5 results from the higher magnitude of energy barrier.

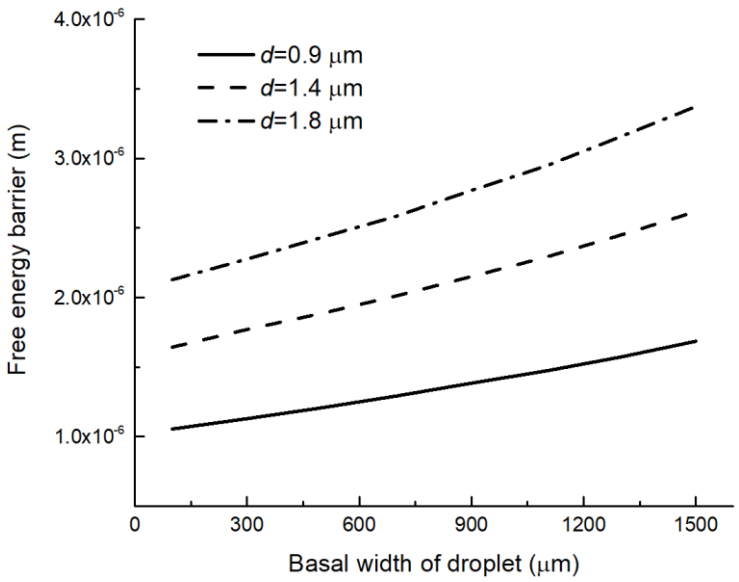


**Figure 4.7.** Variation of magnitude of free energy barrier with the basal width of droplet for different fiber diameters (droplet volume: 2 μL; $\theta_{Y1}$=95˚; $\theta_{Y2}$=97˚).

Figure 4.8 presents the influence of average inter-fiber distance ($l$) on the wettability of surfaces dressed by aligned fibers with an average fiber diameter of 1.8 μm. Specifically, as $l$ decreases from 1000 μm to 210 μm, the number of fibers being wetted increases from 2 to 5. The triangle, inverted triangle, square, and round points denote the measured APCAs for wetting 2, 3, 4, and 5 fibers, respectively.

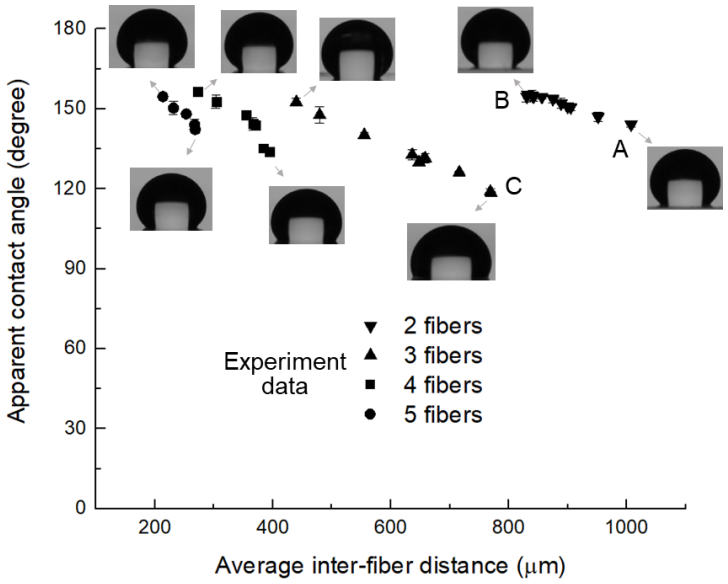


**Figure 4.8.** Influence of inter-fiber distance on surface wettability (average fiber diameter: 1.8 μm; droplet volume: 2.0 μL).

Pinning a droplet at a metastable state indicates that the perturbation energy to the droplet is not able to overcome the free energy barrier. At the point A of Figure 4.8, where two fibers are wetted and the $l$ is about 1000 μm, the energy barrier induced by the two fibers is greater than the perturbation energy, so the APCA of point A can be realized. As we decrease $l$, the magnitude of energy barrier decreases (*see* Figure 4.7) while the perturbation energy remains nearly constant for a given measurement environment. At point B ($l$~800 μm), the energy barrier is very close to (or slightly greater than) the perturbation energy. Further decreasing $l$ results in that the droplet overcomes the energy barrier and wets more fiber, i.e., jumping from point B to C. From B to C, the basal width of droplet increases from $l$ to 2$l$, resulting a higher energy barrier, but the APCA at point C drops below 120˚.

In Figure 4.8, similar variation pattern of APCA as the change from A to B to C can be observed for wetting three to five fibers. However, the overall APCAs for three to five fibers increase when $l$ is below 800 μm. The reason is attributed to the decreased $l$ from three to five fibers: once the energy barrier pinning the droplet is overcome, the following fiber that can pin the droplet becomes closer. In other words, more energy barriers are induced by the denser fibers to attenuate the perturbation energy to the droplet. In addition, the maximum APCAs for wetting three to five fibers are nearly fixed around 155˚ because of the nearly constant perturbation energy to droplets. At the maximum APCA, the perturbation energy is very close the energy barrier, which is only determined by the basal width of droplets for a given fiber diameter (*see* Figure 4.7). Thus, the basal width is similar due to the constant perturbation energy, resulting in a nearly fixed maximum APCA.

Based on the results in Figure 4.5 and Figure 4.8, it can be concluded that, in noncomposite state, increasing fiber diameter and reducing inter-fiber distance can increase the APCA of surfaces dressed by aligned fibers. These findings can guide the development of petal-effect surfaces in the next. However, the fiber diameter here is hard to be further increased because ensuring fiber alignment needs a high rotating speed of the electrospinning collector, which reduces fiber diameter because of the extra stretching of fibers on collector. Therefore, we reduce the inter-fiber distance for petal effect.

Figure 4.9(A) shows the APCA of fibers ($d$ = 1.8 μm) with inter-fiber distance $l$ varying from 70 to 1000 μm. When $l$ lies between 160-1000 μm (solid inverted triangles), less than eight fibers are wetted and the APCA varies in the range of 118˚-156˚. As $l$ decreases below 130 μm (solid triangles), eight or more fibers are wetted, resulting in an APCA range of 150˚-156˚. The stable APCA for $l$ < 130 μm is attributed to the multiple free energy barriers induced before the pinning location. Moreover, the same highest APCA of 156˚ for $l$ varying in 160-1000 μm and 70-130 μm is determined by the environment perturbation.

Furthermore, the adhesion of fiber-dressed surfaces ($d$ = 1.8 μm and $l$ <130 μm) to water droplet is characterized by tilting the surfaces after deposition of water droplets. As a result,

droplets can adhere to all the surfaces by turning the surfaces upside down. Figure 4.9(B) shows that the high adhesion enables to turn the fiber-dressed surface with a droplet having a contact angle of 156˚ upside down. After turning back, the basal width and the APCA of the droplet remain unchanged. The high adhesion is attributed to liquid droplet penetrating into the spaces between adjacent fibers, resulting in a high liquid-solid contact area.

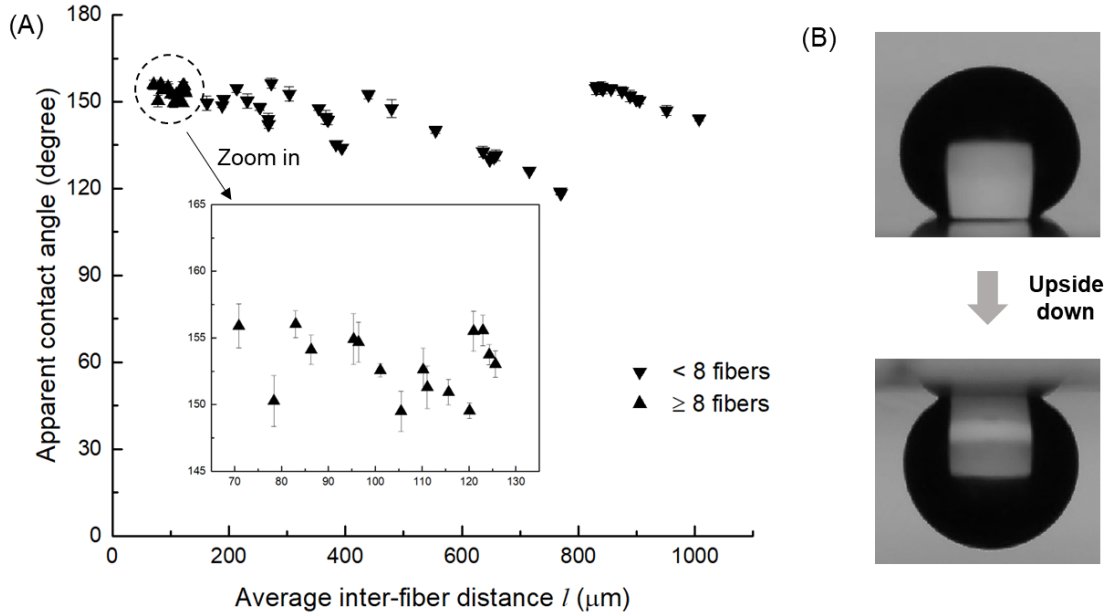


**Figure 4.9.** (A) The apparent contact angle of fiber-dressed surfaces with inter-fiber distance varying from 70 μm to 1000 μm (average fiber diameter: 1.8 μm; droplet volume: 2.0 μL); (B) Illustration of rose petal effect by turning the surface with a droplet upside down.

## 4.4 Summary

This research studied the influence of fiber parameters on the wettability of surfaces dressed by aligned fibers and developed petal-effect surfaces with a strategic approach. Based on this research, the following conclusions can be reached.

(1). A thermodynamic model relating free energy with the apparent contact angle (APCA) on the surfaces dressed by aligned fibers is built. Free energy barriers can pin a droplet at metastable states, resulting in higher APCAs than the equilibrium contact angle. The model indicates that the magnitude of energy barrier increases with the fiber diameter

and basal width of droplets.

(2). Aligned polystyrene fibers with diameter of 0.9 μm and 1.8 μm and varying inter-fiber distance from 80 μm to 1450 μm are produced using one-step electrospinning. At large inter-fiber distance, > 800 μm, where two fibers can pin a 2 μL droplet from spreading to equilibrium state, the maximum APCA of the 1.8 μm fibers is 155˚, compared to that of 147˚ for 0.9 μm fibers. The greater APCA is due to the higher magnitude of energy barrier for 1.8 μm fibers.

(3). When the inter-fiber distance is below 800 μm, two 1.8 μm fibers are unable to pin the droplet because of the reduced energy barrier with inter-fiber distance, so three fibers are wetted with APCA reducing below 120˚. Similar variation of APCA by reducing inter-fiber distance are observed for three to five fibers. However, the overall APCAs increase because more energy barriers are induced to attenuate the perturbation.

(4). Superhydrophobic surfaces with rose-petal effect are created using aligned fibers with a diameter of 1.8 μm and inter-fiber distance between 70 μm and 130 μm. The APCAs of the fiber-dressed surfaces are in a range of 150˚-156˚, and droplets can adhere to the surfaces by turning the surfaces upside down. The basal width and the APCA of the droplet are unchanged after turning back.

However, it should be noted that the fabrication of the petal effect surfaces using aligned fibers is still in a laboratory scale. The rotating fin collector and the single spinneret used in this thesis can result in a low production rate, which is hard to satisfy industrial demand.

# Chapter 5 Developing Superhydrophobic Surfaces with "Lotus" Effect using Aligned Porous Fibers*

## 5.1 Introduction

Superhydrophobic surfaces with lotus effect, also termed as lotus-effect surfaces [142, 143], are featured with a high water contact angle (> 150˚) and a low roll-off angle (< 10˚) [144]. The lotus-effect surfaces have a variety of applications in developing functional materials including self-cleaning [108], anti-corrosion [15], anti-icing [16].

Surface roughness is necessary for developing a lotus-effect surface since a material with intrinsic contact angle greater than 120˚ is rarely available [137]. For the wetting on a rough surface, droplets can be in Wenzel [42] or Cassie-Baxter (CB) [41] state. Compared to the Wenzel state, droplets in the CB state have less contact area with solids, resulting in lower adhesion to the surfaces and thereby a lower roll-off angle. Therefore, CB state is preferable for creating lotus-effect surfaces.

Lotus-effect surfaces can be fabricated by a few techniques including lithography [21], chemical etching [22], laser micromachining [24], and electrospinning [25]. Electrospinning is a facile and versatile technique to generate continuous micro- and nano-fibers by applying a high voltage on a viscous polymeric solution. The generated thin fibers can increase surface roughness, enabling electrospinning to be an efficient method for developing lotus-effect surfaces. In addition, different from methods such as chemical etching, laser micromachining that need to subtract materials from surface, electrospinning modifies surface wettability by introducing new materials, resulting in less impact on the original surface.

A few electrospinning-based methods are developed for producing lotus-effect surfaces, which have been introduced in Section 2.3.1 and 2.3.2 of this thesis. Briefly, these methods

* The contents have been accepted for publication in *Advanced Materials Interfaces*.

are classified into one-step electrospinning and electrospinning followed by post treatments. However, current electrospinning-based methods for developing superhydrophobicity often require complex fabrication processes and multiple raw materials, which increase the overall cost and hinder them from broad implementation. For example, synthesizing and applying low surface energy polymers into the electrospinning solution [31, 97], adding nanosized additives to the fiber surface [28, 87], and various post-treatments to incorporate a secondary material, such as PPFEMA [33, 61], DMDCS [91], and DTMS [29], with desired surface energy are commonly reported in the literature.

Moreover, there is a lack of a strategic approach to superhydrophobicity by electrospun fibers. Current theoretical works have limited ability in guiding the development of super-hydrophobic electrospun structures because either the works are limited to only studying the stability of wetting state or the theoretical structures are difficult in replicating because of oversimplification of the fibrous structures in developing model. For example, Rawal [139] developed an analytical model relating fiber parameters with the pressure difference across the liquid-vapor interface. Based on the model, the influence of fiber diameter and inter-fiber distance on the CB stability is analyzed. Moreover, Emami et al. [145] treated fibrous surface as a plane by neglecting the height difference of fibers in different layers to explore the influence of fiber orientation on the CB stability. In addition, Onda [146] built a model for the equilibrium contact angle (ECA) of fibrous surfaces. Fibrous structure is treated as a porous film, so the ECA is related to volume porosity, film thickness, etc.

Therefore, the objective of this study is to develop a superhydrophobic electrospun fibrous structure by a strategic approach based on the understanding of droplets wetting behavior on fibrous structures. Uniaxially and biaxially aligned porous polystyrene (PS) fibers are studied because such structure may assist in achieving the lotus effect, due to (1) the porous fiber surface reduces the contact area between fibers and droplets (since the nanopores on the fiber surface can resist liquid from penetration due to the intrinsic hydrophobicity of PS and the closed pore [147]), facilitating the movement of droplet by reducing the resistance;

(2) the alignment serves as a track to facilitate droplet rolling at a low tilting angle.

Accordingly. the rest of this chapter is organized as follows. Section 5.2 introduces the experimental methods for fabrication of uniaxially and biaxially aligned porous fibers, and characterizations of fiber morphology and hydrophobicity. Section 5.3 builds a numerical model using Surface Evolver to determine the wetting state of droplets on the fiber-dressed surfaces. Section 5.4.1 provides the morphology of the fabricated fibers. The experimental wetting behaviors on the uniaxially and biaxially aligned porous fibers, presented in Section 5.4.2, are explained in Section 5.4.3 based on the numerical simulation. Then Section 5.4.4 develops a lotus-effect surface by a strategic approach considering the influences of fiber-surface pores and liquid-fiber contact area. Finally, Section 5.5 summarizes this chapter.

## 5.2 Experimental methods

### 5.2.1 Fabrication of aligned porous fibers

Aligned porous fibers are produced by electrospinning as follows. First, a polymer solution is prepared by dissolving 1.9 g of polystyrene (PS, obtained from Sigma-Aldrich, US, with a molecular weight of 280 kDa and an intrinsic water contact angle of 95˚) into 10 mL of tetrahydrofuran (THF, obtained from Sigma-Aldrich, US, ACS reagent grade ≥ 99%). The THF has a low boiling point at 66℃, such that its quick evaporation in electrospinning can help to create pores on fiber surfaces by breath figure [68]. Then, the PS solution is loaded into a syringe with a 22 gauge metallic needle for electrospinning with the solution feeding rate of 4.4 ml/h, the applied voltage of 6 kV, and the needle tip to collector distance of 10 cm. A rotating fin collector covered with transparent tape is used to collect the uniaxially aligned fibers. The collector rotates at a speed of 450-1,000 r/min and the deposition time is between 30-270 s. The transparent tape has an intrinsic contact angle of 95˚. The relative humidity (RH) of the air inside the electrospinning chamber is controlled between 40% and 80% by a portable humidifier (Sparoom, US) to create pores on fiber surfaces. Finally, the biaxial structures are produced by rotating the tape 90˚ for depositing the upper-layer fibers.

### 5.2.2 Characterization of fiber morphology

The morphology of the prepared electrospun fibers is characterized using a field-emission scanning electron microscope (SEM, Zeiss Leo 1530, Germany) at 5.0 kV. SEM images at low magnification of 500X and high magnifications of 10-20kX are analyzed by ImageJ software to measure fiber diameter, and pore size and pore area fraction, respectively, of the produced fibers. In addition, an optical microscope with a digital in-lens camera (Swift SW380B, USA) is used to capture images of the produced fibers at low magnifications of 40-1,000X. These images are then analyzed using Swift Imaging 3.0 software to determine the average center-to-center inter-fiber distance.

### 5.2.3 Characterization of surface wettability

The contact angle ($\theta_A$) and roll-off angles ($\alpha_r$) of the fiber-dressed surfaces are measured using a contact angle goniometer (Model 250, ramé-hart instrument, US) with the sessile drop method. Deionized water droplets with a volume of 3 μL, unless otherwise specified, are generated by an automated dispensing system of the goniometer and mounted on the testing surfaces. The contact angles along the fiber direction are measured from the images captured by the ramé-hart DROPimage Advanced software. After that, the roll-off angle is determined by tilting the sample platform of the goniometer in the direction that droplets roll along the fiber direction. The contact angle and roll-off angle of each tested surface are measured 3-5 times, and average values are presented with standard deviation.

## 5.3 Model development

The model developed in this study determines the wetting state of water droplets on a fiber-dressed surfaces since the wetting behaviors of the droplet are closely related to the wetting state. A droplet can either fully or partially penetrate into the inter-fiber spaces, resulting in different contact angle and roll-off angle. Specifically, full penetration refers to the droplet touching the underneath substrate and filling all the inter-fiber spaces, i.e., in Wenzel state. Partial penetration means that the penetrated droplet stops at a certain layer of fibers and

creates an air pocket between the bottom of the droplet and the underneath substrate. If the droplet stops at the top-layer fibers, it is noted as the Cassie-Baxter (CB) state.

The wetting state of a droplet on the fiber-dressed surface is controlled by its free energy *G*. The penetration of a liquid into the inter-fiber spaces may stop at a state where *G* is locally or globally minimized. The calculation of *G* is expressed as Eq. (5.1) [148].

$$\frac{G}{\gamma_{LV}} = A_{LV} - \iint_{A_{LF}} \cos\theta_{Y,F} dA - \iint_{A_{LS}} \cos\theta_{Y,S} dA \tag{5.1}$$

where $A$ and $\gamma$ are the surface area and surface tension, respectively; subscripts L, V, and F denote to liquid, vapor, and fiber, respectively; $\theta_{Y,F}$ and $\theta_{Y,S}$ are the intrinsic contact angles of the porous fiber and the substrate materials, respectively. The effect of gravity on droplet deformation is ignored since the radius of a 3 μL droplet (~0.89 mm) used in this study is smaller than the capillary length of ~2.7 mm [149].

Therefore, the free energy of the system, *G*, is essentially related to $A_{LV}$, $A_{LF}$, and $A_{LS}$ as shown in Eq. (5.1). The latter three are variables changing with the droplet penetration and spreading on a fibrous structure. It brings challenges to analytically solve Eq. (5.1) because the liquid-vapor and liquid-fiber interfaces deform to complex geometries when the droplet is in contact with fibers (especially for multi-layer fibers). Thus, this study employs Surface Evolver (SE, version 2.70) finite element code to numerically solve Eq. (5.1) and predict the wetting state by minimizing the total free energy of the surface.

Figure 5.1 presents the schematic of the initial configuration of a water droplet on either uniaxially or biaxially aligned porous fibers for modeling in Surface Evolver. The droplet shape is initially set as cubic prior to minimizing total surface energy. The number of fibers in contact with the droplet is subject to the droplet volume. For a 3 μL droplet, the number of fibers contacted is between 4-30 based on the inter-fiber distance. It should be noted that only two fibers are shown in Figure 5.1 to help visualize the contact between droplet and fibers. Grid independence is checked by ensuring the variation of *G* is less than 0.01% after each successive refinement. For the biaxially aligned fibrous structure, the lower-layer fibers

are set to have one fiber (or two for studying the inter-fiber distance of the lower layer). This configuration is deemed adequate for studying the trend of free energy changes during the droplet wetting, and it can also save computational costs by avoiding complicated mesh. In addition, the length and energy related parameters in the model are normalized to their dimensionless forms with respect to $d_c$, and $\gamma_{LV} d_c^2$ [150, 151], respectively. The $d_c$ is set as 5 μm to represents the characteristic diameter of the produced fibers.

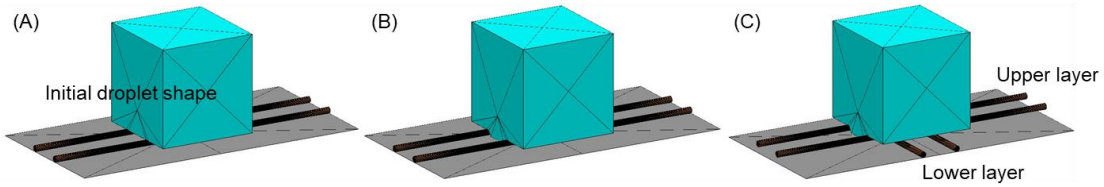


**Figure 5.1.** Initial configuration of a water droplet contacting (A) only fibers and (B) both fibers and substrate of uniaxially aligned porous fibers, and (C) the upper- and lower-layer fibers of biaxially aligned porous fibers for modeling using Surface Evolver.

The effect of porous fibers on droplet wetting is approximately considered equivalent to that of using smooth fibers with an elevated $\theta_Y$ in the modeling since the SE is incapable of adding pores to fibers. In detail, the amendment of $\theta_{Y,F}$ is based on a strategy of formulating a non-porous surface that has the same energy change as the droplet does on a porous surface. For a droplet wetting a porous surface, the change of free energy $\Delta G$ is expressed as [148]

$$\frac{\Delta G}{\gamma_{LV}} = \Delta A_1 + (1 - f)\Delta A_2 - f\Delta A_2 \cos\theta_{Y,F} \tag{5.2}$$

where $\gamma_{LV}$ is the interfacial tension between water and vapor phase; $A_1$ and $A_2$ are the surface areas of the outer surface of the droplet and the apparent contact area between the droplet and the substrate, respectively; $f$ is the fraction of the actual surface wetted area over $A_2$; a porous surface with a higher porosity means a smaller $f$. In contrast, the energy change of a droplet wetting a non-porous surface is expressed as

$$\frac{\Delta G}{\gamma_{LV}} = \Delta A_1 - \Delta A_2 \cos\theta_{Y,F} \tag{5.3}$$

where $\theta_{Y,F'}$ is the intrinsic contact angle of the non-porous surface. Then, Eqs. 5.2 and 5.3 give Eq. 5.4 when $\Delta G$ on the porous and non-porous surfaces are the same.

$$\theta_{Y,F} = \arccos\left( f \cos\theta_{Y,F'} - 1 + f \right) \tag{5.4}$$

## 5.4 Results and discussion

### 5.4.1 Electrospun fiber morphology

Figure 5.2(A-D) show the surface morphology of the electrospun fibers produced at different RH. The results demonstrate the porous nature of fibers. The largest pore size of $180 \pm 49$ nm is obtained for electrospinning at the highest RH of 80%. As the RH reduces to 60%, 50%, and 40%, the pore size reduces to $160 \pm 31$ nm, 93±22 nm, and 77±16 nm, respectively. Furthermore, the fraction of the fiber surface occupied by pores ($f_p$) is related to the size of the pores. Thus, $f_p$ also decreases from 51% to 34% with reducing RH for electrospinning. Additionally, it is also worth noting that increasing the speed of collector to more than 1000 rpm can alter the pore shape from approximate circle to oval because of the extra stretching to the fibers by the collector.

The formation of pores on fiber surfaces at a high RH fabrication environment of 40-80% is explained as follows [68, 152]. In electrospinning, the THF solvent in the ejected fibers evaporates to solidify the PS solute and form elongated fibers under an electric field. At the same time, the evaporation of THF is quick enough (due to its relatively low boiling point of 66°C) to considerably reduce the fiber temperature, leading to the condensation of water vapor into droplets from the ambient air. Eventually, these condensed droplets result in the formation of the surface pores, because they occupy spaces before the ejected fiber is fully solidified (PS is hydrophobic and not soluble in water). This also explains the observation of bigger pore size and greater $f_p$ for fibers fabricated at higher humidity, as it facilitates the condensation of water vapor onto the fiber surface during electrospinning. It is worth noting that the vapor-induced phase separation is not accounted for the pore formation because the compositional path of the PS solution stays in the homogeneous region in the ternary phase

diagram of $H_2O$/THF/PS [152].

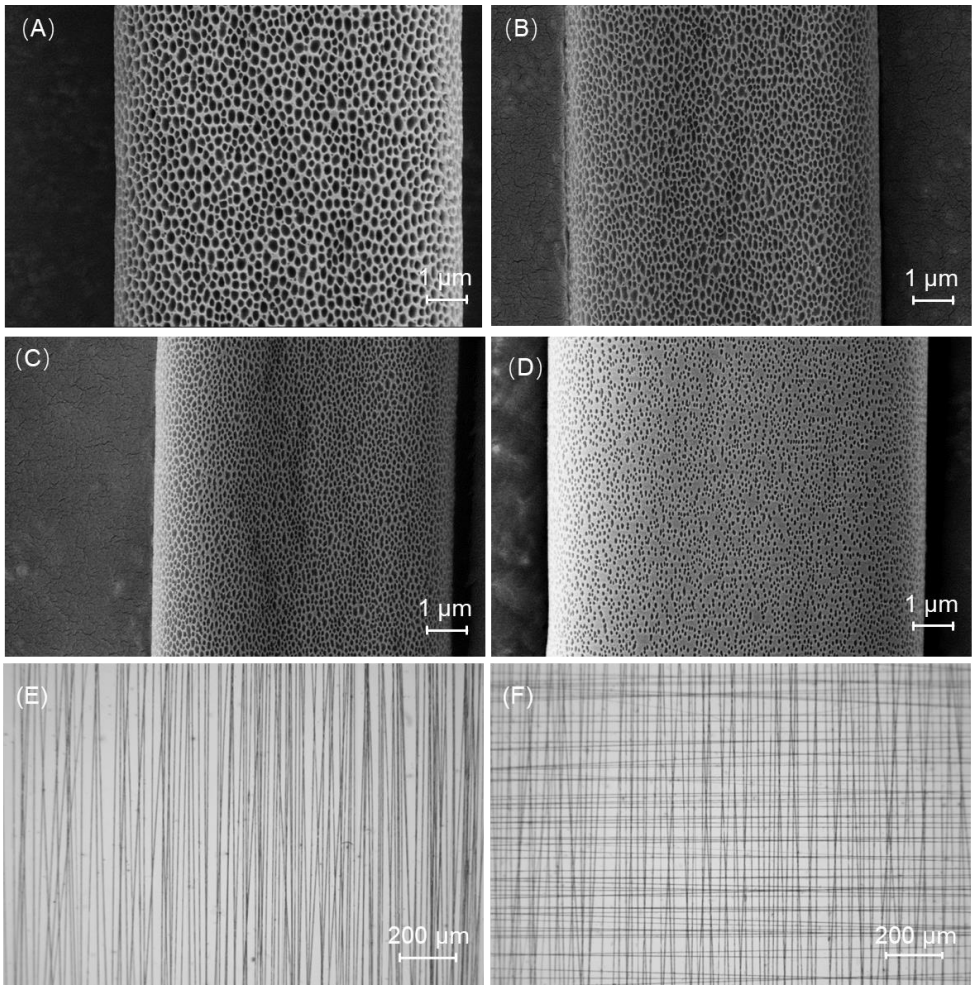


**Figure 5.2.** SEM images of the aligned porous fibers electrospun at (A) 80%, (B) 60%, (C) 50%, and (D) 40% relative humidity, and optical microscope images of 40X magnification for surface dressed by (E) uniaxially and (F) biaxially aligned porous fiber.

Figure 5.2(E-F) present the optical microscope images of the surfaces dressed by porous fibers, which shows that the fibers are directionally aligned. The average inter-fiber distance is obtained by dividing the covered width of fibers, normal to the alignment direction, by the number of inter-fiber spaces. In this study, the inter-fiber distance, ranging from 10 to 90 μm, is controlled by the electrospinning time as increasing the time decreases the distance.

### 5.4.2 Wetting behavior of surface dressed by aligned porous fibers

Figure 5.3 shows the preliminary experimental results for comparing the hydrophobicity of porous and non-porous fibers. The contact angle $\theta_A$ and roll-off angle $\alpha_r$ are measured on

substrate surfaces (i.e., glossy side of an adhesive tape) dressed by uniaxially aligned fibers. The fiber diameters and inter-fiber distances of all samples are in the range of 6.2-8.9 μm and 25.3-29.5 μm, respectively. Maintaining these two parameters within a relatively narrow range is advantageous in highlighting the influence of pores on hydrophobicity.

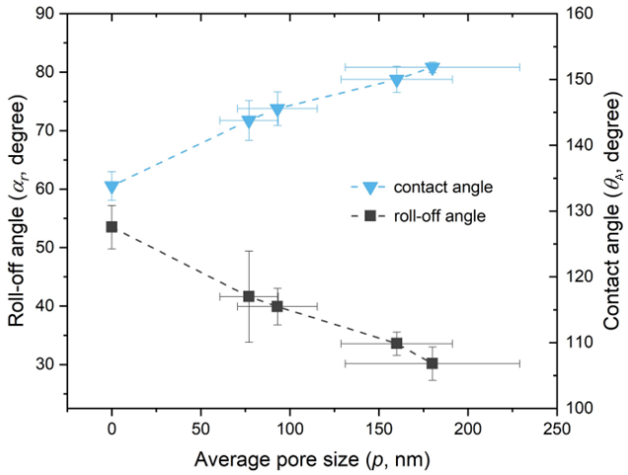


**Figure 5.3.** Comparison of hydrophobicity of surfaces dressed by uniaxially aligned fibers with and without pores

The results in Figure 5.3 show the advantage of porous fibers in improving hydrophobicity. Increasing the average pore size from 0 to $180 \pm 49.0$ nm (corresponding to increasing the fraction of the fiber-surface area occupied by pores from 0 to 34-51%), leads to increasing contact angle from $134 \pm 2^{\circ}$ to $152 \pm 1^{\circ}$ and decreasing roll-off angle from $54 \pm 4^{\circ}$ to $30 \pm 3^{\circ}$. This improvement in hydrophobicity is attributed to the increase of the total liquid-vapor contact area when the droplet contacts fibers with greater pore area. Then, the observed $\theta_A$ increase can be explained by the CB equation [41]:

$$\cos\theta_A = f_1 \cos\theta_Y - f_2 \tag{5.5}$$

where $f_1$ and $f_2$ represent the area fractions of the liquid-solid and liquid-vapor interfaces, respectively, over the unity parallel plane area of a rough surface. $\theta_Y$ is the intrinsic contact angle of the solid material. In this study, the sum of $f_1$ and $f_2$ is assumed to equal to 1, given that the cross section of the fiber is essentially an oval-shape with the fiber top having a

relatively smaller curvature. This simplification is also adopted by other researchers [27, 69], who assume the fiber top as a plane for simplicity. Then, Eq. (5.5) is simplified as:

$$\cos\theta_A = -1 + f\left(1+\cos\theta_Y\right) \tag{5.6}$$

where $f$ is the liquid-solid contact area faction and can be calculated by

$$f = Nd\left(1-f_p\right)/L_t \tag{5.7}$$

where $N$ is the number of fibers across the measured area; $d$ is the average fiber diameter, $f_p$ is the pore area fraction on fiber surfaces; $L_t$ is the total width from the first to the $N^{th}$ measured fiber. The introduction of fiber pores reduces $f$ and ultimately results in an increase in $\theta_A$, as indicated by Eq. (5.6). The decrease in $f$ also explains the observed decrease in $\alpha_r$ because liquid contacts more vapor phase, which reduces the friction that impedes droplet from rolling. The results in Figure 5.3 concur with the earlier works [33, 69] of developing porous surfaces to improve hydrophobicity. So, all fibers are porous in the following studies.

Then the hydrophobicity of uniaxially and biaxially aligned porous fibers are compared. Figure 5.4 shows the measured contact and roll-off angles on surfaces dressed by uniaxially (*see* grey scatters) and biaxially (blue scatters) aligned porous fibers with all fibers having an average diameter of $3.95 \pm 0.25$ μm. The results show that increasing inter-fiber distance ($l$) from about 9 to 18.2 μm in both structures improves the hydrophobicity, as evidenced by the increased $\theta_A$ and decreased $\alpha_r$ from about 145˚ and 55˚ to 150˚ and 35˚, respectively. The increased $\theta_A$ with enlarging $l$ suggests a CB wetting state. Specifically, in the CB state, droplets are supported by fibers without touching the bottom substrate. As a result, increasing inter-fiber distance in CB state reduces the liquid-solid contact fraction $f$, thereby increasing the $\theta_A$ (see Eq. 5.6). Moreover, this decrease in $f$ also explains the observed decrease in $\alpha_r$ because decreasing $f$ reduces the liquid-solid contacting fraction, which reduces the friction that impedes droplet from rolling. In the rest of this study, this correlation between $\theta_A$, $\alpha_r$, and $f$ is used to interpret changes in hydrophobicity for fiber-dressed surfaces before liquid wets the substrate (i.e., hydrophobicity improves with decreasing $f$, and vice versa).

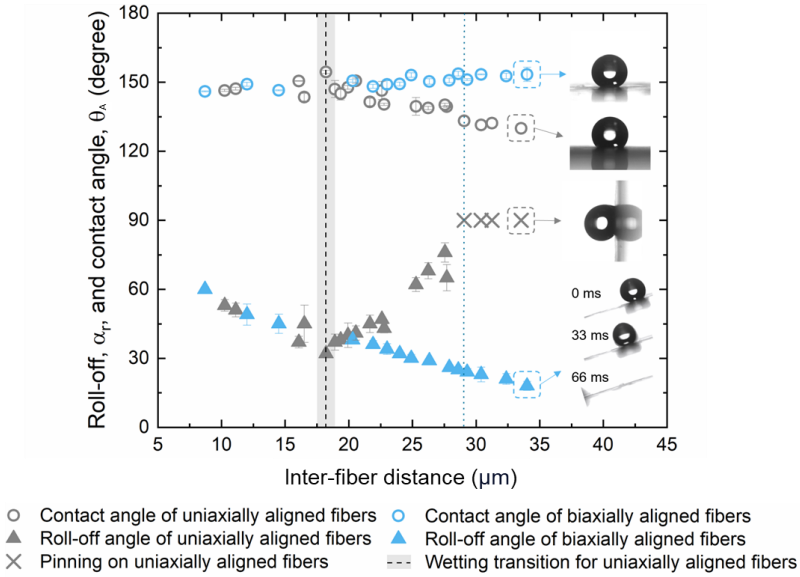


**Figure 5.4.** Measured contact angle and roll-off angle on surfaces dressed by uniaxially or biaxially aligned porous fibers (water droplets with volume of 3 μL).

The wetting behavior of droplets on these two fibrous structures diverges when the inter-fiber distance ($l$) is above 18.2 μm. For the uniaxial structure, further increasing $l$ from 18.2 μm to 33.5 μm weakens the hydrophobicity, as evidenced by the decrease of $\theta_A$ from 155˚ to 130˚ and the increase of $\alpha_r$ from 32˚ to a sticky state even at 90˚ tilting angle. This result indicates that a wetting transition occurs at $l > 18.2$ μm for the surfaces dressed by uniaxially aligned porous fibers: at this $l$, the liquid starts filling up some of many inter-fiber grooves under the droplet; further increasing $l$ leads to more grooves filled by liquid and eventually results in the Wenzel state when the droplet fully wets the underlying substrate. The wetting transition weakens hydrophobicity since the liquid-solid contact fraction greatly increases once the droplet touches the substrate, enhancing the adhesion between the droplet and the covered area. In contrast, this wetting transition is not observed for droplets on the biaxially aligned porous fibers for $l$ between 18.2-34 μm: the hydrophobicity continues to improve without a sudden change for all the $l$ tested.

The experimental results are unexpected for the biaxial structure in Figure 5.4. Note that the biaxial structure is essentially a stacking of two layers of uniaxially aligned fibers in the warp and weft directions, and therefore the droplets on the biaxial structure are expected to

behave in the same way as on the uniaxial structure before reaching the lower-layer fibers. One would then intuitively expect that the wetting of the biaxial structure would transit to a state where the droplet contacts the lower-layer fibers once the $l$ is greater than 18.2 μm. The reason is that at this $l$, the same droplet on the uniaxial structure would have touched the substrate. Had the droplet touched lower-layer fibers, the measured $\theta_A$ and $\alpha_r$ should have suddenly dropped and risen, respectively, because of the increase in liquid-solid contact fraction $f$. This weakening of hydrophobicity is expected to occur, even if it may not be as severe as seen in the uniaxial structure when $l$ >18.2 μm. However, the hydrophobicity of the biaxial structure maintains an unchanged trend for the tested $l$ range of 8.7 to 34 μm. This unchanged relationship suggests that the liquid droplets did not touch the lower-layer fibers, i.e., the CB state is maintained.

In addition, the evidence from the free evaporation of an identical droplet on the biaxial structure further confirms that droplet is in CB state for $l$ >18.2 μm without contacting the lower-layer fibers. In Figure 5.5, the deformations of liquid edges due to the capillary force evidence that the droplet is in contact with upper-layer fibers (*see* the yellow dot lines). The interaction between the droplet and the lower-layer fibers is not observed until the last few seconds of the evaporation (the red dot lines). Thus, the evaporating droplet is in CB state until the last few seconds. Note that the CB state is more stable prior to evaporation because the evaporation is essentially a trigger that weakens the stability of CB state and increases the tendency of wetting transition (i.e., evaporation-triggered wetting transition [153]). In addition to observing droplet evaporation, an inverted laser scanning confocal microscope [154] can also help to confirm the CB state of droplets by directly imaging the underneath liquid-vapor interface.

To understand the mechanism behind the preceding unexpected phenomenon, we map our experiment points into the wetting state chart of the uniaxial structure. Figure 5.6 presents the wetting states of a 3 μL water droplet on the uniaxial structure with different inter-fiber distances ($l$). The Cassie-Baxter region, i.e., blue region in Figure 5.6, is obtained as follows.

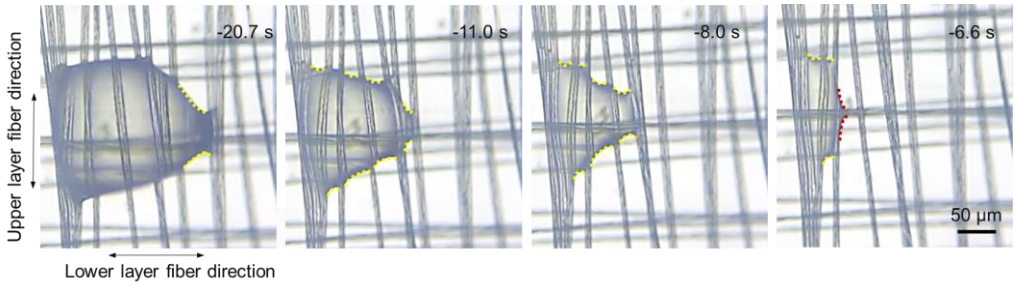


**Figure 5.5.** Images of the final seconds of droplet free evaporation on the biaxially aligned porous fibers.

In wetting transition, the change of free energy ($\Delta G$) can be expressed as follows based on Eq. (3.14).

$$\frac{\Delta G}{\gamma_{LV}} = -\left[ l\left(1+\cos\theta_{Y,S}\right) - d\sin\theta_{Y,F} - d\left(1-f\right)\theta_{Y,F} + df\,\theta_{Y,F}\cos\theta_{Y,F} \right] \tag{5.8}$$

where $\theta_{Y,F}$ and $\theta_{Y,S}$ denote the intrinsic contact angles of the fiber and the substrate material, respectively; $d$ is the fiber diameter, and $f$ is the liquid-solid contact area fraction. The CB state dominates when it is thermodynamically more stable than the Wenzel state, i.e., $\Delta G > 0$, which derives Eq. (5.9).

$$l < \frac{d\left(\sin\theta_{Y,F} + \left(1-f\right)\theta_{Y,F} - f\cos\theta_{Y,F}\right)}{1+\cos\theta_{Y,S}} \tag{5.9}$$

Then, substituting the structure parameters and the material properties of the developed fibers in this study (i.e., $d$=3.95 μm, $f$ = 0.5, $\theta_{Y,F}$ = 95˚, $\theta_{Y,S}$ = 95˚) into Eq. (5.9) leads to the result of $l$ < 8.2 μm. Finally, this result is used to determine the CB region in Figure 5.6.

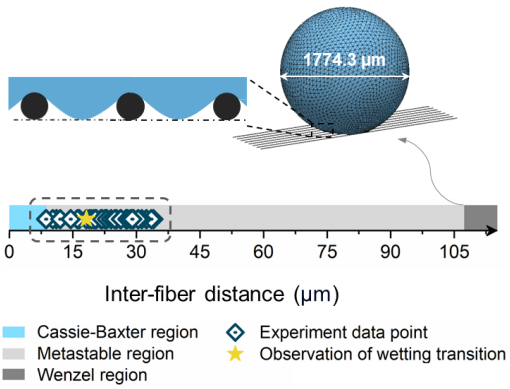


**Figure 5.6.** Experimental data points mapped in a wetting state chart obtained by modeling

the uniaxially aligned fibrous structure with a fiber diameter of 3.95 μm.

In contrast, as simulated by the numerical model in SE, $l$ greater than 107.4 μm (the dark grey region in Figure 5.6) results in the Wenzel state because the bottom of the liquid-vapor interface reaches the level of the fiber bottom (*see* the inset in Figure 5.6). Thus, the wetting transition from CB to Wenzel state due to sagging effect [9] is expected when in contact with the substrate. However, there is a metastable region where the CB state could sustain despite being energetically less stable than the Wenzel state [155, 156]. The metastable CB state occurs because the additional energy acquired by the droplet from environment cannot overcome the free energy barrier between the CB and Wenzel states [157] (as discussed in Section 3.2.3). In Figure 5.6, the experimentally observed wetting transition for the uniaxial structure falls into the metastable region, which indicates that the energy barrier separating the CB and Wenzel states is overcome by the environmental disturbances once $l$ is greater than 18.2 μm. Based on this analysis, it can be inferred that the biaxial structure's advantage over the uniaxial structure in resisting wetting transition, as observed in Figure 5.4, can be attributed to its enhanced energy barrier between the CB and Wenzel states. However, this argument still leaves a question of why a droplet is in CB state on the biaxial structure instead of a transitional state between CB and Wenzel that touches the lower-layer fibers. Then we further map a more detailed energy profile for droplets wetting surfaces dressed by fibrous structures in the following section.

### 5.4.3 Modeling of droplet wetting fiber-dressed surface

The model parameters of droplet volume, fiber diameter, and pore area fraction on the fiber-surface are 3 μL, 4 μm, and 0.5, respectively, which are consistent with those in preceding experiment of Figure 5.4; inter-fiber distance $l$ is set as 30 μm because the wetting behaviors of droplets on the biaxial and uniaxial structures are notably different for $l > 29$ μm (shown as the blue dotted line in Figure 5.4, droplets are pinned on the uniaxial structure while roll off the biaxial structure). The amended $\theta_{Y,F}$ for the PS porous fibers is calculated to be 123° using Eq. (5.4).

Based on the model, we particularly studied the free energy of droplets in CB, Wenzel, and two transitional states to map the energy profile for droplet wetting fibrous structures. Figure 5.7 shows the variation of free energy in wetting surfaces dressed by aligned porous fibers. As illustrated in Figure 5.7(A), State(i) is the transitional state in which the droplet just starts to encounter the solids beneath the upper-layer fibers. The solid is the substrate surface for the uniaxial structure or the lower-layer fibers for biaxial structure. States(ii) represents any transitional states between State(i) and Wenzel state, e.g., State(ii′) and (ii″), in which the liquid partially wets the beneath solid. The normalized free energy of the droplet at CB, Wenzel and two transitional state is denoted as $\bar{G}_{CB}$, $\bar{G}_{W}$, $\bar{G}_{i}$ and $\bar{G}_{ii}$, respectively.

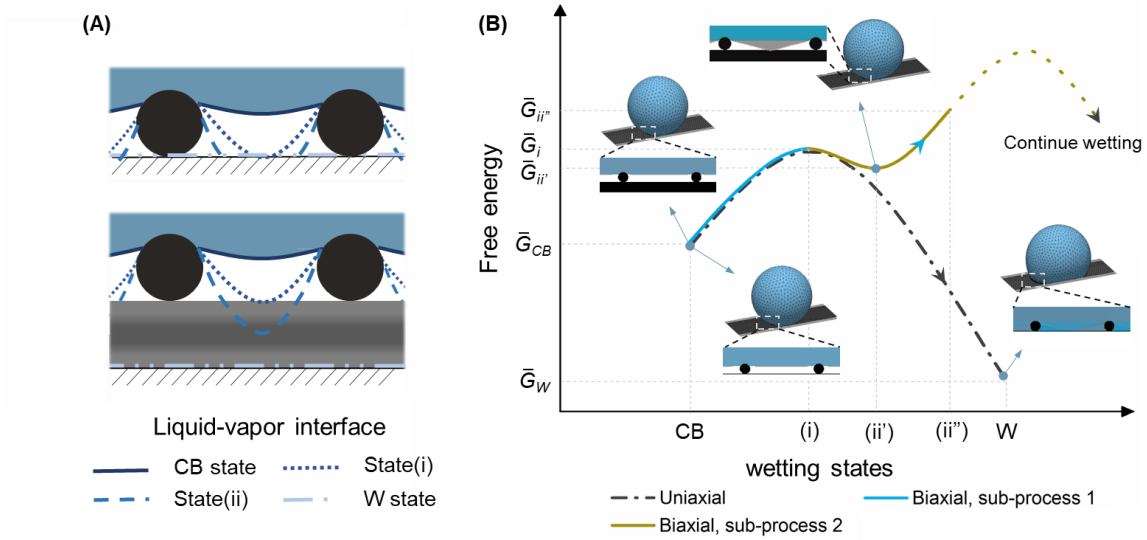


**Figure 5.7.** (A) Illustration of four different wetting states. (B) Energy profile for a water droplet wetting uniaxial and biaxial structures, the insets are the wetting states with a local minimum of free energy obtained from modeling.

The grey dash-dot line in Figure 5.7(B) illustrates the mapped energy profile derived for wetting the surface dressed by uniaxially aligned porous fibers. The profiled is mapped as $\bar{G}_{i} > \bar{G}_{CB} > \bar{G}_{W}$ because the model results identify CB and Wenzel as the wetting states with the lowest free energy before and after the droplet touching the substrate, respectively. The normalized free energy (with respect to $\gamma_{LV} d_c^2$) difference between CB and Wenzel states

is 15,176.4. In addition, the free energy level of State(i) is at the peak because State(i) is a transitional state with the largest liquid-vapor interface (*see* Figure 5.7(A) and Eq. 5.1). This energy profile concurs with the experimental results in Figure 5.4 in which the Wenzel state occurs on the uniaxial structure with an inter-fiber distance of 30 μm because $\bar{G}_W$ is the lowest among all wetting states.

However, as shown in Figure 5.7(B), the mapped energy profile for wetting the biaxial structure is different from wetting the uniaxial structure. The profile is mapped as $\bar{G}_i > \bar{G}_{ii} > \bar{G}_{CB}$ by dividing the wetting into two consecutive sub-processes, where droplet wets only the upper-layer fibers (i.e., sub-process 1), and both the upper and lower-layer fibers (i.e., sub-process 2). The sub-process 1 is same as the process wetting the uniaxial structure before liquid touches substrate, thereby, we can map $\bar{G}_i > \bar{G}_{CB}$. For the sub-process 2, the modeling results show that there is a metastable state, i.e., State (ii′), soon after State(i) with a local minimum $\bar{G}_{ii'}$, thereby, $\bar{G}_i > \bar{G}_{ii'}$. The obtained $\bar{G}_{ii'}$ is calculated to be greater than $\bar{G}_{CB}$ with $\Delta\bar{G}_{ii'\text{-}CB}$ =9.7. Furthermore, the energy needed for the droplet to continue wetting the biaxial structure beyond State(ii′) is larger than the energy at State(i). As an evidence, we identify a follow-up state before reaching the underlying substrate, denoted as State(ii″), with a higher free energy than State(i), which is discussed below.

First, we imposed a constraint on Surface Evolver to limit the normalized wetting length ($\bar{l}_w$) of each contact point between the liquid and lower-layer fibers to a small value of <0.1 to estimate $\bar{G}_i$. Then we set $\bar{l}_w$ to be longer than that of State(ii′) to estimate the free energy of a state that comes after State(ii′), i.e., State(ii″). Figure 5.8 shows the modeling results of State(i), State(ii′), and State (ii″) with corresponding cross-section view and $\bar{l}_w$. The free energy of State(ii″) is already higher than that of State(i) with the normalized $\Delta\bar{G}_{ii''-i} = 7.8$, even though the lower-layer fiber is not yet fully wetted at State(ii″).

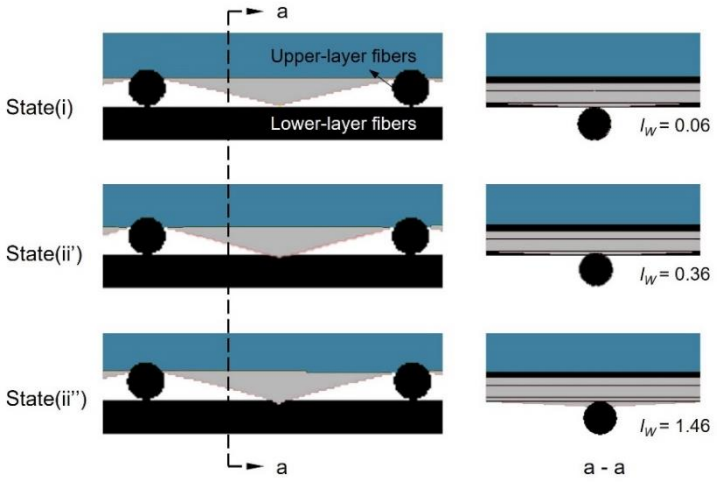


**Figure 5.8.** Modeling results from Surface Evolver showing three wetting states with cross-section views. $\bar{l}_w$ is the normalized wetting length between liquid and the lower-layer fiber.

The energy profile in Figure 5.7(B) for the biaxial structure can explain the unexpected phenomenon in Figure 5.4 for inter-fiber distance between 18.2 and 34 μm, that is even if the droplet touches the lower-layer fibers of a biaxial structure, the droplet could "restore" CB state. To highlight this special phenomenon, we denote this Cassie-Baxter-"restoring" process as CaRe wetting. This CaRe wetting occurs on the biaxial structure because (1) the overall greater energy barrier to the Wenzel state compared to that for the uniaxial structure hinders the droplet from further wetting the lower-layer fibers, and (2) the local minimum $\bar{G}_{ii'}$ for the metastable State(ii′) is greater than $\bar{G}_{CB}$ (i.e., $\Delta\bar{G}_{ii'\text{-}CB}$ =9.7) which allows the droplet to reclaim the CB state for being thermodynamically more stable. It should be noted that, the porous fiber-surface also contributes to realizing the CaRe wetting because the pores in fibers ensure that the water droplet still contacts vapor phase when the droplet touches the lower layer fibers, which elevates $\bar{G}_{ii}$ and makes State(ii′) less stable than the CB state.

We further study the influence of the structure parameters on the CaRe wetting, aiming at providing guidance for structure optimization. The influence is evaluated by the free energy difference between the CB state and State(ii′), i.e., $\Delta\bar{G}_{ii'\text{-}CB}$; a higher $\Delta\bar{G}_{ii'\text{-}CB}$ facilitates the CaRe wetting and also leads to a more stable CB state. Figure 5.9 shows the influence of structure parameters on $\Delta\bar{G}_{ii'\text{-}CB}$.

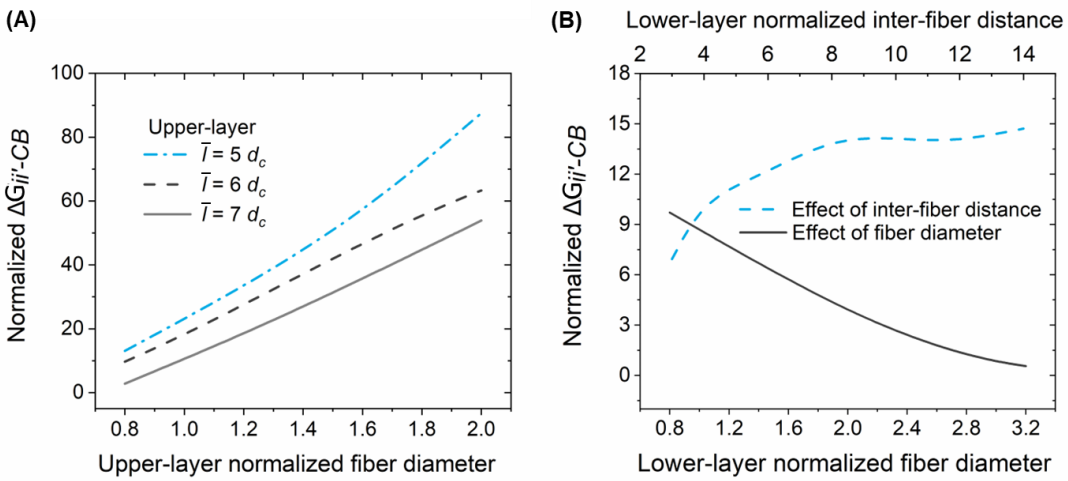


**Figure 5.9.** (A) Normalized $\Delta\bar{G}_{ii'\text{-}CB}$ vs. upper-layer fiber diameter and inter-fiber distance of the biaxial structure; the normalized low-layer fiber diameter and inter-fiber distance are 0.8 and 6, respectively. (B) Normalized $\Delta\bar{G}_{ii'\text{-}CB}$ vs. lower-layer fiber diameter and inter-fiber distance; the normalized upper-layer fiber diameter and inter-fiber distance are 0.8 and 6, respectively.

Figure 5.9(A) shows a positive correlation between the increase in fiber diameter ($\bar{d}$) and the decrease in inter-fiber distance ($\bar{l}$) of the upper-layer fibers with $\Delta\bar{G}_{ii'\text{-}CB}$. In detail, the normalized $\Delta\bar{G}_{ii'\text{-}CB}$ increases 19.3 times when increasing the normalized upper-layer $\bar{d}$ from 0.8 to 2 while $\bar{l} = 7$; further decreasing $\bar{l}$ from 7 to 5 results in an additional 62.3% increase in the normalized $\Delta\bar{G}_{ii'\text{-}CB}$. This is because increasing $\bar{d}$ or decreasing $\bar{l}$ of the upper layer requires greater deformation and thereby more energy for the droplet to wet the lower-layer fibers.

Figure 5.9(B) shows the variations of $\Delta\bar{G}_{ii'\text{-}CB}$ with changing lower-layer $\bar{d}$ and $\bar{l}$. The normalized $\Delta\bar{G}_{ii'\text{-}CB}$ decreases dramatically by 94.3% when increasing the normalized lower-layer $\bar{d}$ from 0.8 to 3.2 while $\bar{l} = 6$. This is because a larger lower-layer fiber diameter means a smaller curvature of the liquid-fiber contact interface, enabling the droplet to wet the lower-layer fibers with smaller deformation; as a result, the $\bar{G}_{ii'}$ is reduced. Moreover, the normalized $\Delta\bar{G}_{ii'\text{-}CB}$ increases by 51.0% when increasing the normalized lower-layer $\bar{l}$ from

3 to 8 while $\bar{d} = 0.8$; but further increasing $\bar{l}$ from 8 to 14 leads to a small $\Delta\bar{G}_{ii'-CB}$ variation of less than 4.0%. The change in $\Delta\bar{G}_{ii'-CB}$ with lower-layer $\bar{l}$ is attributed to the interference of liquid-fiber interfaces among adjacent lower-layer fibers caused by surface tension of liquid. For the lower-layer $\bar{l}$ in the range of 3-8, the interference between adjacent liquid-fiber interfaces is reduced with increasing $\bar{l}$, resulting in a more stable CB state as reflected by the increase in $\Delta\bar{G}_{ii'\text{-}CB}$. However, for lower-layer $\bar{l}$ greater than 8, the interference is further reduced, leading to an insignificant effect of $\bar{l}$ on $\Delta\bar{G}_{ii'\text{-}CB}$.

In summary, the energy profile in Figure 5.7(B) unveiled the CaRe wetting that explains the observed CB state for the biaxial structure in experiment whereas the uniaxial structure reaches Wenzel state. The occurrence of CaRe wetting is related to the structure parameters of the biaxially aligned porous fibers: increasing the upper-layer $\bar{d}$ (from 0.8 to 2), lower-layer $\bar{l}$ (from 3 to 8), and decreasing the upper-layer $\bar{l}$ (from 7 to 5), lower-layer $\bar{d}$ (from 3.2 to 0.8) facilitates the CaRe wetting and results in a stable CB state. In this study, the CaRe wetting is considered the key advantage of the biaxial structure which enables us to further adjust the structural parameters to achieve superhydrophobicity (i.e., $\theta_A > 150^\circ$ and $\alpha_r < 10^\circ$).

### 5.4.4 Achieving lotus effect by a rational approach

This section follows the guidance obtained from Figure 5.9 to construct the biaxial structure that facilitates CaRe wetting and further adjusts the structure parameters by experiments to realize superhydrophobicity. Considering the practical fabrication range of electrospinning and the preceding guidance, we construct the upper-layer fibers with diameter of $8.1 \pm 0.62$ μm, while the lower-layer fibers are smaller in diameter at $3.95 \pm 0.25$ μm. This combination of fiber diameters can promote CaRe wetting, which enables us to strategically approach superhydrophobicity by reducing the liquid-solid contact fraction $f$ through increasing fiber pore size and inter-fiber distance of the upper layer.

Figure 5.10 shows the changes in the measured $\theta_A$ and $\alpha_r$ on the biaxial structure with decreasing $f$. The decrease of $f$ from 0.187 to 0.101 in the yellow shaded area is attributed

to the increase of the pore size from 77 ± 16 to 180 ± 49 nm in fiber-surface (while *l* is kept at 32.0 ± 4.2 µm). The hydrophobicity of the biaxial structure is improved with increasing pore size as evidenced by the increase of $\theta_A$ from 141.0 ± 0.4˚ to 157.3 ± 0.4˚ and the decrease of $\alpha_r$ from 48.0 ± 0.4˚ to 28.4 ± 0.8˚. In addition, the upper-layer *l* is further adjusted with the largest pore size of 180 ± 49 nm. As shown in the blue area of Figure 5.10, reducing *f* from 0.101 to 0.047 by increasing the upper-layer *l* further enhances hydrophobicity. The fiber-dressed surface becomes superhydrophobic when *f* is below 0.053 (corresponding to upper-layer *l* of 81.5 µm). So, the adopted biaxial structure for further studies has *f* values between 0.053-0.047. Further decreasing *f* below 0.047 by increasing the *l* is not adopted because keeping the upper-layer fibers in a closer distance facilitates the CaRe wetting as shown in Figure 5.9(A).

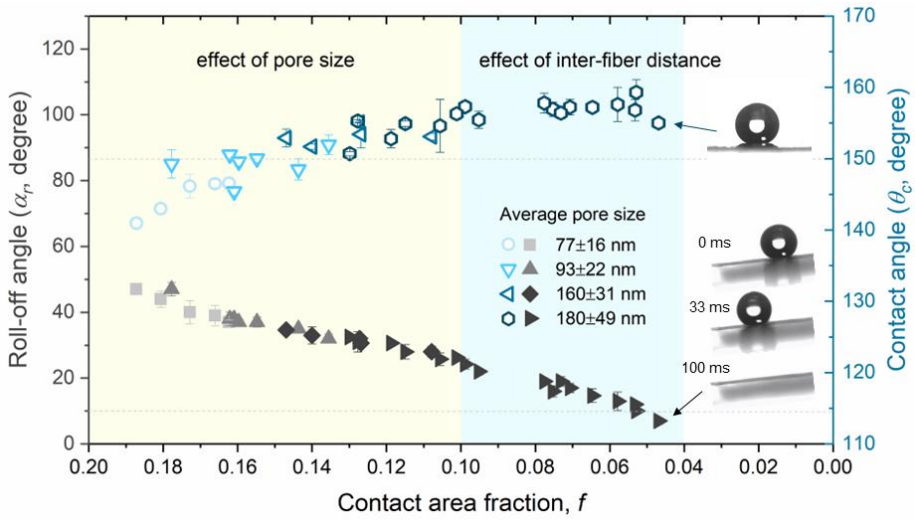


**Figure 5.10.** Influence of upper-layer fiber pore size and inter-fiber distance on the measured contact angle and roll-off angle. The fiber diameters for the upper- and lower-layer are 8.1 ± 0.62 µm and 3.95 ± 0.25 µm, respectively. The inter-fiber distance for both layers in the yellow shaded area and the lower-layer in the blue shaded area are 32.0 ± 4.2 µm.

In contrast to the earlier studies of developing electrospun fiber-based superhydrophobic structures that used a single droplet volume to measure $\theta_A$ and $\alpha_r$ (or a larger droplet volume to measure $\alpha_r$), this study evaluates the hydrophobicity for a range of droplets between 3-

10 µL, as shown in Figure 5.11. The studied droplet volume of 3-10 µL is an appropriate range for characterizing superhydrophobicity by sessile drop method [158].

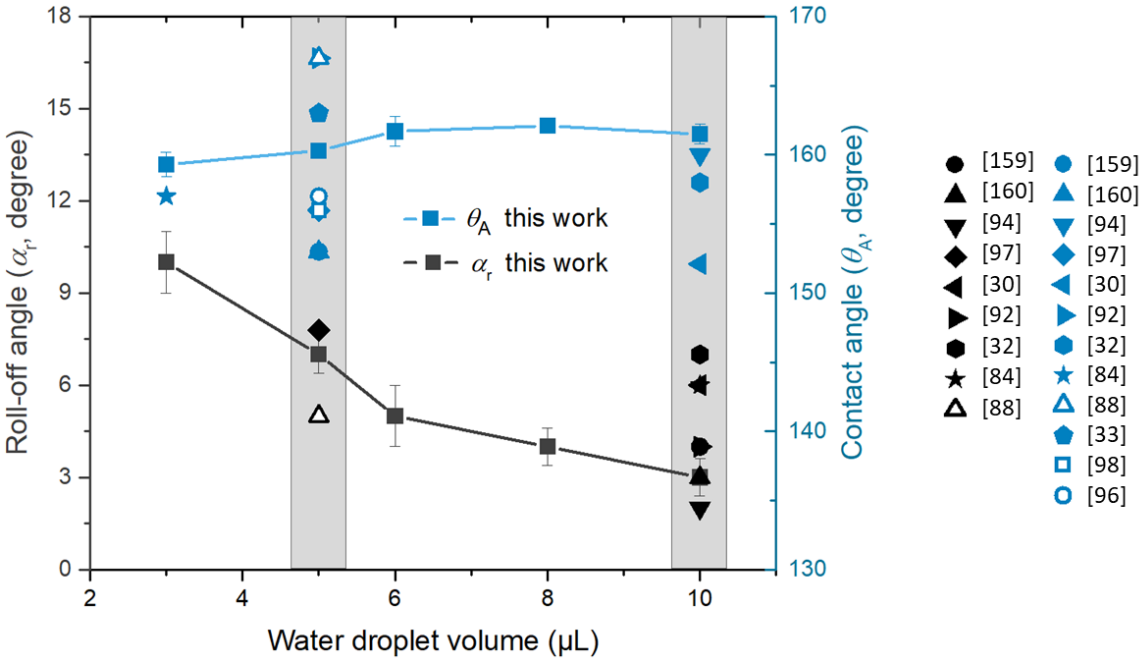


**Figure 5.11.** Variation of hydrophobicity with droplet volumes on the biaxial structure, and comparison to other electrospun fiber-based superhydrophobic surfaces reported in literature [30, 32, 33, 84, 88, 92, 94, 96-98, 159, 160]. The adopted biaxial structure has *f* between 0.053-0.047.

The results in Figure 5.11 show that the influence of droplet volume on $\theta_A$ is negligible because $\theta_A$ maintains relatively stable between $159.3 \pm 0.9^\circ$ and $161.5 \pm 0.7^\circ$ with various droplet volumes. The variation of $2.2^\circ$ is close to the inherent error of sessile drop method for unstructured surfaces (i.e., approximately $\pm 2^\circ$ [161]), and additional minor error may be attributed to the surface heterogeneity of the fibers used in the experiment. In contrast, $\alpha_r$ decreases from $10 \pm 1^\circ$ to $3 \pm 0.6^\circ$ with increasing droplet volume from 3 to 10 µL. This observed trend agrees with the current theoretical correlation between the droplet volume and $\alpha_r$ under CB state, as presented in Eq. (5.10) [162]:

$$\sin \alpha_r = \frac{W}{V}\left[\frac{2\gamma_{LV}\left(1+\cos\theta_{Y,F}\right)\sqrt{f}}{\rho g}\right] \tag{5.10}$$

where $\rho$, $g$, and $V$ represent the droplet density, gravity acceleration, and droplet volume, respectively; $W$ is the droplet contact width. As the droplet volume increases from 3 to 10 μL, there is a 333.3% increase in $V$ and a 169.1% increase in $W$. Substituting this increase of $V$ and $W$ in Eq. (5.10) while keeping all other variables in the square bracket constant for the given biaxial structure, results in a decrease in the roll-off angle.

It is worth noting that the superhydrophobic fibrous structure developed in this study is a one-step approach that uses only one commercially available polymer, which is deemed simple and can reduce the cost of developing electrospun superhydrophobic materials. In contrast, previous technologies typically involve complex fabrication processes and the use of multiple raw materials. For example, preparing fluorinated polymers, blending nano-size additives into solutions, and post treatment of the electrospun fibers are often required (*see* Table 2.1 and Table 2.2).

## 5.5 Summary

This chapter studied the wetting behavior on fiber-dressed surfaces by both experiment and numerical simulation, and developed a lotus-effect surface using aligned porous fibers based on a strategic approach. Based on this research, the following conclusions can be drawn.

(1). On uniaxially aligned porous fibers with average fiber diameter of 4 μm and pore size of 160 nm, droplets are in Cassie-Baxter (CB) state and hydrophobicity increases with the inter-fiber distance ($l$) when $l$ is less than 18.2 μm. After 18.2 μm, wetting transition to Wenzel state occurs, resulting in decrease of hydrophobicity with $l$.

(2). On biaxially aligned porous fibers with similar fiber parameters, droplets stay in CB state and hydrophobicity increases with $l$ until $l = 34$ μm. More importantly, there is no change in trend of hydrophobicity at $l$=18.2 μm, indicating that droplets stay in the upper-layer fibers without touching the lower-layer fibers or substrate.

(3). Energy profiles of droplets wetting the uniaxial and biaxial structures are obtained by numerical simulation in Surface Evolver. Compared to the uniaxial structure, there is a Cassie-Baxter-“restoring” (CaRe) wetting contributing to a more stable CB state in

biaxial structure.

(4). The CaRe wetting ensures droplets stay in CB state even at a large *l* of 81.5 μm, which allows for a rational approach towards superhydrophobicity through increasing inter-fiber distance and increasing pore size. As a result, the developed structure has contact angles between 159˚ and 162˚ and roll-off angles from 10˚ to 3˚ for water droplets from 3 to 10 μL in volume.

# Chapter 6 Potential Applications of the "Lotus" Surface Based on Biaxially Aligned Porous Fibers

Electrospun fibrous structures are featured with high porosity, up to more than 90% [163], with interconnectivity between the inter-fiber pores, which can realize a high breathability. Thus, superhydrophobic and breathable structure, which has wide engineering applications such as wearable electronics [164], personal protections [165], gas sensors [166], etc., can be developed by electrospinning.

The biaxial structure with lotus effect developed in Chapter 5 only consists of two layers of fibers, realizing a total thickness less than 20 μm. In contrast, most earlier reported lotus-effect electrospun structures consist of randomly distributed fibers, so usually a thicker (more than 50 μm [30, 84]) fibrous mat is made to prevent droplet from touching the underneath substrate, which results in Wenzel state. However, increasing structure thickness reduces breathability as air and water vapor needs to transmit the structure with greater resistance. So, it is expected that the biaxial structure can have a high breathability (to be measured in the following section).

In this chapter, two potential applications of the biaxial structure are demonstrated based on the lotus superhydrophobicity and high breathability: developing waterproof, breathable and superhydrophobic membrane, and as a surface layer for protecting wearable electronics.

## 6.1 Waterproof, breathable and superhydrophobic membrane

The developed biaxial structure of aligned porous fibers in Chapter 5 offers an opportunity to address the challenge of developing a simple method for producing waterproof, breathable, and superhydrophobic membrane. The waterproof and breathable membrane that prevents liquid water permeation while allows moisture and air transmission are highly desired for various applications, such as wearable electronics, medical dressing, and desalination [8]. Lotus superhydrophobicity is an additional desired feature for waterproof and breathable

membranes because it enables self-cleaning, which help to maintain the waterproofness and breathability. For fabrication, electrospinning is widely adopted for developing waterproof breathable membranes because the electrospun fibrous structure provides a good basis for breathability [27, 28] owing to its interconnected pores. However, despite the substantial progress made in this field, existing technologies can only achieve two or three out of four features of waterproofing, breathability, superhydrophobicity, and simplicity (*see* Table 6.1). The demonstration of our approach that achieves all four features is shown as follows.

Figure 6.1 demonstrates the application of biaxially aligned porous fibers for developing water-proof, breathable, and superhydrophobic (WBS) membrane. The fibers are dressed on a commercial nylon mesh that is originally water permeable. Despite the biaxially aligned porous fibers being sparsely arranged with only two layers of fibers, they transform the mesh into a waterproof membrane. As shown in Figure 6.1(A), the water passes the pristine mesh and enters the bottom vessel, while the fiber-dressed mesh is capable of holding the water in the top vessel.

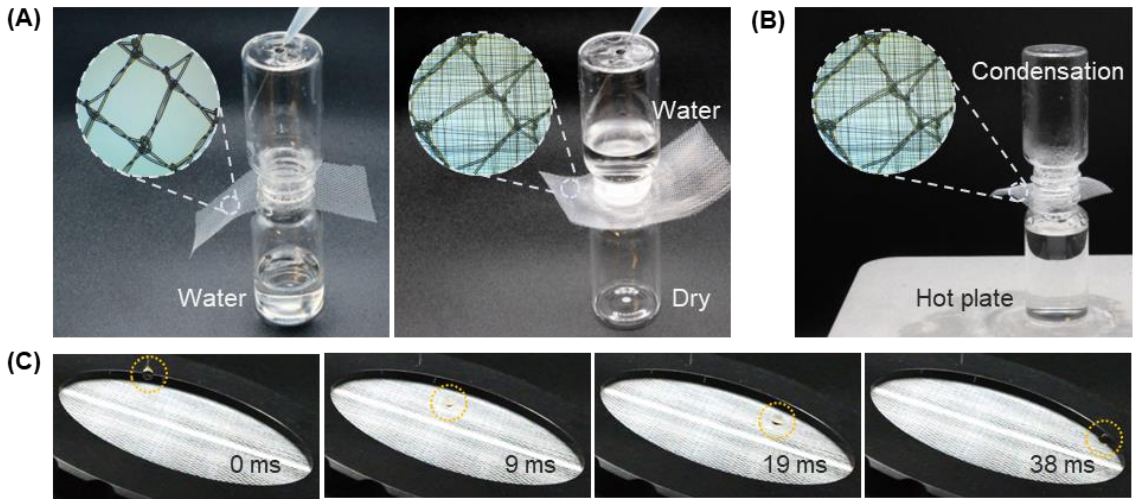


**Figure 6.1.** Development of waterproof, breathable and superhydrophobic membrane by applying biaxially aligned porous fibers on a mesh. Demonstration for (A) waterproofing, (B) breathability, and (C) superhydrophobicity of the fiber-dressed mesh. Insets of (A-B) are the optical microscopic images of the mesh before and after being dressed by the fibers.

**Table 6.1.** Comparison of electrospun waterproof, breathable and superhydrophobic membrane

| Materials | Fabrication | W [1] | B [2] | S [3] | SP [4] | WVTR ($kg \cdot m^2 \cdot d^{-1}$) | WVTR testing condition | Ref. |
|---|---|---|---|---|---|---|---|---|
| FPU/BN | Blending fluorinated polymer and nanosheets for electrospinning | ✓ | ✓ | ✓ | | 11.6 | 38 ˚C, 50% RH, [5] | [159] |
| FPU/PU/PCC | Blending fluorinated polymer and nano-capsules for electrospinning | ✓ | ✓ | ✓ | | 11.4 | 38 ˚C, 50% RH, [5] | [160] |
| PU | Electrospinning of nanosized fibers | ✓ | ✓ | | ✓ | 1.5 | 25 ˚C, 65% RH, [5] | [167] |
| Silk fibroin | Electrospinning of nanosized fibers | | ✓ | | ✓ | 2.0 ± 0.1 | 38 ˚C, 50% RH, [5] | [168] |
| PU/$SiO_2$ | Post-treatments of surface grafting and hydrothermal reaction to electrospun fibers for growing nanoparticles | ✓ | ✓ | ✓ | | 8.4 | - | [30] |
| PVDF | Post-treatments of thermo-pressing to electrospun fibers | ✓ | ✓ | | | 10.9 | 38 ˚C, 90% RH, [6] | [169] |
| PVDF/PVB | Blending two polymers for electrospinning and followed by thermal treatment | ✓ | ✓ | | | 10.6 | 38 ˚C, 90% RH, [6] | [170] |
| PVDF/PVB/ octadecane/CNT | Blending nanosize carbon tubes with polymer solutions for co-axial electrospinning | ✓ | ✓ | | | 7.8 | 38 ˚C, 90% RH, [6] | [171] |
| PAN/FPU | Post thermal treatment to electrospun fibers | ✓ | ✓ | | | 10.1 | 38 ˚C, 90% RH, [6] | [172] |
| PES/$BaTiO_3$ | Blending nanoparticles and polymer solution for electrospinning | | ✓ | | | 6.2 | -, [6] | [173] |
| PS | Electrospinning of aligned porous fibers | ✓ | ✓ | ✓ | ✓ | 20.8 ± 0.1 | 38 ˚C, 90% RH, [6] | this work |

[1] waterproof; [2] breathable; [3] superhydrophobic; [4] simple; [5] test method based on water evaporation; [6] test method based on vapor absorption by desiccant;

Figure 6.1(B) indicates the breathability of the fiber-dressed mesh. Specifically, water vapor generated from heating passes through the fiber-dressed mesh and condenses in the upper vessel. For quantification, the breathability is assessed by water vapor transmission rate (WVTR) test following the ASTM E96 standard. In a typical test, $CaCl_2$ desiccant is sealed by the tested sample in a testing cup with a 25 $cm^2$ opening, which is placed in an environmental chamber controlled at 38 ℃ and 90% RH. The weight of the testing cup is measured every 10 minutes to calculate the WVTR using Eq. (6.1).

$$\mathrm{WVTR} = \frac{\Delta m}{\Delta t \times A_c} \tag{6.1}$$

where $\Delta m$ is the weight change of $CaCl_2$ in $\Delta t$ period and $A_c$ is the cup opening area.

The WVTR of the fiber-dressed mesh is measured to be $20.8 \pm 0.1$ $kg \cdot m^{-2} \cdot d^{-1}$. To the best of our knowledge, this WVTR is the highest value reported so far for electrospun WBS membranes (*see* Table 6.1) due to its large inter-fiber distance and low thickness. Moreover, the biaxially aligned porous fibers also impart superhydrophobicity to the mesh, as indicated by the rapid rolling of a water droplet from its surface in Figure 6.1(C).

It should be noted that the nylon mesh substrate herein is only for demonstration. The developed biaxial structure is essentially a versatile dressing layer that can be applied to various substrates, such as conventional electrospun membranes, microporous media, metal mesh, etc. The choice of substrate depends on mechanical strength, hydrostatic pressure, breathability, and so on, in various applications. For example, Figure 6.2 demonstrates the modification of a pristine electrospun PVDF-HFP membrane. Prior to modification, water droplets are observed to be pinned on the surface of the PVDF-HFP membrane, even when placing the membrane vertically as shown in Figure 6.2 (A). In contrast, after dressing the membrane with the biaxially aligned porous fibers, the droplet rapidly rolls off the surface as shown in Figure 6.2 (B).

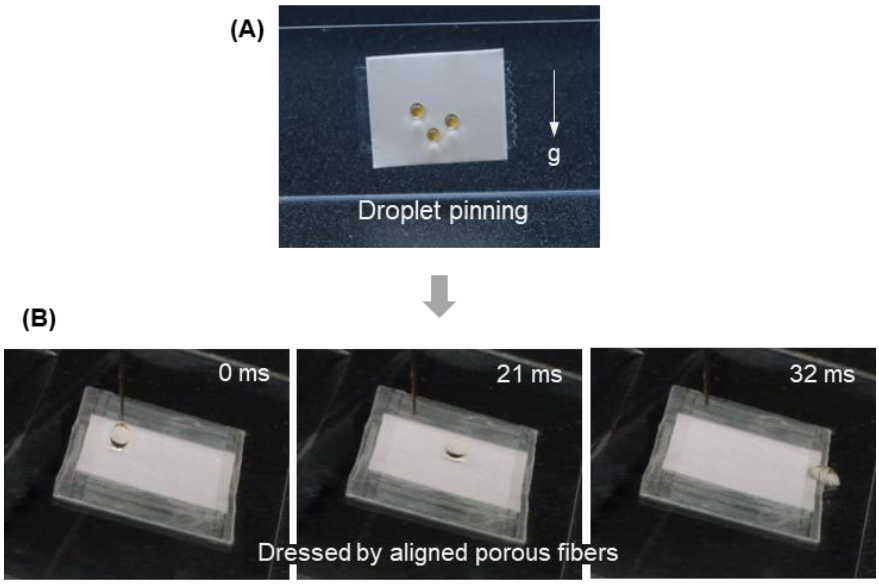


**Figure 6.2.** Modifying an electrospun PVDF-HFP membrane from (A) droplet-pinning to (B) lotus superhydrophobicity by dressing the biaxially aligned porous fibers.

## 6.2 Surface layer for wearable electronics

The emerging wearable electronics have advanced considerably for healthcare monitoring, energy harvesting, human-machine interface, and so on. To ensure user comfort and device longevity, it is important to incorporate a breathable superhydrophobic surface layer into the wearable electronics. The surface layer allows for sweat evaporation, preventing skin irritation and inflammation from prolonged use [174], and protects the underlying electronics from wetting damage. This section demonstrates such an application, where a flexible nylon web, representing an electronic layer, is patched onto a human forearm with a surface layer of the developed biaxially aligned porous fibers.

Figure 6.3 (A) and (B) show the temperature change of the skin being patched by a non-breathable adhesive tape and the developed biaxial structure, respectively. The temperature change of the skin after being covered for 60 minutes reflects the influence of the patched material on sweat evaporation. A material with inadequate breathability causes a temperature drop due to the evaporation of the accumulated sweat, *see* Figure 6.3 (A). In contrast, the skin shows unnoticeable temperature change after being covered by the biaxial structure as

shown in Figure 6.3 (B), indicating sufficient breathability for wearable uses. In addition, Figure 6.3 (C) indicates that a water droplet can rapidly roll off the same biaxial structure, which demonstrates its water repellence if used as a surface layer for wearable electronics on human skin. This characteristic is particularly useful in protecting electronics devices that are sensitive to water intrusion [175], such as wearable nano-generators.

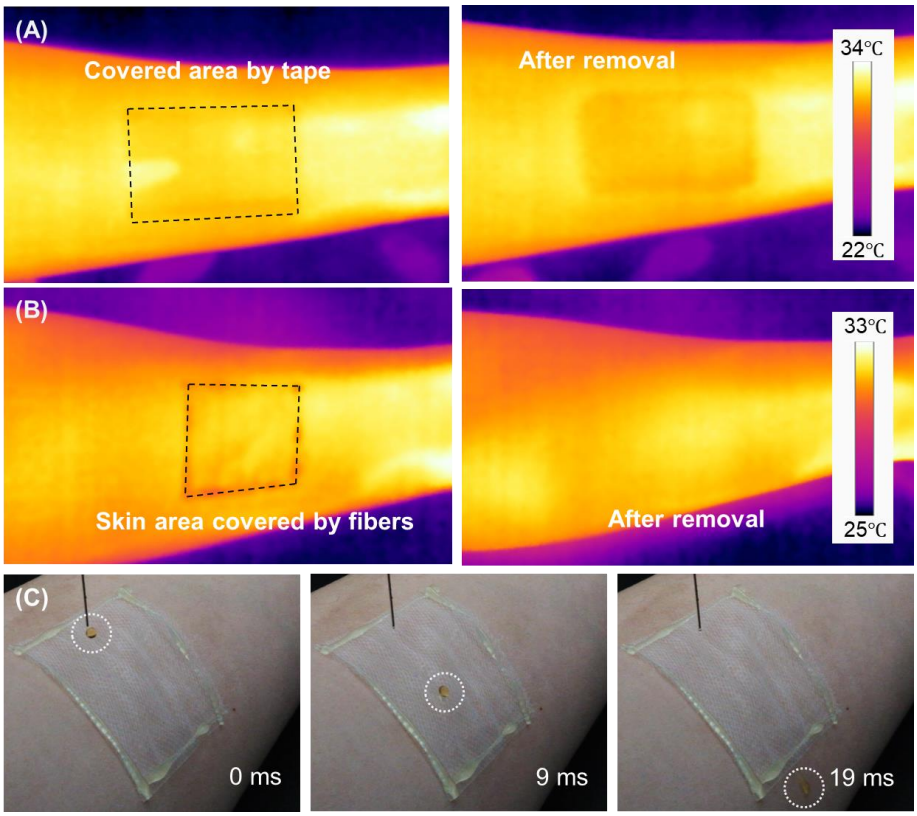


**Figure 6.3.** Development of the surface layer for protecting wearable electronics. Thermal camera images of human forearm skin, which is patched by (A) a non-breathable adhesive tape and (B) the developed biaxial structure for 60 min and removal afterward. (C) Super-hydrophobicity of forearm skin area covered by the developed biaxial structure. Water droplet is dyed in orange.

In addition, Figure 6.4 shows that the developed biaxial structure has a high transparency as the pattern under the fiber-dressed glass slide is visible. The transparency of the biaxial structure is characterized using a UV-Vis spectrophotometer. The average transmittance in

the visible region (380-760 nm) is 83.6 ± 3.1%. The transparency can be useful for allowing direct observation and close monitoring of wearable electronics.

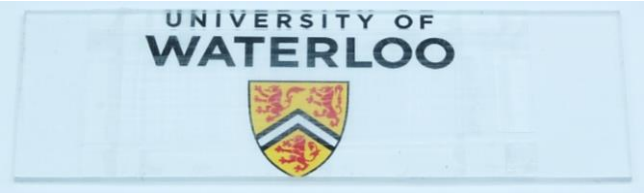


**Figure 6.4.** Transparency of the developed biaxially aligned porous fibers

# Chapter 7 Conclusions and Future Works

## 7.1 Conclusions

Based on the wetting behavior on fiber-dressed surfaces, this thesis develops rose-petal and lotus superhydrophobic surfaces using uniaxially aligned fibers and biaxially aligned porous fibers, respectively, both fabricated by simple one-step electrospinning.

An integrated thermodynamic model for droplet wetting on various parallel-structured surfaces is established to understand the wetting behavior. The model relates free energy with the continuous movement of the three-phase contact line (TPCL) in different wetting states, and the forming conditions of energy barrier are derived from the model. Then, the model are validated using existing works and the experimental data by aligned fibers. The model indicates that for surfaces patterned by sharp-edge structures (cross-section shape) with an internal angle $\varphi$ and an intrinsic contact angle $\theta_Y$, the initiating and ending apparent contact angles (APCA, $\theta_A$) for energy barrier in noncomposite state are $\theta_Y + \varphi$ and $\theta_Y - \varphi$, respectively. For the round structures, an energy barrier may form for every structure at $\theta_A + (180^\circ - \theta_Y)$ in noncomposite state because the round surface has continuous inclination angles with respect to the horizontal plane. Thus, surfaces patterned with round structures, such as fibers, can achieve a large contact angle with a high contact angle hysteresis, which is needed for petal superhydrophobicity.

Then this thesis studies the influence of fiber parameters on the surface wettability and develops petal-effect surfaces based on uniaxially aligned fibers. First, the wetting model for surfaces dressed by aligned fibers is specified based on the integrated model mentioned above. The model indicates that the magnitude of energy barrier, which can pin a droplet at a higher APCA than the equilibrium contact angle, increases with the fiber diameter and the basal width of droplet. Uniaxially aligned polystyrene fibers with average diameters of 0.9 μm and 1.8 μm and varying inter-fiber distance ($l$) from 70 μm to 1450 μm are fabricated by one-step electrospinning. At large $l$, > 800 μm, where two fibers can pin a 2 μL droplet,

the maximum APCA of the 1.8 μm fibers is 155˚, compared to 147˚ for 0.9 μm fibers. The greater APCA is due to the higher magnitude of energy barrier for 1.8 μm fibers. When *l* is below 800 μm, two 1.8 μm fibers are unable to pin the droplet because of the reduced energy barrier with basal width, so three fibers are wetted. Similar variation pattern of APCA by reducing *l* are observed for three to five fibers. However, there is an increase of the overall APCAs due to that more energy barriers are induced to attenuate the perturbation energy.

Petal-effect surfaces are developed based on uniaxially aligned polystyrene fibers with diameter of 1.8 μm and inter-fiber distance between 70 μm and 130 μm. The APCAs of the fiber-dressed surfaces are in a range of 150˚-156˚, and droplets can adhere to the surfaces even by turning surfaces upside down.

After that, this thesis studies the wetting behaviors on surfaces dressed by aligned porous fibers and develops a lotus-effect surface using biaxially aligned porous fibers. In experiment, on uniaxially aligned porous fibers with average fiber diameter of 4 μm and pore size of 160 nm, droplets are in Cassie-Baxter (CB) state and hydrophobicity increases with *l* when *l* is below 18.2 μm. After 18.2 μm, the wetting transition to Wenzel state occurs, resulting in decrease of hydrophobicity with *l*. On biaxially aligned porous fibers with similar fiber parameters, droplets stay in CB state and hydrophobicity increases with *l* until $l$=34 μm. More importantly, there is no change in the trend of hydrophobicity at $l$=18.2 μm until 34 μm, indicating that droplets stay in the upper-layer fibers without touching the lower-layer fibers or substrate. To explain the unchanged trend, the energy profiles of droplets wetting uniaxial and biaxial structures are obtained using numerical simulation in Surface Evolver. Compared to the uniaxial structure, a Cassie-Baxter-“restoring” (CaRe) wetting results in a more stable CB state in biaxial structure.

Lotus-effect surfaces are developed based on the CaRe wetting of biaxially aligned porous fibers. The CaRe wetting allows for a rational approach towards superhydrophobicity by increasing inter-fiber distance to 81.5 μm and increasing pore sizes to 180 nm. As a result, the developed structure display contact angles between 159˚ and 162˚ and roll-off angles

from 10˚ to 3˚ for water droplets from 3 to 10 μL in volume.

Finally, the biaxially aligned porous fibers are used to develop a waterproof, breathable, and superhydrophobic membrane by depositing the fibers on a supporting nylon mesh. The biaxial structure transforms the nylon mesh into a waterproof membrane. The breathability of the membrane is characterized by water vapor transmission rate (WVTR) test, resulting in a WVTR of 20.8±0.1 $kg \cdot m^{-2} \cdot d^{-1}$. The membrane is also shown to be superhydrophobic as water droplets rapidly roll off the surface. The second application is to develop a surface layer for protecting wearable electronics. The skin of a human forearm shows unnoticeable temperature change after being patched with a surface layer of the biaxial structure for 60 minutes. Moreover, the average transmittance in visible region (380-760 nm) of the biaxial structure is characterized to be 83.6 ± 3.1% using a UV-Vis spectrophotometer.

Overall, this thesis provides insights into the interfacial behavior of wetting fiber-dressed surfaces, and a rational design of surfaces with controlled wettability, especially rose-petal and lotus superhydrophobicity, using electrospun fibers.

## 7.2 Recommended future works

Based on this thesis, the following recommendations are made for future research works.

(1) **Improving the alignment and distribution uniformity of fibers.** The aligned fibers used in this thesis are fabricated using a conventional electrospinning setup with a rotating fin collector. However, the alignment and uniformity of distribution of fibers are hard to be precisely controlled, as shown in Figure 5.2(E-F), because of the bending instabilities of the jets in electrospinning [59].

Improving the alignment and uniformity of distribution helps to more efficiently control the surface wettability. For example, to develop lotus-effect surfaces using aligned fibers, a higher distribution density of fibers is needed to prevent droplets from penetration if the fibers are poorly aligned and distributed with low uniformity. However, the high density can increase liquid-fiber contact area, causing decreasing of hydrophobicity.

Even though a higher rotating speed of the fin collector can improve the alignment and distribution to some extent, extra stretching is exerted on the unsolidified jets by the collector [176], which may alter the fiber morphology. In addition to the collector rotating speed, the relative humidity, applied voltage, and spinning distance can also influence the alignment of the produced fibers.

Near-field electrospinning (NFES) may be one solution to precisely control the alignment and uniformity of distribution of fibers because it can control the deposition of fibers. The bending instabilities of the jets are avoided in NFES by reducing the spinning distance to several millimeters or below [177].

(2) **Further investigating the surface wettability of aligned fibers.** For the aligned non-porous fibers, the experimental lower limit of inter-fiber distance in this thesis is around 70 μm. This lower limit ensures a noncomposite wetting state for the rose-petal effect. However, further reducing the inter-fiber distance may generate intersections of adjacent fibers, which can change the magnitude of free energy barrier, because of the limited alignment of fibers by conventional electrospinning.

Studying the wetting behavior of droplets for inter-fiber distance lower than 70 μm helps to develop the full spectrum of wettability of fiber-dressed surfaces, facilitating the wetting control, especially for the region between lotus effect and petal effect, by electrospun fibers. In literature, Aziz et al. [178] have established an analytical model to determine the critical inter-fiber distance for the composite state on aligned fibers, and numerically calculated the anisotropic contact angles. Moreover, Meng et al. [114] experimentally studied the wetting behavior on densely aligned fibers with inter-fiber distance below 30 μm. However, super-hydrophobicity is not achieved partially because of the poor alignment of fibers. Therefore, future works may modify the collector for conventional electrospinning or adopt NFES to produce well-aligned fibers with lower inter-fiber distances.

(3) **Enhancing the mechanical strength of the fibrous structure.** As shown in chapter 4 and chapter 5, the structure, especially the morphology and spatial distribution, of fibers is

critical in modifying surface wettability. For instance, increasing the inter-fiber distance may cause the wetting transition of droplets from Cassie-Baxter to Wenzel state, as indicated in Figure 5.4 (A). Therefore, the mechanical strength of the fibrous structure can influence the efficiency and duration of wetting control. However, electrospun fibers have been suffered from a low mechanical strength [179].

To enhance the mechanical strength, future works may focus on the following methods. The first method is to use polymers with higher mechanical strength for electrospinning such as PVDF [180], which also has an intrinsic contact angle close to PS. Second, fibers can be cross-linked at intersections. The cross-linking can not only increase the overall strength of the fibrous structure, but also fix the position of each fiber. Third, for the biaxial structure, more layers of fibers can be added at the bottom since the lotus effect is created by the top two layers. However, this may reduce the breathability of the structure.

(4) **Achieving controlled motion of droplets based on the biaxial structure.** Droplet manipulation attracts much attention for its important role in fields like microfluidics [181]. The biaxial structure in this thesis, which enables droplets easily rolling off, can be modified to achieve controlled motion of droplets.

The modified biaxial structure also contains two layers of fibers: the lower layer still uses aligned porous fibers; the upper layer is produced using NFES to pattern fibers with various shapes, e.g., “S” in shape, but the fiber parameters still follow the guideline for lotus effect developed in Section 5.4.4. As a result, the modified biaxial structure is featured with lotus effect and a patterned upper layer in “S” shape, which serves as a track for droplets . When the surface is tilted to roll-off angle, droplets can roll off the surface following the “S” track. This controlled motion of droplets is expected to have potential applications in microfluidic system, inkjet printing, and water harvesting.

(5) **Controlling the hydrophobicity of the biaxial structure by stretching.** As shown in Figure 5.4 (A), the hydrophobicity of the biaxial structure increases with the upper-layer inter-fiber distance ($l$) when $l$ is less than 35 μm. This relationship can be adopted to control

hydrophobicity as follows. In electrospinning, a flexible frame is attached to the collector such that the fibers are deposited onto the frame; a biaxial structure is produced with a low upper-layer *l*. As a result, the obtained biaxial structure is supported by the flexible frame and has a relatively low hydrophobicity. By stretching the frame along the alignment of the lower-layer fibers, the upper-layer *l* increases, leading to increment of hydrophobicity, even to lotus superhydrophobicity. When the stretching is relaxed, the biaxial structure returns to its low hydrophobicity. Thus, the biaxial structure achieves a reversible transition between droplets-pinning effect to lotus effect by stretching the frame of the structure.

Furthermore, it is worth studying the change of wetting behaviors for droplets that have already been on the surface in stretching the frame. If the on-surface droplets also become easier to roll off, the biaxial structure is able to control the movement of droplets. This ability can be useful in water collection, i.e., collecting droplets by relaxing frame and transporting droplets by stretching frame.

(6) **Exploring the use of fiber-surface pores.** First, the fiber-surface pores can be filled with therapeutic compounds and then applied in wound dressing or tissue engineering. For example, a biaxial structure, where the lower-layer porous fibers are filled with drugs, can be used in wound dressing. After patching the biaxial structure on the wound, the low layer can release the filled drug to the wound. At the same time, the biaxial structure provides a self-cleaning, breathable and waterproof surface to the wound. Furthermore, porous cellulose acetate fibers can be added below the biaxial structure for the biocompatibility of cellulose acetate. Moreover, the nanoscale surface roughness on porous cellulose acetate fibers can improve cell attachment [182]. Fabrication of porous cellulose acetate fibers with various pore sizes based on electrospinning is provided in Appendix A. Second, the pores can be filled with phase change material for temperature control of WBS membrane based on the developed biaxial structure.

# References

[1] A. R. Parker, C. R. Lawrence. "Water capture by a desert beetle," *Nature,* vol. 414, no. 6859, pp. 33-34, 2001.

[2] J. Long, M. Hyder, R. Huang, P. Chen. "Thermodynamic modeling of contact angles on rough, heterogeneous surfaces," *Advances in colloid and interface science,* vol. 118, no. 1-3, pp. 173-190, 2005.

[3] C. Jothi Prakash, R. Prasanth. "Approaches to design a surface with tunable wettability: a review on surface properties," *Journal of Materials Science,* vol. 56, pp. 108-135, 2021.

[4] Z. Wang, M. Elimelech, S. Lin. "Environmental applications of interfacial materials with special wettability," *Environmental science & technology,* vol. 50, no. 5, pp. 2132-2150, 2016.

[5] L. Sun, J. Guo, H. Chen, D. Zhang, L. Shang, B. Zhang, *et al*. "Tailoring materials with specific wettability in biomedical engineering," *Advanced Science,* vol. 8, no. 19, p. 2100126, 2021.

[6] J. Drelich, E. Chibowski. "Superhydrophilic and superwetting surfaces: definition and mechanisms of control," *Langmuir,* vol. 26, no. 24, pp. 18621-18623, 2010.

[7] X. Deng, L. Mammen, H.-J. Butt, D. Vollmer. "Candle soot as a template for a transparent robust superamphiphobic coating," *Science,* vol. 335, no. 6064, pp. 67-70, 2012.

[8] D. Ebert, B. Bhushan. "Wear-resistant rose petal-effect surfaces with superhydrophobicity and high droplet adhesion using hydrophobic and hydrophilic nanoparticles," *Journal of Colloid and Interface Science,* vol. 384, no. 1, pp. 182-188, 2012.

[9] E. Bormashenko. "Progress in understanding wetting transitions on rough surfaces," *Advances in colloid and interface science,* vol. 222, pp. 92-103, 2015.

[10] W. Barthlott, C. Neinhuis. "Purity of the sacred lotus, or escape from contamination in biological surfaces," *Planta,* vol. 202, pp. 1-8, 1997.

[11] L. Feng, Y. Zhang, J. Xi, Y. Zhu, N. Wang, F. Xia, *et al*. "Petal effect: a

superhydrophobic state with high adhesive force," *Langmuir*, vol. 24, no. 8, pp. 4114-4119, 2008.

[12] https://commons.wikimedia.org/w/index.php?curid=364500.

[13] Y. Zheng, C. Zhang, J. Wang, Y. Liu, C. Shen, J. Yang. "Robust adhesion of droplets via heterogeneous dynamic petal effects," *Journal of colloid and interface science*, vol. 557, pp. 737-745, 2019.

[14] K. Liu, L. Jiang. "Bio-inspired self-cleaning surfaces," *Annual Review of Materials Research*, vol. 42, pp. 231-263, 2012.

[15] B. Zhang, X. Zhao, Y. Li, B. Hou. "Fabrication of durable anticorrosion superhydrophobic surfaces on aluminum substrates via a facile one-step electrodeposition approach," *Rsc Advances*, vol. 6, no. 42, pp. 35455-35465, 2016.

[16] T. V. Charpentier, A. Neville, P. Millner, R. W. Hewson, A. Morina. "Development of anti-icing materials by chemical tailoring of hydrophobic textured metallic surfaces," *Journal of colloid and interface science*, vol. 394, pp. 539-544, 2013.

[17] Y. Chen, Y. Zhang, L. Shi, J. Li, Y. Xin, T. Yang, *et al*. "Transparent superhydrophobic/superhydrophilic coatings for self-cleaning and anti-fogging," *Applied Physics Letters*, vol. 101, no. 3, p. 033701, 2012.

[18] X. Hong, X. Gao, L. Jiang. "Application of superhydrophobic surface with high adhesive force in no lost transport of superparamagnetic microdroplet," *Journal of the American Chemical Society*, vol. 129, no. 6, pp. 1478-1479, 2007.

[19] A. I. Neto, C. R. Correia, C. A. Custódio, J. F. Mano. "Biomimetic miniaturized platform able to sustain arrays of liquid droplets for high-throughput combinatorial tests," *Advanced Functional Materials*, vol. 24, no. 32, pp. 5096-5103, 2014.

[20] A. Winkleman, G. Gotesman, A. Yoffe, R. Naaman. "Immobilizing a drop of water: Fabricating highly hydrophobic surfaces that pin water droplets," *Nano letters*, vol. 8, no. 4, pp. 1241-1245, 2008.

[21] F. Wang, S. Li, L. Wang. "Fabrication of artificial super-hydrophobic lotus-leaf-like bamboo surfaces through soft lithography," *Colloids and surfaces a: physicochemical and*

*engineering aspects,* vol. 513, pp. 389-395, 2017.

[22] C.-H. Xue, Y.-R. Li, P. Zhang, J.-Z. Ma, S.-T. Jia. "Washable and wear-resistant superhydrophobic surfaces with self-cleaning property by chemical etching of fibers and hydrophobization," *ACS applied materials & interfaces,* vol. 6, no. 13, pp. 10153-10161, 2014.

[23] R. Jafari, S. Asadollahi, M. Farzaneh. "Applications of plasma technology in development of superhydrophobic surfaces," *Plasma Chemistry and Plasma Processing,* vol. 33, pp. 177-200, 2013.

[24] K. Bachus, L. Mats, H. Choi, G. Gibson, R. Oleschuk. "Fabrication of patterned superhydrophobic/hydrophilic substrates by laser micromachining for small volume deposition and droplet-based fluorescence," *ACS applied materials & interfaces,* vol. 9, no. 8, pp. 7629-7636, 2017.

[25] N. Nuraje, W. S. Khan, Y. Lei, M. Ceylan, R. Asmatulu. "Superhydrophobic electrospun nanofibers," *Journal of Materials Chemistry A,* vol. 1, no. 6, pp. 1929-1946, 2013.

[26] M. Zhu, J. Han, F. Wang, W. Shao, R. Xiong, Q. Zhang, *et al*. "Electrospun nanofibers membranes for effective air filtration," *Macromolecular Materials and Engineering,* vol. 302, no. 1, p. 1600353, 2017.

[27] L. Jiang, Y. Zhao, J. Zhai. "A lotus-leaf-like superhydrophobic surface: a porous microsphere/nanofiber composite film prepared by electrohydrodynamics," *Angewandte Chemie-International Edition,* vol. 43, no. 33, pp. 4338-4341, 2004.

[28] J. Lin, Y. Cai, X. Wang, B. Ding, J. Yu, M. Wang. "Fabrication of biomimetic superhydrophobic surfaces inspired by lotus leaf and silver ragwort leaf," *Nanoscale,* vol. 3, no. 3, pp. 1258-1262, 2011.

[29] S. Jin, Y. Park, C. H. Park. "Preparation of breathable and superhydrophobic polyurethane electrospun webs with silica nanoparticles," *Textile Research Journal,* vol. 86, no. 17, pp. 1816-1827, 2016.

[30] H. Gu, G. Li, P. Li, H. Liu, T. T. Chadyagondo, N. Li, *et al*. "Superhydrophobic and

breathable SiO2/polyurethane porous membrane for durable water repellent application and oil-water separation," *Applied Surface Science,* vol. 512, p. 144837, 2020.

[31] M. Ma, R. M. Hill, J. L. Lowery, S. V. Fridrikh, G. C. Rutledge. "Electrospun poly (styrene-block-dimethylsiloxane) block copolymer fibers exhibiting superhydrophobicity," *Langmuir,* vol. 21, no. 12, pp. 5549-5554, 2005.

[32] D. Han, A. J. Steckl. "Superhydrophobic and oleophobic fibers by coaxial electrospinning," *Langmuir,* vol. 25, no. 16, pp. 9454-9462, 2009.

[33] M. Ma, M. Gupta, Z. Li, L. Zhai, K. K. Gleason, R. E. Cohen, *et al*. "Decorated electrospun fibers exhibiting superhydrophobicity," *Advanced Materials,* vol. 19, no. 2, pp. 255-259, 2007.

[34] H. R. Hong, C. H. Park. "The influence of nanostructure on the wetting transition of polyvinylidene fluoride nanoweb: from the petal effect to the lotus effect," *Textile Research Journal,* vol. 91, no. 7-8, pp. 752-765, 2021.

[35] J. Serra, R. Pinto, J. Barbosa, D. Correia, R. Gonçalves, M. Silva, *et al*. "Ionic liquid based Fluoropolymer solid electrolytes for Lithium-ion batteries," *Sustainable materials and technologies,* vol. 25, p. e00176, 2020.

[36] X. Li, X. Yu, C. Cheng, L. Deng, M. Wang, X. Wang. "Electrospun superhydrophobic organic/inorganic composite nanofibrous membranes for membrane distillation," *ACS applied materials & interfaces,* vol. 7, no. 39, pp. 21919-21930, 2015.

[37] A. Marmur. "Soft contact: measurement and interpretation of contact angles," *Soft Matter,* vol. 2, no. 1, pp. 12-17, 2006.

[38] T. Young. "III. An essay on the cohesion of fluids," *Philosophical transactions of the royal society of London,* no. 95, pp. 65-87, 1805.

[39] P.-G. Gennes, F. Brochard-Wyart, D. Quéré, *Capillarity and wetting phenomena: drops, bubbles, pearls, waves*. Springer, 2004.

[40] A. Marmur. "Thermodynamic aspects of contact angle hysteresis," *Advances in colloid and interface science,* vol. 50, pp. 121-141, 1994.

[41] A. Cassie, S. Baxter. "Wettability of porous surfaces," *Transactions of the Faraday*

*society,* vol. 40, pp. 546-551, 1944.

[42]R. N. Wenzel. "Resistance of solid surfaces to wetting by water," *Industrial & Engineering Chemistry,* vol. 28, no. 8, pp. 988-994, 1936.

[43]A. Marmur. "Wetting on hydrophobic rough surfaces: to be heterogeneous or not to be?," *Langmuir,* vol. 19, no. 20, pp. 8343-8348, 2003.

[44]C. H. Kung, P. K. Sow, B. Zahiri, W. Mérida. "Assessment and interpretation of surface wettability based on sessile droplet contact angle measurement: challenges and opportunities," *Advanced Materials Interfaces,* vol. 6, no. 18, p. 1900839, 2019.

[45]G. Whyman, E. Bormashenko. "Wetting transitions on rough substrates: General considerations," *Journal of adhesion science and technology,* vol. 26, no. 1-3, pp. 207-220, 2012.

[46]J. B. Boreyko, C.-H. Chen. "Restoring superhydrophobicity of lotus leaves with vibration-induced dewetting," *Physical review letters,* vol. 103, no. 17, p. 174502, 2009.

[47]R. J. Vrancken, H. Kusumaatmaja, K. Hermans, A. M. Prenen, O. Pierre-Louis, C. W. Bastiaansen, *et al*. "Fully reversible transition from Wenzel to Cassie− Baxter states on corrugated superhydrophobic surfaces," *Langmuir,* vol. 26, no. 5, pp. 3335-3341, 2010.

[48]J. R. Panter, H. Kusumaatmaja. "The impact of surface geometry, cavitation, and condensation on wetting transitions: Posts and reentrant structures," *Journal of Physics: Condensed Matter,* vol. 29, no. 8, p. 084001, 2017.

[49]L. Huang, S. P. Lau, H. Yang, E. Leong, S. F. Yu, S. Prawer. "Stable superhydrophobic surface via carbon nanotubes coated with a ZnO thin film," *The Journal of Physical Chemistry B,* vol. 109, no. 16, pp. 7746-7748, 2005.

[50]Y. I. Yoon, H. S. Moon, W. S. Lyoo, T. S. Lee, W. H. Park. "Superhydrophobicity of PHBV fibrous surface with bead-on-string structure," *Journal of colloid and interface science,* vol. 320, no. 1, pp. 91-95, 2008.

[51]A. Tuteja, W. Choi, J. M. Mabry, G. H. McKinley, R. E. Cohen. "Robust omniphobic surfaces," *Proceedings of the National Academy of Sciences,* vol. 105, no. 47, pp. 18200-18205, 2008.

[52] M. Im, H. Im, J.-H. Lee, J.-B. Yoon, Y.-K. Choi. "A robust superhydrophobic and superoleophobic surface with inverse-trapezoidal microstructures on a large transparent flexible substrate," *Soft Matter,* vol. 6, no. 7, pp. 1401-1404, 2010.

[53] W. S. Wong, N. Nasiri, G. Liu, N. Rumsey-Hill, V. S. Craig, D. R. Nisbet, *et al*. "Flexible transparent hierarchical nanomesh for rose petal-like droplet manipulation and lossless transfer," *Advanced Materials Interfaces,* vol. 2, no. 9, p. 1500071, 2015.

[54] M. Ma, R. M. Hill. "Superhydrophobic surfaces," *Current opinion in colloid & interface science,* vol. 11, no. 4, pp. 193-202, 2006.

[55] T. Subbiah, G. S. Bhat, R. W. Tock, S. Parameswaran, S. S. Ramkumar. "Electrospinning of nanofibers," *Journal of Applied Polymer Science,* vol. 96, no. 2, pp. 557-569, 2005.

[56] Y. Yue, X. Gong, W. Jiao, Y. Li, X. Yin, Y. Si, *et al*. "In-situ electrospinning of thymol-loaded polyurethane fibrous membranes for waterproof, breathable, and antibacterial wound dressing application," *Journal of Colloid and Interface Science,* vol. 592, pp. 310-318, 2021.

[57] F. K. Ko, Y. Wan, "Nanofiber technology," in *Introduction to nanofiber materials*: Cambridge University Press, 2014, pp. 44-63.

[58] G. I. Taylor. "Electrically driven jets," *Proceedings of the Royal Society of London. A. Mathematical and Physical Sciences,* vol. 313, no. 1515, pp. 453-475, 1969.

[59] J. Xue, T. Wu, Y. Dai, Y. Xia. "Electrospinning and electrospun nanofibers: Methods, materials, and applications," *Chemical reviews,* vol. 119, no. 8, pp. 5298-5415, 2019.

[60] B. Zaarour, L. Zhu, X. Jin. "A review on the secondary surface morphology of electrospun nanofibers: formation mechanisms, characterizations, and applications," *ChemistrySelect,* vol. 5, no. 4, pp. 1335-1348, 2020.

[61] M. Ma, Y. Mao, M. Gupta, K. K. Gleason, G. C. Rutledge. "Superhydrophobic fabrics produced by electrospinning and chemical vapor deposition," *Macromolecules,* vol. 38, no. 23, pp. 9742-9748, 2005.

[62] M. Kakunuri, N. D. Wanasekara, C. S. Sharma, M. Khandelwal, S. J. Eichhorn. "Three-

dimensional electrospun micropatterned cellulose acetate nanofiber surfaces with tunable wettability," *Journal of Applied Polymer Science,* vol. 134, no. 15, 2017.

[63] D. Bagrov, S. Perunova, E. Pavlova, D. Klinov. "Wetting of electrospun nylon-11 fibers and mats," *RSC advances,* vol. 11, no. 19, pp. 11373-11379, 2021.

[64] N. Thakur, A. S. Ranganath, K. Agarwal, A. Baji. "Electrospun bead-on-string hierarchical fibers for fog harvesting application," *Macromolecular Materials and Engineering,* vol. 302, no. 7, p. 1700124, 2017.

[65] C. Huang, H. Niu, J. Wu, Q. Ke, X. Mo, T. Lin. "Needleless electrospinning of polystyrene fibers with an oriented surface line texture," *Journal of nanomaterials,* vol. 2012, pp. 1-7, 2012.

[66] C.-L. Pai, M. C. Boyce, G. C. Rutledge. "Morphology of porous and wrinkled fibers of polystyrene electrospun from dimethylformamide," *Macromolecules,* vol. 42, no. 6, pp. 2102-2114, 2009.

[67] Z. Asvar, E. Mirzaei, N. Azarpira, B. Geramizadeh, M. Fadaie. "Evaluation of electrospinning parameters on the tensile strength and suture retention strength of polycaprolactone nanofibrous scaffolds through surface response methodology," *Journal of the mechanical behavior of biomedical materials,* vol. 75, pp. 369-378, 2017.

[68] C. Huang, N. L. Thomas. "Fabrication of porous fibers via electrospinning: strategies and applications," *Polymer Reviews,* vol. 60, no. 4, pp. 595-647, 2020.

[69] Y. Miyauchi, B. Ding, S. Shiratori. "Fabrication of a silver-ragwort-leaf-like super-hydrophobic micro/nanoporous fibrous mat surface by electrospinning," *Nanotechnology,* vol. 17, no. 20, p. 5151, 2006.

[70] J. T. McCann, M. Marquez, Y. Xia. "Highly porous fibers by electrospinning into a cryogenic liquid," *Journal of the American Chemical Society,* vol. 128, no. 5, pp. 1436-1437, 2006.

[71] A. Rawal, S. Shukla, S. Sharma, D. Singh, Y.-M. Lin, J. Hao, *et al.* "Metastable wetting model of electrospun mats with wrinkled fibers," *Applied Surface Science,* vol. 551, p. 149147, 2021.

[72]M. Liang, X. Chen, Y. Xu, L. Zhu, X. Jin, C. Huang. "Double-grooved nanofibre surfaces with enhanced anisotropic hydrophobicity," *Nanoscale,* vol. 9, no. 42, pp. 16214-16222, 2017.

[73]R. S. Kurusu, N. R. Demarquette. "Blending and morphology control to turn hydrophobic SEBS electrospun mats superhydrophilic," *Langmuir,* vol. 31, no. 19, pp. 5495-5503, 2015.

[74]G. Li, Y. Zhao, M. Lv, Y. Shi, D. Cao. "Super hydrophilic poly (ethylene terephthalate)(PET)/poly (vinyl alcohol)(PVA) composite fibrous mats with improved mechanical properties prepared via electrospinning process," *Colloids and Surfaces A: Physicochemical and Engineering Aspects,* vol. 436, pp. 417-424, 2013.

[75]A. Abdal-Hay, H. R. Pant, J. K. Lim. "Super-hydrophilic electrospun nylon-6/hydroxyapatite membrane for bone tissue engineering," *European Polymer Journal,* vol. 49, no. 6, pp. 1314-1321, 2013.

[76]R. Beigmoradi, A. Samimi, D. Mohebbi-Kalhori. "Fabrication of polymeric nanofibrous mats with controllable structure and enhanced wetting behavior using one-step electrospinning," *Polymer,* vol. 143, pp. 271-280, 2018.

[77]E. Schoolaert, L. Cossu, J. Becelaere, J. F. Van Guyse, A. Tigrine, M. Vergaelen, *et al*. "Nanofibers with a tunable wettability by electrospinning and physical crosslinking of poly (2-n-propyl-2-oxazoline)," *Materials & Design,* vol. 192, p. 108747, 2020.

[78]T. Ogawa, B. Ding, Y. Sone, S. Shiratori. "Super-hydrophobic surfaces of layer-by-layer structured film-coated electrospun nanofibrous membranes," *Nanotechnology,* vol. 18, no. 16, p. 165607, 2007.

[79]L. Wang, Y. Zhao, J. Wang, X. Hong, J. Zhai, L. Jiang, *et al*. "Ultra-fast spreading on superhydrophilic fibrous mesh with nanochannels," *Applied surface science,* vol. 255, no. 9, pp. 4944-4949, 2009.

[80]Y. Zhu, J. C. Zhang, J. Zhai, L. Jiang. "Preparation of superhydrophilic α-Fe2O3 nanofibers with tunable magnetic properties," *Thin Solid Films,* vol. 510, no. 1-2, pp. 271-274, 2006.

[81] L. D. Tijing, M. T. G. Ruelo, A. Amarjargal, H. R. Pant, C.-H. Park, D. W. Kim, *et al*. "Antibacterial and superhydrophilic electrospun polyurethane nanocomposite fibers containing tourmaline nanoparticles," *Chemical Engineering Journal,* vol. 197, pp. 41-48, 2012.

[82] Y. Zhu, J. Zhang, Y. Zheng, Z. Huang, L. Feng, L. Jiang. "Stable, superhydrophobic, and conductive polyaniline/polystyrene films for corrosive environments," *Advanced Functional Materials,* vol. 16, no. 4, pp. 568-574, 2006.

[83] M. W. Lee, S. An, S. S. Latthe, C. Lee, S. Hong, S. S. Yoon. "Electrospun polystyrene nanofiber membrane with superhydrophobicity and superoleophilicity for selective separation of water and low viscous oil," *ACS applied materials & interfaces,* vol. 5, no. 21, pp. 10597-10604, 2013.

[84] L. Zhou, C. L. Li, P. T. Chang, S. H. Tan, A. L. Ahmad, S. C. Low. "Intrinsic microspheres structure of electrospun nanofibrous membrane with rational superhydrophobicity for desalination via membrane distillation," *Desalination,* vol. 527, p. 115594, 2022.

[85] V. Pais, M. Navarro, C. Guise, R. Martins, R. Fangueiro. "Hydrophobic performance of electrospun fibers functionalized with TiO2 nanoparticles," *Textile Research Journal,* vol. 92, no. 15-16, pp. 2719-2730, 2022.

[86] M. Kang, R. Jung, H.-S. Kim, H.-J. Jin. "Preparation of superhydrophobic polystyrene membranes by electrospinning," *Colloids and Surfaces A: Physicochemical and Engineering Aspects,* vol. 313, pp. 411-414, 2008.

[87] R. Asmatulu, M. Ceylan, N. Nuraje. "Study of superhydrophobic electrospun nanocomposite fibers for energy systems," *Langmuir,* vol. 27, no. 2, pp. 504-507, 2011.

[88] W. S. Wong, P. Gutruf, S. Sriram, M. Bhaskaran, Z. Wang, A. Tricoli. "Strain Engineering of Wave-like Nanofibers for Dynamically Switchable Adhesive/Repulsive Surfaces," *Advanced Functional Materials,* vol. 26, no. 3, pp. 399-407, 2016.

[89] I. Sadeghi, N. Govinna, P. Cebe, A. Asatekin. "Superoleophilic, mechanically strong electrospun membranes for fast and efficient gravity-driven oil/water separation," *ACS*

*Applied Polymer Materials,* vol. 1, no. 4, pp. 765-776, 2019.

[90]M. E. Callow, R. L. Fletcher. "The influence of low surface energy materials on bioadhesion—a review," *International biodeterioration & biodegradation,* vol. 34, no. 3-4, pp. 333-348, 1994.

[91]F. Zareei Pour, M. M. Sabzehmeidani, H. Karimi, V. Madadi Avargani, M. Ghaedi. "Superhydrophobic–superoleophilic electrospun nanofibrous membrane modified by the chemical vapor deposition of dimethyl dichlorosilane for efficient oil–water separation," *Journal of Applied Polymer Science,* vol. 136, no. 24, p. 47621, 2019.

[92]K. Acatay, E. Simsek, C. Ow-Yang, Y. Z. Menceloglu. "Tunable, superhydrophobically stable polymeric surfaces by electrospinning," *Angewandte Chemie,* vol. 116, no. 39, pp. 5322-5325, 2004.

[93]G. Gong, J. Wu, X. Jin, L. Jiang. "Adhesion tuning at superhydrophobic states: from petal effect to lotus effect," *Macromolecular Materials and Engineering,* vol. 300, no. 11, pp. 1057-1062, 2015.

[94]J.-M. Lim, G.-R. Yi, J. H. Moon, C.-J. Heo, S.-M. Yang. "Superhydrophobic films of electrospun fibers with multiple-scale surface morphology," *Langmuir,* vol. 23, no. 15, pp. 7981-7989, 2007.

[95]F. Zhao, X. Wang, B. Ding, J. Lin, J. Hu, Y. Si, *et al*. "Nanoparticle decorated fibrous silica membranes exhibiting biomimetic superhydrophobicity and highly flexible properties," *RSC advances,* vol. 1, no. 8, pp. 1482-1488, 2011.

[96]T.-T. Li, Y. Wang, H.-K. Peng, X. Zhang, B.-C. Shiu, J.-H. Lin, *et al*. "Lightweight, flexible and superhydrophobic composite nanofiber films inspired by nacre for highly electromagnetic interference shielding," *Composites Part A: Applied Science and Manufacturing,* vol. 128, p. 105685, 2020.

[97]D.-E. Lee, E.-Y. Choi, H.-J. Yang, A. S. Murthy, T. Singh, J.-M. Lim, *et al*. "Highly stretchable superhydrophobic surface by silica nanoparticle embedded electrospun fibrous mat," *Journal of colloid and interface science,* vol. 555, pp. 532-540, 2019.

[98]J. Sheng, Y. Xu, J. Yu, B. Ding. "Robust fluorine-free superhydrophobic amino-

silicone oil/SiO2 modification of electrospun polyacrylonitrile membranes for waterproof-breathable application," *ACS Applied Materials & Interfaces,* vol. 9, no. 17, pp. 15139-15147, 2017.

[99]F. Mikaeili, P. I. Gouma. "Super water-repellent cellulose acetate mats," *Scientific reports,* vol. 8, no. 1, p. 12472, 2018.

[100] H. Yoshida, K. Yanagisawa. "Creation of superhydrophobic poly (L-phenylalanine) nonwovens by electrospinning," *Polymers,* vol. 10, no. 11, p. 1212, 2018.

[101] G. Gong, J. Wu, J. Liu, N. Sun, Y. Zhao, L. Jiang. "Bio-inspired adhesive superhydrophobic polyimide mat with high thermal stability," *Journal of Materials Chemistry,* vol. 22, no. 17, pp. 8257-8262, 2012.

[102] H. Yoshida, D. Klee, M. Möller, M. Akashi. "Creation of superhydrophobic electrospun nonwovens fabricated from naturally occurring poly (amino acid) derivatives," *Advanced Functional Materials,* vol. 24, no. 40, pp. 6359-6364, 2014.

[103] T. Pisuchpen, N. Chaim-Ngoen, N. Intasanta, P. Supaphol, V. P. Hoven. "Tuning hydrophobicity and water adhesion by electrospinning and silanization," *Langmuir,* vol. 27, no. 7, pp. 3654-3661, 2011.

[104] N. Janardan, M. V. Panchagnula. "Effect of the initial conditions on the onset of motion in sessile drops on tilted plates," *Colloids and Surfaces A: Physicochemical and Engineering Aspects,* vol. 456, pp. 238-245, 2014.

[105] L. Yang, X. Luo, W. Chang, Y. Tian, Z. Wang, J. Gao, *et al*. "Manufacturing of anti-fogging super-hydrophilic microstructures on glass by nanosecond laser," *Journal of Manufacturing Processes,* vol. 59, pp. 557-565, 2020.

[106] T. Hao, X. Ma, Z. Lan, N. Li, Y. Zhao, H. Ma. "Effects of hydrophilic surface on heat transfer performance and oscillating motion for an oscillating heat pipe," *International Journal of Heat and Mass Transfer,* vol. 72, pp. 50-65, 2014.

[107] T. Shimizu, T. Goda, N. Minoura, M. Takai, K. Ishihara. "Super-hydrophilic silicone hydrogels with interpenetrating poly (2-methacryloyloxyethyl phosphorylcholine) networks," *Biomaterials,* vol. 31, no. 12, pp. 3274-3280, 2010.

[108] R. Blossey. "Self-cleaning surfaces—virtual realities," *Nature materials,* vol. 2, no. 5, pp. 301-306, 2003.

[109] Y. Chen, B. He, J. Lee, N. A. Patankar. "Anisotropy in the wetting of rough surfaces," *Journal of colloid and interface science,* vol. 281, no. 2, pp. 458-464, 2005.

[110] W. Ding, Z. Cao, B. Wang, S. Xu, Z. Wang. "Construction of grating structure model based on Gibbs free energy and experimental verification by micro-milling," *Applied Physics A,* vol. 125, no. 6, pp. 1-8, 2019.

[111] S. Zhenyu, L. Zhanqiang, S. Hao, Z. Xianzhi. "Prediction of contact angle for hydrophobic surface fabricated with micro-machining based on minimum Gibbs free energy," *Applied Surface Science,* vol. 364, pp. 597-603, 2016.

[112] C. T. Cheng, S. To, G. Zhang. "Characterization of intermediate wetting states on micro-grooves by water droplet contact line," *Journal of Industrial and Engineering Chemistry,* vol. 91, pp. 69-78, 2020.

[113] B. Wang, Y. Zhang, J. Song, Z. Wang. "Investigation and prediction on regulation of hydrophobicity of polymethyl methacrylate (PMMA) surface by femtosecond laser irradiation," *Coatings,* vol. 10, no. 4, p. 386, 2020.

[114] X.-L. Meng, L.-S. Wan, Z.-K. Xu. "Insights into the static and advancing water contact angles on surfaces anisotropised with aligned fibers: Experiments and modeling," *Colloids and Surfaces A: Physicochemical and Engineering Aspects,* vol. 389, no. 1-3, pp. 213-221, 2011.

[115] S. Koombhongse, W. Liu, D. H. Reneker. "Flat polymer ribbons and other shapes by electrospinning," *Journal of Polymer Science Part B: Polymer Physics,* vol. 39, no. 21, pp. 2598-2606, 2001.

[116] Y.-J. Sheng, S. Jiang, H.-K. Tsao. "Effects of geometrical characteristics of surface roughness on droplet wetting," *The Journal of chemical physics,* vol. 127, no. 23, p. 234704, 2007.

[117] G. Whyman, E. Bormashenko. "How to make the Cassie wetting state stable?," *Langmuir,* vol. 27, no. 13, pp. 8171-8176, 2011.

[118] L. Barbieri, E. Wagner, P. Hoffmann. "Water wetting transition parameters of perfluorinated substrates with periodically distributed flat-top microscale obstacles," *Langmuir,* vol. 23, no. 4, pp. 1723-1734, 2007.

[119] A. Bussonnière, M. B. Bigdeli, D.-Y. Chueh, Q. Liu, P. Chen, P. A. Tsai. "Universal wetting transition of an evaporating water droplet on hydrophobic micro-and nano-structures," *Soft matter,* vol. 13, no. 5, pp. 978-984, 2017.

[120] J. Ou, G. Fang, W. Li, A. Amirfazli. "Wetting transition on textured surfaces: a thermodynamic approach," *The Journal of Physical Chemistry C,* vol. 123, no. 39, pp. 23976-23986, 2019.

[121] W. Li, A. Amirfazli. "A thermodynamic approach for determining the contact angle hysteresis for superhydrophobic surfaces," *Journal of colloid and interface science,* vol. 292, no. 1, pp. 195-201, 2005.

[122] L. Tie, Z. Guo, W. Liu. "Anisotropic wetting properties on various shape of parallel grooved microstructure," *Journal of colloid and interface science,* vol. 453, pp. 142-150, 2015.

[123] L. He, W. Liang, Z. Wang, B. Yang, Z. Duan, Y. Chen. "3-D thermodynamic analysis on wetting behavior of superhydrophobic surfaces," *Colloids and Surfaces A: Physicochemical and Engineering Aspects,* vol. 504, pp. 201-209, 2016.

[124] D. Kim, N. M. Pugno, S. Ryu. "Wetting theory for small droplets on textured solid surfaces," *Scientific reports,* vol. 6, no. 1, pp. 1-8, 2016.

[125] J. Eick, R. Good, A. Neumann. "Thermodynamics of contact angles. II. Rough solid surfaces," *Journal of Colloid and Interface Science,* vol. 53, no. 2, pp. 235-248, 1975.

[126] R. Shuttleworth, G. Bailey. "The spreading of a liquid over a rough solid," *Discussions of the Faraday Society,* vol. 3, pp. 16-22, 1948.

[127] M. Reyssat, D. Quéré. "Contact angle hysteresis generated by strong dilute defects," *The Journal of Physical Chemistry B,* vol. 113, no. 12, pp. 3906-3909, 2009.

[128] R. Raj, R. Enright, Y. Zhu, S. Adera, E. N. Wang. "Unified model for contact angle hysteresis on heterogeneous and superhydrophobic surfaces," *Langmuir,* vol. 28, no. 45,

pp. 15777-15788, 2012.

[129] H.-J. Butt, C. Semprebon, P. Papadopoulos, D. Vollmer, M. Brinkmann, M. Ciccotti. "Design principles for superamphiphobic surfaces," *Soft Matter,* vol. 9, no. 2, pp. 418-428, 2013.

[130] J. Panter, Y. Gizaw, H. Kusumaatmaja. "Multifaceted design optimization for superomniphobic surfaces," *Science advances,* vol. 5, no. 6, p. eaav7328, 2019.

[131] Z. Zhang, M. Zhao, Y. Ahn, J. Jang. "Wettability of a surface engraved with the periodic nanoscale trenches: Effects of geometry and pressure," *Journal of Molecular Liquids,* vol. 335, p. 116276, 2021.

[132] Y. Kaufman, S.-Y. Chen, H. Mishra, A. M. Schrader, D. W. Lee, S. Das, *et al*. "Simple-to-apply wetting model to predict thermodynamically stable and metastable contact angles on textured/rough/patterned surfaces," *The Journal of Physical Chemistry C,* vol. 121, no. 10, pp. 5642-5656, 2017.

[133] A. Marmur. "From hygrophilic to superhygrophobic: theoretical conditions for making high-contact-angle surfaces from low-contact-angle materials," *Langmuir,* vol. 24, no. 14, pp. 7573-7579, 2008.

[134] E. Bormashenko. "Wetting of flat and rough curved surfaces," *The Journal of Physical Chemistry C,* vol. 113, no. 40, pp. 17275-17277, 2009.

[135] D. Arisawa, Y. Umetsu, A. Yoshizawa, C. Hill, J. Eastoe, F. Guittard, *et al*. "Controlling water adhesion on superhydrophobic surfaces with bi-functional polymers," *Colloids and Surfaces A: Physicochemical and Engineering Aspects,* vol. 616, p. 126307, 2021.

[136] C. Yuan, M. Huang, X. Yu, Y. Ma, X. Luo. "A simple approach to fabricate the rose petal-like hierarchical surfaces for droplet transportation," *Applied Surface Science,* vol. 385, pp. 562-568, 2016.

[137] J. W. Gose, K. Golovin, M. Boban, J. M. Mabry, A. Tuteja, M. Perlin, *et al*. "Characterization of superhydrophobic surfaces for drag reduction in turbulent flow," *Journal of Fluid Mechanics,* vol. 845, pp. 560-580, 2018.

[138] H. T. Bahrami, B. Ahmadi, H. Saffari. "Preparing superhydrophobic copper surfaces with rose petal or lotus leaf property using a simple etching approach," *Materials Research Express,* vol. 4, no. 5, p. 055014, 2017.

[139] A. Rawal. "Design parameters for a robust superhydrophobic electrospun nonwoven mat," *Langmuir,* vol. 28, no. 6, pp. 3285-3289, 2012.

[140] T. Bucher, M. Amrei, H. V. Tafreshi. "Wetting resistance of heterogeneous superhydrophobic coatings with orthogonally layered fibers," *Surface and Coatings Technology,* vol. 277, pp. 117-127, 2015.

[141] P. Katta, M. Alessandro, R. Ramsier, G. Chase. "Continuous electrospinning of aligned polymer nanofibers onto a wire drum collector," *Nano letters,* vol. 4, no. 11, pp. 2215-2218, 2004.

[142] D. Ebert, B. Bhushan. "Durable Lotus-effect surfaces with hierarchical structure using micro-and nanosized hydrophobic silica particles," *Journal of colloid and interface science,* vol. 368, no. 1, pp. 584-591, 2012.

[143] C.-H. Chen, I.-C. Cheng, J.-Z. Chen. "Facile method to convert petal effect surface to lotus effect surface for superhydrophobic polydimethylsiloxane," *Surfaces and Interfaces,* vol. 30, p. 101901, 2022.

[144] D. Wang, Q. Sun, M. J. Hokkanen, C. Zhang, F.-Y. Lin, Q. Liu, *et al*. "Design of robust superhydrophobic surfaces," *Nature,* vol. 582, no. 7810, pp. 55-59, 2020.

[145] B. Emami, H. V. Tafreshi, M. Gad-el-Hak, G. Tepper. "Effect of fiber orientation on shape and stability of air–water interface on submerged superhydrophobic electrospun thin coatings," *Journal of Applied Physics,* vol. 111, no. 6, p. 064325, 2012.

[146] T. Onda. "Theoretical Investigation of Wenzel and Cassie Wetting States on Porous Films and Fiber Meshes," *Langmuir,* vol. 38, no. 45, pp. 13744-13752, 2022.

[147] Y. Xue, S. Chu, P. Lv, H. Duan. "Importance of hierarchical structures in wetting stability on submersed superhydrophobic surfaces," *Langmuir,* vol. 28, no. 25, pp. 9440-9450, 2012.

[148] J. Berthier, K. A. Brakke, *The physics of microdroplets*. John Wiley & Sons, 2012.

[149] D. L. Hu, B. Chan, J. W. Bush. "The hydrodynamics of water strider locomotion," *nature,* vol. 424, no. 6949, pp. 663-666, 2003.

[150] S. Brandon, N. Haimovich, E. Yeger, A. Marmur. "Partial wetting of chemically patterned surfaces: the effect of drop size," *J Colloid Interface Sci,* vol. 263, no. 1, pp. 237-43, Jul 1 2003.

[151] L. He, W. Liang, Z. Wang, A. Akbarzadeh. "A three-dimensional model for analyzing the anisotropic wetting behavior of striped surfaces," *Colloids and Surfaces A: Physicochemical and Engineering Aspects,* vol. 552, pp. 67-74, 2018.

[152] H. Fashandi, M. Karimi. "Pore formation in polystyrene fiber by superimposing temperature and relative humidity of electrospinning atmosphere," *Polymer,* vol. 53, no. 25, pp. 5832-5849, 2012.

[153] P. Tsai, R. G. Lammertink, M. Wessling, D. Lohse. "Evaporation-triggered wetting transition for water droplets upon hydrophobic microstructures," *Phys Rev Lett,* vol. 104, no. 11, p. 116102, Mar 19 2010.

[154] F. Schellenberger, N. Encinas, D. Vollmer, H.-J. Butt. "How water advances on superhydrophobic surfaces," *Physical review letters,* vol. 116, no. 9, p. 096101, 2016.

[155] A. Marmur. "The Lotus effect: superhydrophobicity and metastability," *Langmuir,* vol. 20, no. 9, pp. 3517-9, Apr 27 2004.

[156] A. Dupuis, J. M. Yeomans. "Modeling droplets on superhydrophobic surfaces: equilibrium states and transitions," *Langmuir,* vol. 21, no. 6, pp. 2624-9, Mar 15 2005.

[157] Y. Jiang, J. Lian, Z. Jiang, Y. Li, C. Wen. "Thermodynamic analysis on wetting states and wetting state transitions of rough surfaces," *Adv Colloid Interface Sci,* vol. 278, p. 102136, Apr 2020.

[158] C. E. Cansoy. "The effect of drop size on contact angle measurements of superhydrophobic surfaces," *Rsc Advances,* vol. 4, no. 3, pp. 1197-1203, 2014.

[159] X. Yu, Y. Li, X. Wang, Y. Si, J. Yu, B. Ding. "Thermoconductive, moisture-permeable, and superhydrophobic nanofibrous membranes with interpenetrated boron nitride network for personal cooling fabrics," *ACS applied materials & interfaces,* vol. 12,

no. 28, pp. 32078-32089, 2020.

[160] X. Yu, Y. Li, X. Yin, X. Wang, Y. Han, Y. Si, *et al*. "Corncoblike, superhydrophobic, and phase-changeable nanofibers for intelligent thermoregulating and water-repellent fabrics," *ACS applied materials & interfaces,* vol. 11, no. 42, pp. 39324-39333, 2019.

[161] Y. Yuan, T. R. Lee. "Contact angle and wetting properties," *Surface science techniques,* pp. 3-34, 2013.

[162] C. Lv, C. Yang, P. Hao, F. He, Q. Zheng. "Sliding of water droplets on microstructured hydrophobic surfaces," *Langmuir,* vol. 26, no. 11, pp. 8704-8708, 2010.

[163] Z. Yan, J. Xiong, B. Wang, M. Gao, G. Yin, T. Hu, *et al*. "Recent advances in breathable electronics," *Nano Research,* pp. 1-13, 2022.

[164] J. Luo, S. Gao, H. Luo, L. Wang, X. Huang, Z. Guo, *et al*. "Superhydrophobic and breathable smart MXene-based textile for multifunctional wearable sensing electronics," *Chemical Engineering Journal,* vol. 406, p. 126898, 2021.

[165] L. Lao, D. Shou, Y. Wu, J. Fan. "“Skin-like” fabric for personal moisture management," *Science advances,* vol. 6, no. 14, p. eaaz0013, 2020.

[166] X. Zhang, X. Hao, Z. Zhai, J. Wang, H. Li, Y. Sun, *et al*. "Flexible H2S sensors: Fabricated by growing NO2-UiO-66 on electrospun nanofibers for detecting ultralow concentration H2S," *Applied Surface Science,* vol. 573, p. 151446, 2022.

[167] F. J. Maksoud, M. Lameh, S. Fayyad, N. Ismail, A. R. Tehrani-Bagha, N. Ghaddar, *et al*. "Electrospun waterproof breathable membrane with a high level of aerosol filtration," *Journal of Applied Polymer Science,* vol. 135, no. 2, p. 45660, 2018.

[168] S. Ghalei, J. Nourmohammadi, A. Solouk, H. Mirzadeh. "Enhanced cellular response elicited by addition of amniotic fluid to alginate hydrogel-electrospun silk fibroin fibers for potential wound dressing application," *Colloids Surf B Biointerfaces,* vol. 172, pp. 82-89, Dec 1 2018.

[169] X. Li, J. Lin, F. Bian, Y. Zeng. "Improving waterproof/breathable performance of electrospun poly(vinylidene fluoride) fibrous membranes by thermo-pressing," *Journal of*

*Polymer Science Part B: Polymer Physics*, vol. 56, no. 1, pp. 36-45, 2018.

[170] M. Zhang, J. Sheng, X. Yin, J. Yu, B. Ding. "Polyvinyl Butyral Modified Polyvinylidene Fluoride Breathable-Waterproof Nanofibrous Membranes with Enhanced Mechanical Performance," *Macromolecular Materials and Engineering*, vol. 302, no. 8, 2017.

[171] L. Yi, S. Wang, L. Wang, J. Yao, J. Marek, M. Zhang. "A waterproof and breathable nanofibrous membrane with thermal-regulated property for multifunctional textile application," *Journal of Applied Polymer Science*, vol. 138, no. 19, p. 50391, 2020.

[172] J. Sheng, Y. Li, X. Wang, Y. Si, J. Yu, B. Ding. "Thermal inter-fiber adhesion of the polyacrylonitrile/fluorinated polyurethane nanofibrous membranes with enhanced waterproof-breathable performance," *Separation and Purification Technology*, vol. 158, pp. 53-61, 2016.

[173] N. Wang, M. Cai, X. Yang, Y. Yang. "Electret nanofibrous membrane with enhanced filtration performance and wearing comfortability for face mask," *J Colloid Interface Sci*, vol. 530, pp. 695-703, Nov 15 2018.

[174] Y. Zhu, R. Haghniaz, M. C. Hartel, S. Guan, J. Bahari, Z. Li, *et al*. "A Breathable, Passive-Cooling, Non-Inflammatory, and Biodegradable Aerogel Electronics for Wearable Physical-Electrophysiological-Chemical Analysis," *Advanced Materials*, p. 2209300, 2022.

[175] X. Gong, X. Yin, F. Wang, X. Liu, J. Yu, S. Zhang, *et al*. "Electrospun Nanofibrous Membranes: A Versatile Medium for Waterproof and Breathable Application," *Small*, vol. 19, no. 2, p. 2205067, 2023.

[176] H. Yuan, Q. Zhou, Y. Zhang. "Improving fiber alignment during electrospinning," *Electrospun nanofibers*, pp. 125-147, 2017.

[177] M. M. Nazemi, A. Khodabandeh, A. Hadjizadeh. "Near-field electrospinning: crucial parameters, challenges, and applications," *ACS Applied Bio Materials*, vol. 5, no. 2, pp. 394-412, 2022.

[178] H. Aziz, M. Amrei, A. Dotivala, C. Tang, H. V. Tafreshi. "Modeling Cassie

droplets on superhydrophobic coatings with orthogonal fibrous structures," *Colloids and Surfaces A: Physicochemical and Engineering Aspects,* vol. 512, pp. 61-70, 2017.

[179] Y. Han, Y. Xu, S. Zhang, T. Li, S. Ramakrishna, Y. Liu. "Progress of improving mechanical strength of electrospun nanofibrous membranes," *Macromolecular Materials and Engineering,* vol. 305, no. 11, p. 2000230, 2020.

[180] G.-d. Kang, Y.-m. Cao. "Application and modification of poly (vinylidene fluoride)(PVDF) membranes–a review," *Journal of membrane science,* vol. 463, pp. 145-165, 2014.

[181] C. Yang, Q. Zeng, J. Huang, Z. Guo. "Droplet manipulation on superhydrophobic surfaces based on external stimulation: A review," *Advances in Colloid and Interface Science,* p. 102724, 2022.

[182] L. Ghasemi-Mobarakeh, M. P. Prabhakaran, M. Morshed, M.-H. Nasr-Esfahani, S. Ramakrishna. "Electrospun poly (ε-caprolactone)/gelatin nanofibrous scaffolds for nerve tissue engineering," *Biomaterials,* vol. 29, no. 34, pp. 4532-4539, 2008.

# Appendix A

# Fabrication of porous cellulose acetate fibers

This appendix is to help future works in wound dressing and tissue engineering as explained in Section 7.2.

## A.1 Introduction

Cellulose acetate, a widely used cellulose derivative, is an electrospinnable polymer featured with biocompatibility [1] and hydrophilicity [2]. Porous cellulose acetate fibers can help to apply the developed biaxial structure in medical dressing and develop petal-effect surfaces with higher adhesion strength. For medical dressing, the biaxial structure may be deposited onto a layer of porous cellulose acetate fibers for the following advantages. First, cellulose acetate is biocompatible to be attached to wound. Second, drugs can be loaded into the pores of fibers for better therapeutic effect. Third, the cellulose acetate fibrous structure can also be breathable. For petal-effect surfaces, the cellulose acetate fibers with surface pores may realize a high contact angle for the reduced liquid-air contact area, and the hydrophilicity of cellulose acetate provides a higher adhesion to liquid. In addition, porous cellulose acetate fibers may also be applied in cancer diagnosis considering that the rough surface of single fiber facilitates cancer cell adhesion [3].

In this appendix, porous cellulose acetate fibers are fabricated using two electrospinning-based methods: thermal-induced phase separation and breath figure, and selective removal of sacrificial component.

## A.2 Experimental methods

### A.2.1 Materials

Cellulose acetate (acetyl content 39.8%, Mw =30 kDa), *N*, *N*-dimethylacetamide (DMAc), acetone, and dichloromethane (DCM) were purchased from Sigma Aldrich, US. PVP (Mw

=1300 kDa) was purchased from Thermo Fisher Scientific, US. All chemicals were used as received without any further purification.

### A.2.2 Fabrication of cellulose acetate fibers

The electrospinning-based method with thermal-induced phase separation and breath figure is carried out as follow. First, 1.1 g cellulose acetate is dissolved in a mixture of 6.5 mL DCM and 3.5 mL acetone (unless specified otherwise) and by magnetic stirring for 3 hours for a 11% (w/v) precursor solution. After that, the precursor solution is transferred into a 20 mL syringe with metallic needle (gauge 22) for electrospinning with spinning distance of 9 cm, solution feeding rate of 8 mL/h, and applied voltage of 7.5 kV. The temperature is kept at 23℃ while the relative humidity is adjusted among 50%, 65%, and 80%. Fibers are collected by non-stick aluminum foils on a fixed and grounded collector. After electrospinning, the fibers are dried in a vacuum oven at 80 ℃ overnight to remove residual solvents.

For the selective removal of sacrificial component, the precursor solution is prepared by dissolving 15% (w/v) cellulose acetate and PVP in a binary solvent system: 0.9 g cellulose acetate and 0.45 g PVP in 3 mL DMAc and 6 mL acetone. After that, the precursor solution is transferred to a 20 mL syringe with stainless steel needle (gauge 22) for electrospinning with spinning distance of 8 cm, solution feeding rate of 0.7 mL/h, and applied voltage of 6 kV. The temperature and the relative humidity are maintained at 23℃ and 40%, respectively. Fibers are collected by a stainless steel mesh, which is placed on the grounded collector. A fiber mat is obtained by detaching it from the mesh after 30 min electrospinning. The fiber mat is dried in a vacuum oven at 80 ℃ overnight to remove residual solvents. Then the mat is sandwiched by two stainless steel meshes and immersed in distilled water contained by a beaker. The beaker is placed on a magnetic stirrer so the PVP in fibers can be efficiently dissolved. After 12 hours immersing, the fiber mat is dried in the vacuum oven at 80 ℃ overnight to remove residual water on fibers.

### A.2.3 Characterization of cellulose acetate fibers

The electrospun fibers are first screened under an optical microscope (Swift SW380B, US) with magnifications of 40-1,000X to verify the formation of continuous fibers rather than beads. Then the fabricated fibers are coated with gold and observed under a field-emission SEM (Zeiss Leo 1530, Germany) at 5.0 kV for fiber morphology, especially the presence of pores on fiber surfaces. The captured SEM images at 500X and 25kX magnifications are analyzed using software ImageJ to characterize fiber diameter and pore size, respectively.

## A.3 Results and discussion

Figure A.1 shows the SEM images at 500X and 25kX magnifications of fabricated cellulose acetate fibers with phase separation and breath figure at RH of (A-B) 50%, (C-D) 65%, (E-F) 80%, and (G-H) 65% but with a DCM-to-acetone volume ratio of 4:1. It can be seen that continuous fibers without beads are generated from Figure A.1 (A, C, E, G) and pores are created on fiber surfaces from Figure A.1 (B, D, F, H)

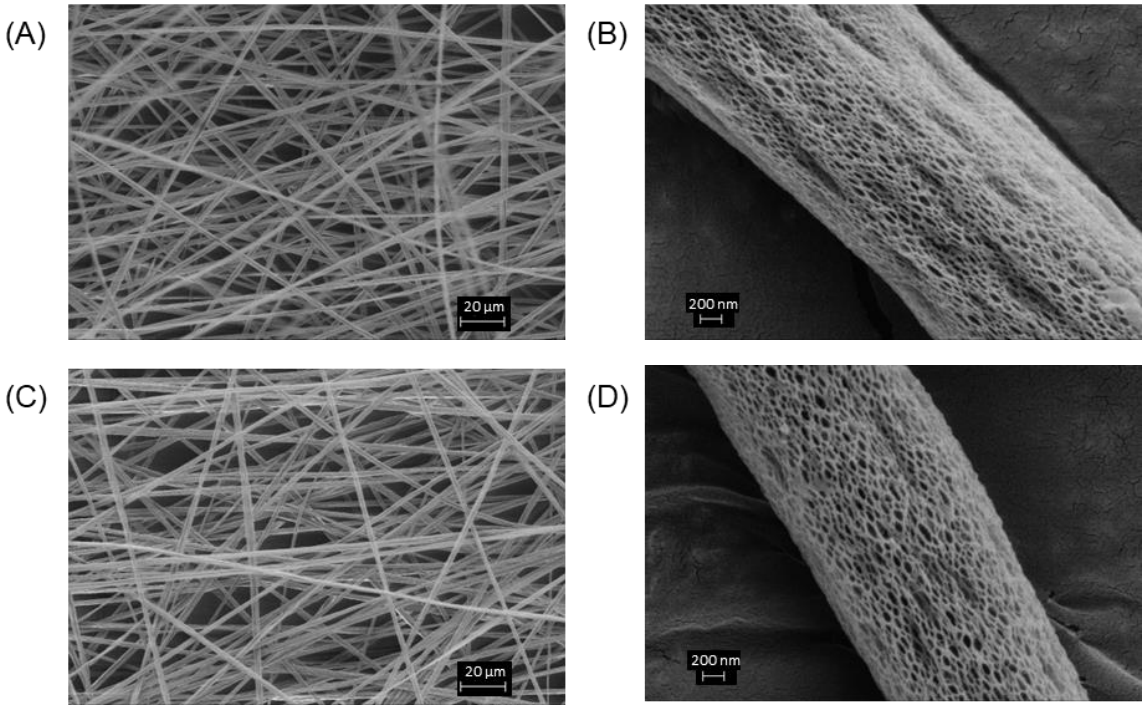

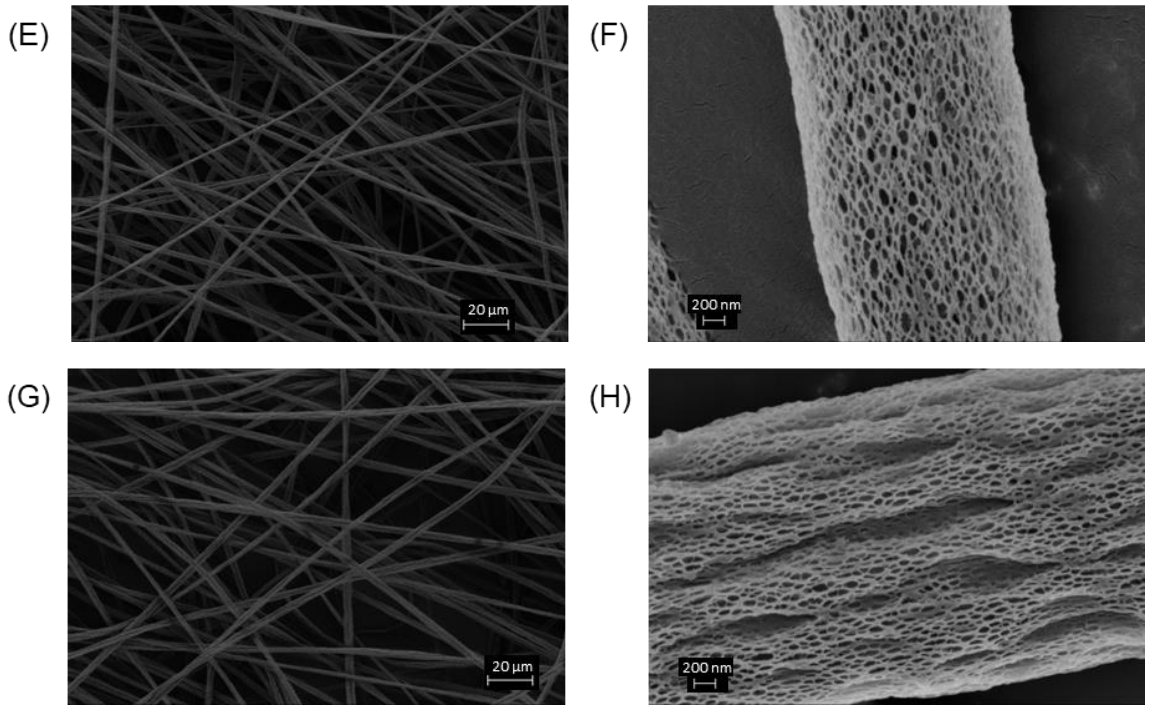


**Figure A.1.** SEM images of the electrospun cellulose acetate fibers with phase separation and breath figure at RH of (A-B) 50%, (C-D) 65%, (E-F) 80%, and (G-H) 65% but with a DCM-to-acetone volume ratio of 4:1.

By image processing, the fiber diameter distributions are $2.38 \pm 0.69$ μm, $2.34 \pm 0.65$ μm, and $2.31 \pm 0.55$ μm for RH of 50%, 65%, and 80%, respectively, indicating a small influence of RH on the fiber diameter. For the RH of 65% and DCM-to-acetone volume ratio of 4:1, the fiber diameter distribution is $2.67 \pm 0.60$ μm. The increase of average fiber diameter is attributed to the increased solution viscosity by increasing the proportion of DCM [4]. The pore size distributions are characterized to be $38 \pm 18$ nm, $43 \pm 17$ nm, $59 \pm 23$ nm, and $52 \pm 17$ nm for RH of 50%, 65%, 80%, and 65% with DCM-to-acetone ratio of 4:1,respectively. The increase of pore size with RH and DCM ratio can be explained the formation mechanism of surface pores as follows.

In electrospinning, the rapid evaporation of DCM due to its low boiling point of 39.6 ℃ causes a temperature reduction of the jet out of Taylor cone, resulting in that the jet becomes thermodynamically unstable and separates into polymer-rich and polymer-poor phases. As solvent evaporates, the polymer-rich phase forms the fiber matrix while the polymer-poor

phase forms the pores. Thus, increasing DCM enhances the phase separation and results in larger pores. Meanwhile, the temperature reduction also causes condensation of water vapor into liquid droplets onto the jets in electrospinning. The condensed droplets also contribute to the formation of the pores, because they occupy spaces before the jets are fully solidified. Larger droplets are condensed with increasing RH, resulting in larger pores of fibers.

Figure A.2 shows the SEM images of the fabricated cellulose acetate fibers after selective removal of PVP. By image processing, the fiber diameter distribution in Figure A.2(A) is $486 \pm 98$ nm. From Figure A.2(B), it can be seen that the fiber surfaces are roughened and featured with shallow grooves, resulting from the removal of PVP after electrospinning. The removal of PVP in water is based on the low water solubility of cellulose acetate. However, deep and round pores as those shown in Figure A.1 are not formed, because deeper PVP is hard to be fully dissolved.

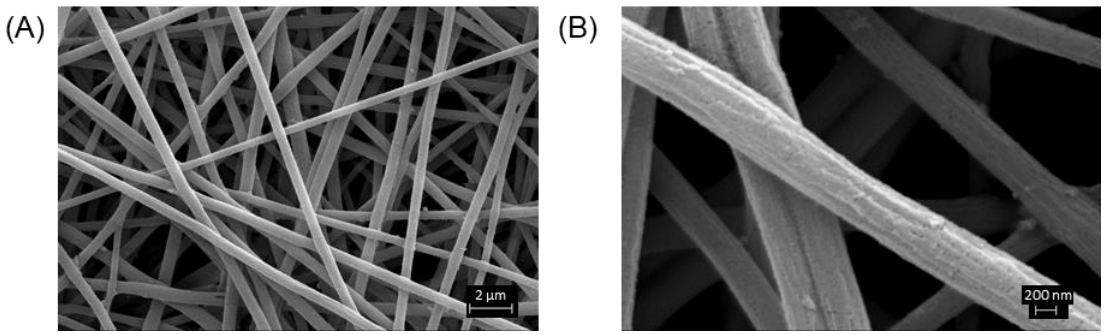


**Figure A.2.** SEM images at (A) 5kX and (B) 25kX magnifications of the fabricated cellulose acetate fibers by selective removal after electrospinning.

## A.4 Summary

Porous cellulose acetate fibers are fabricated based on electrospinning with thermal-induced phase separation and breath figure, and selective removal of sacrificial PVP. Combination of phase separation and breath figure results in fibers with deep and round pores, and fibers with adjustable pore sizes are obtained by controlling the relative humidity in electrospinning. Differently, selective removal generates fibers with shallow grooves on surfaces.

## References

[1] M. A. Wsoo, S. Shahir, S. P. M. Bohari, N. H. M. Nayan, S. I. Abd Razak. "A review on the properties of electrospun cellulose acetate and its application in drug delivery systems: A new perspective," *Carbohydrate research,* vol. 491, p. 107978, 2020.

[2] F. Mikaeili, P. I. Gouma. "Super water-repellent cellulose acetate mats," *Scientific reports,* vol. 8, no. 1, p. 12472, 2018.

[3] Y. Zhang, Y. Li, Z. Tan. "A review of enrichment methods for circulating tumor cells: from single modality to hybrid modality," *Analyst,* vol. 146, no. 23, pp. 7048-7069, 2021.

[4] A. Celebioglu, T. Uyar. "Electrospun porous cellulose acetate fibers from volatile solvent mixture," *Materials Letters,* vol. 65, no. 14, pp. 2291-2294, 2011.

# Appendix B

# Image processing for fiber morphology

## B.1 Fiber diameter distribution

The diameter of the electrospun fibers in this thesis is measured using SEM images based on the scale bar. Figure B.1 shows the measurement of fiber diameter distribution for the cellulose acetate fibers in Appendix. A. The measurement is performed in ImageJ software. For each SEM image, two horizontal and three vertical lines, uniformly distributed, are drawn across the image, and fiber diameter is measured based on the scale bar at each intersection of fiber and the drawn line to avoid bias. As a result, more than 50 fibers are measured for each image to generate the fiber diameter distribution, and descriptive statistics with mean and standard deviation is presented.

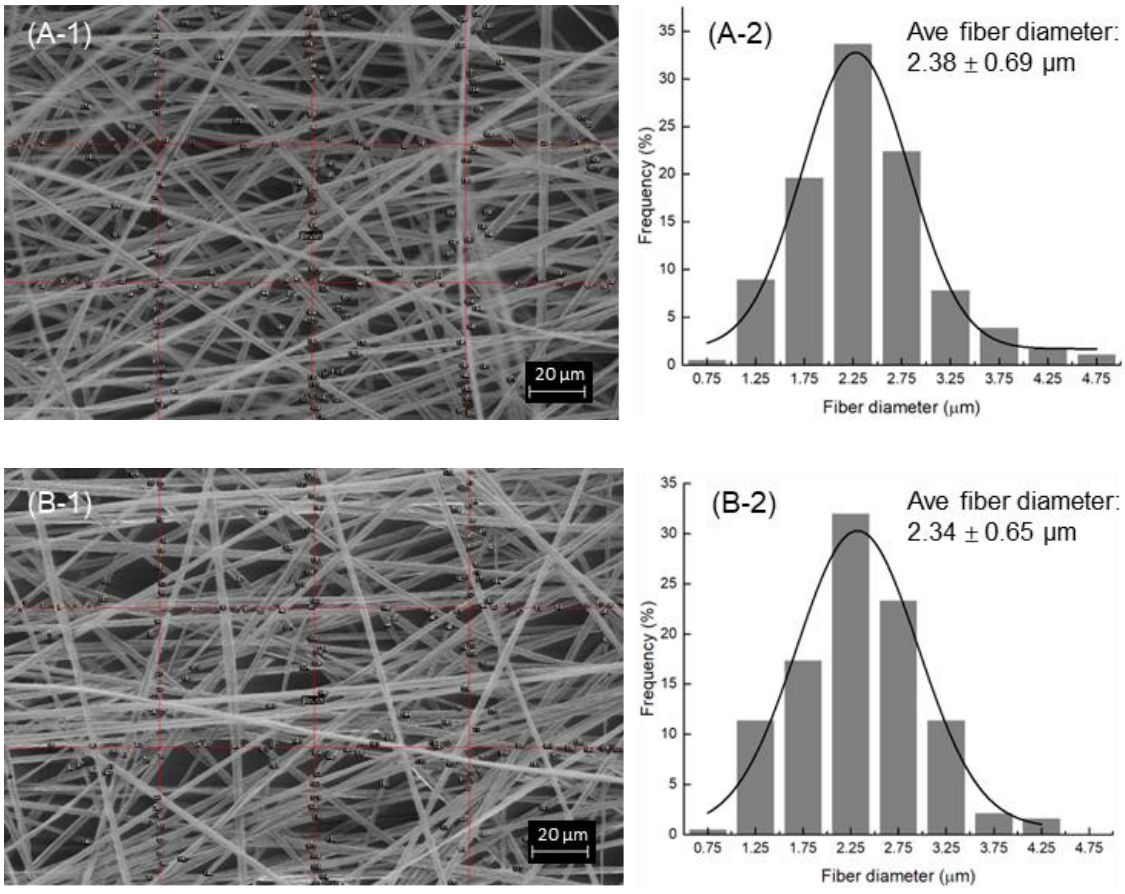

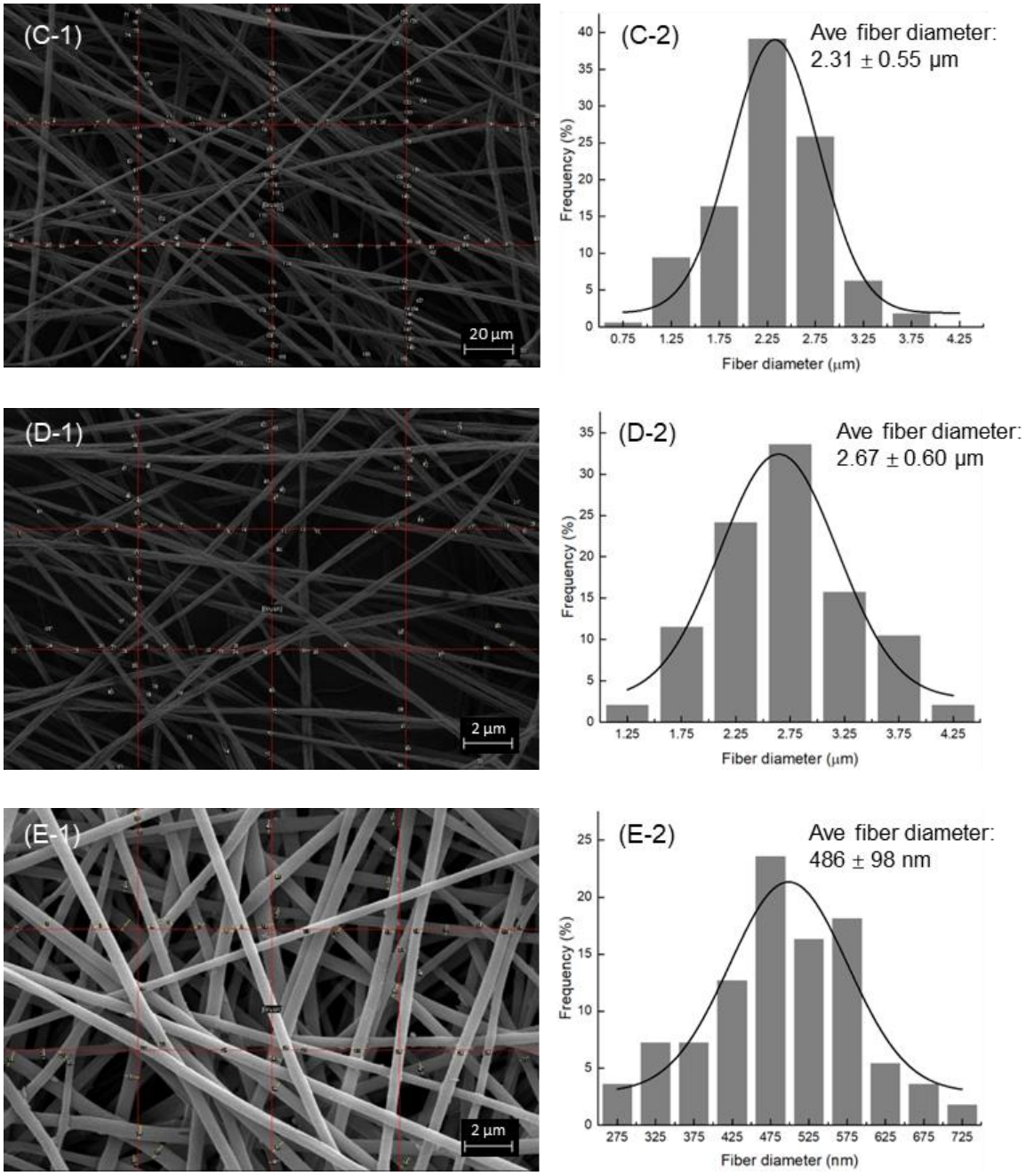


**Figure B.1.** Measurement of fiber diameter distribution from the SEM images based on the scale bar: (A-E) for Figure A.1(A), (C), (E), (G), and Figure A.2 (A), respectively.

Figure B.2 presents the fiber diameter distributions of the fabricated porous PS fibers in Figure 5.2. The fiber diameter is measured using similar method as that for Figure B.1. For each SEM image, one horizontal are drawn across the image because the fibers are aligned. More than 30 fibers are measured for fiber diameter distribution for each fabrication RH, and descriptive statistics with mean and standard deviation is presented.

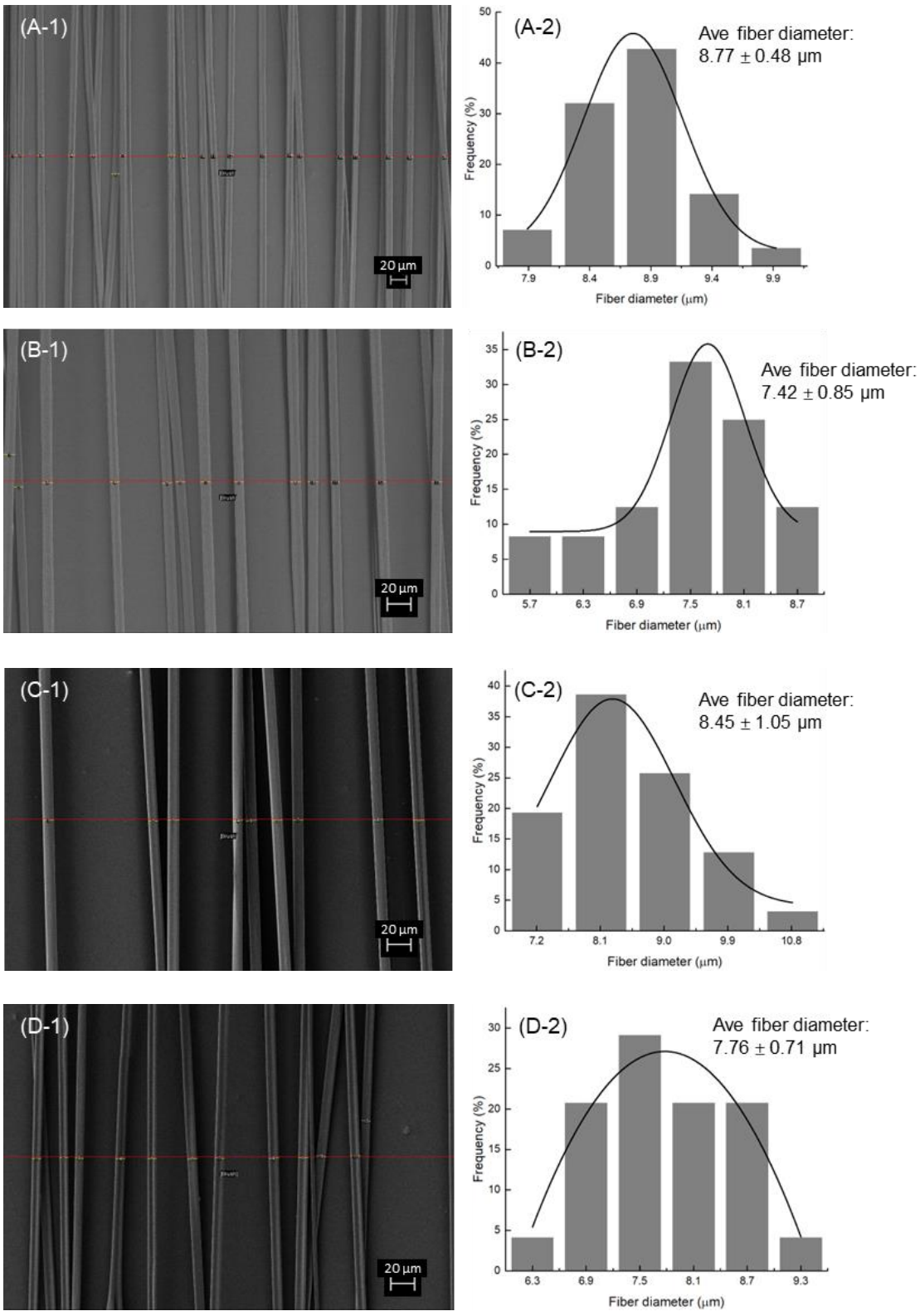


**Figure B.2.** Measurement of fiber diameter distribution of the porous PS fibers fabricated under RH of (A) 80%, (B) 60%, (C) 50%, and (D) 40% in Figure 5.2.

## B.2 Pore size distribution

Figure B.3 shows the measurement of pore size distribution of the porous PS fibers in Chapter 5. First, a 400 × 400 pixels area is selected in the middle area of fiber for image processing. In this area, the colors of fiber matrix and pore are adjusted to white and black, respectively, to increase the contrast. Then, the area of each pore is quantified by the number of pixels in black using the "Analyze Particles" function in ImageJ. Meanwhile, the pore area fraction is also obtained by ratios of total pore area to the selected fiber area. Finally, the equivalent pore diameter is calculated based on the pore area, and descriptive statistics with mean and standard deviation is presented.

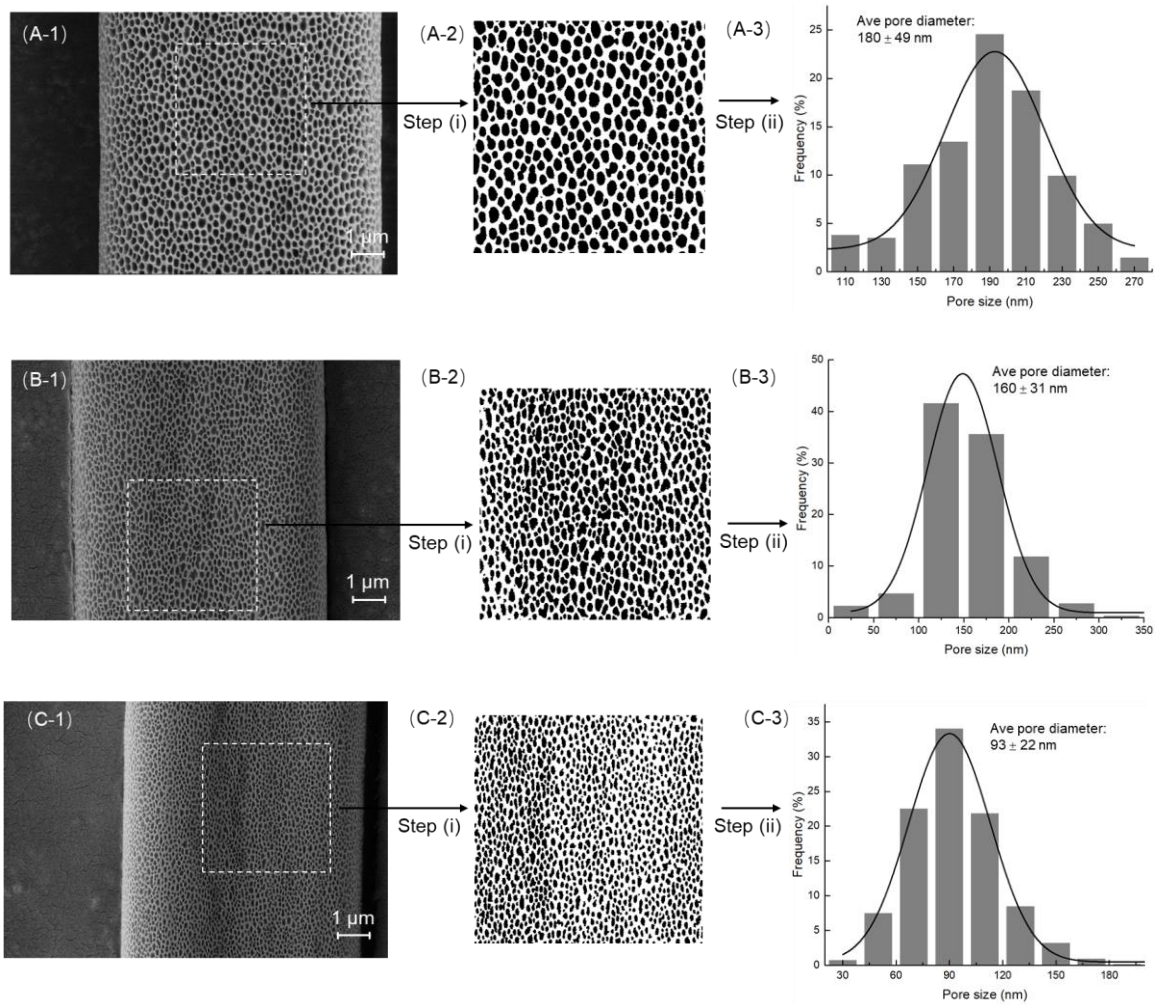

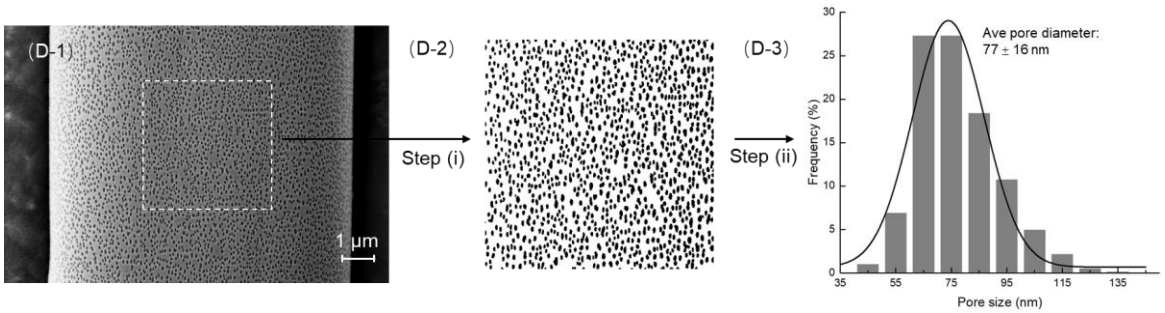


**Figure B.3.** Measurement of pore size distribution of porous PS fibers from the SEM images: (A-D) for Figure 5.2 (A-D), respectively. Step (i) adjusts the color of fiber matrix and pore into white and black, respectively. Step (ii) calculates the equivalent diameter of each pore based on the pore area (number of pixels).

Figure B.4 presents the measurement of the pore size distribution of the porous cellulose acetate fibers fabricated in Appendix. A based on the similar method for Figure B.3. Two 200 × 200 pixels areas or one 100 × 400 pixels area are selected for processing because of the smaller diameter of cellulose acetate fibers.

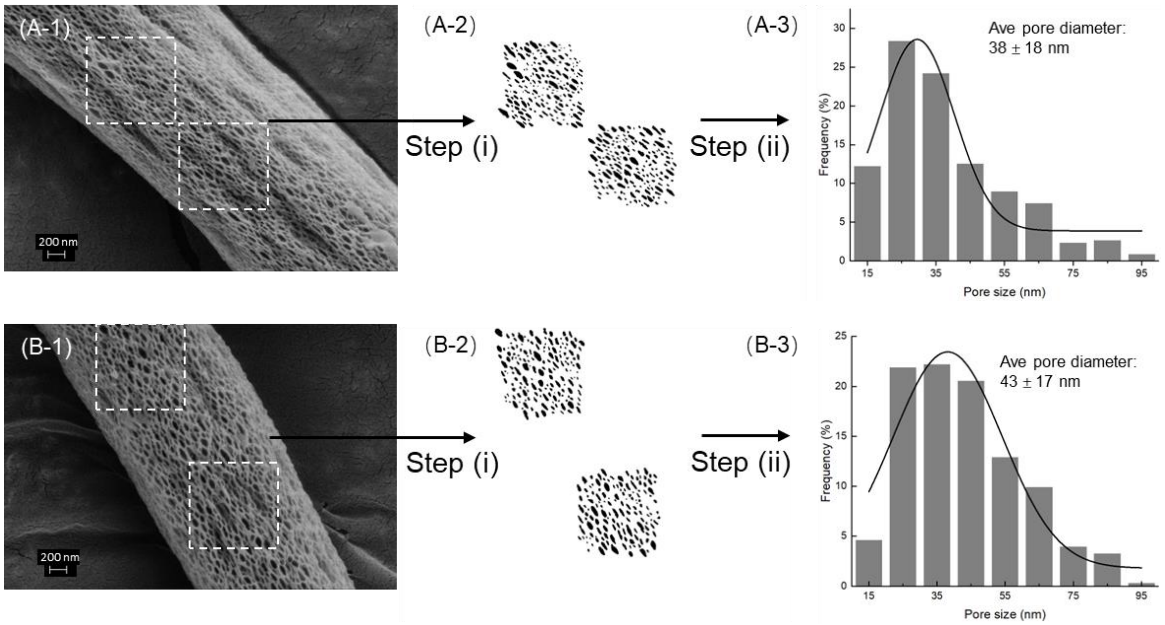

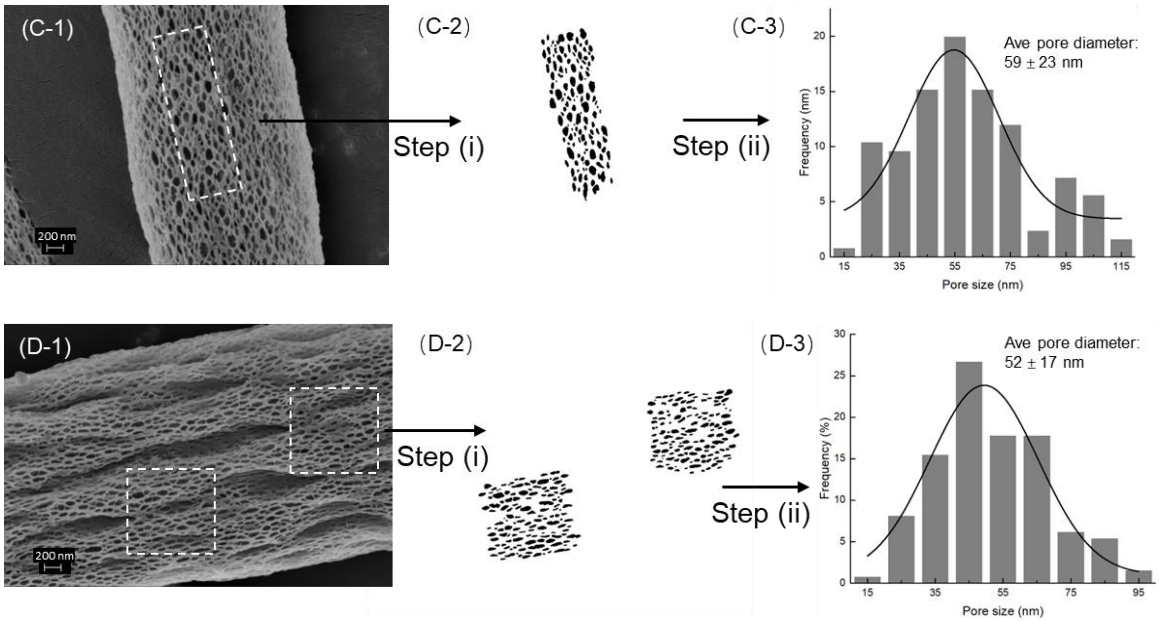


**Figure B.4.** Measurement of pore size distribution of porous cellulose acetate fibers from the SEM images: (A-D) for Figure A.1 (B), (D), (F), and (H), respectively.